Ultrafast Vibrational Spectroscopy of Carbon Dioxide in Polymers and Ionic Liquid-Polymer Composite Materials

by

C. J. Kelsheimer

B.S. Biochemistry, Florida State University, 2016

B.S. Psychology, Florida State University, 2016

Submitted to the Graduate Faculty of

the Kenneth P. Dietrich School of Arts and Sciences in partial fulfillment

of the requirements for the degree of

Doctor of Philosophy

University of Pittsburgh

2021

UNIVERSITY OF PITTSBURGH

KENNETH P. DIETRICH SCHOOL OF ARTS AND SCIENCES

This dissertation was presented

by

C. J. Kelsheimer

It was defended on

March 29, 2021

and approved by

Sean Garrett-Roe, Professor, Department of Chemistry

Sunil Saxena, Professor, Department of Chemistry

Jennifer Laaser, Assistant Professor, Department of Chemistry

Susan Fullerton, Associate Professor, Department of Chemical and Petroleum Engineering,

University of Pittsburgh

Copyright © by C. J. Kelsheimer
2021

Ultrafast Vibrational Spectroscopy of Carbon Dioxide in Polymers and Ionic Liquid-Polymer Composite Materials

C. J. Kelsheimer, PhD

University of Pittsburgh, 2021

Ultrafast two-dimensional infrared spectroscopy enables measurement of frequency dynamics and inter- and intramolecular kinetics which report motions on femto- to picosecond timescales and Ångstrom length scales. These measurements probe carbon dioxide's interaction with ionic liquids, polymers and ionic liquid-polymer composite materials. These systems are of interest for carbon capture and storage utility, an important step of curbing greenhouse gas emissions.

In an investigation of carbon dioxide in a poly(ethylene glycol) diacrylate gel, an unexpected hot ground state appears, and the model used to describe the intramolecular landscape of carbon dioxide is expanded as a result. Polarization-controlled ultrafast experiments are used to measure anisotropy and investigate the two-dimensional frequency dependence in a representative composite material.

Spectra are taken of carbon dioxide in a pair of structurally isomeric, high molecular weight polymers. Poly(vinyl acetate) and Poly(methyl acrylate) show different cloud point behavior despite being nearly identical. While their frequency fluctuation dynamics were not meaningfully different, their intramolecular kinetics were distinctly different, lending weight to direct interaction with the polymer side chains as the cause of different cloud point behavior.

Finally, carbon dioxide in a volume percent series of ion gels is measured. These show a nonlinear, non-monotonic relationship between the timescales of structural reorganization and the percent by volume ionic liquid. A three-regime, core-shell-matrix type model is proposed and suggested as an explanation for this behavior, which reproduces the pattern of the data.

This work offers a perspective on the question of carbon dioxide's interaction with carbon capture media, and identifies important intra- and intermolecular processes that may govern this relationship. This work lays groundwork for further studies of ultrafast two-dimensional vibrational spectroscopy in composites, gels, polymers, and other solid materials, along with expanding the analytical tools to understand these interactions.

Table of Contents

List of Tables

List of Figures

Preface

There have been many pivotal moments in my educational career, but none as impactful as a single conversation in Fall of 2014, in the office of my undergraduate Organic Chemistry I honors professor, Dr. Jack Saltiel. The exact words of our conversation have long since been forgotten, but the effect never will be: within days of this conversation, my major had been changed from Chemical Science to Biochemistry, and I'd signed up for Calculus II. I was going to graduate school for Chemistry. The path of my life took a sharp turn that day, and I would not be where I am today otherwise.

The decision to come to the University of Pittsburgh brought a new round of decisions and pivotal moments, but one underlying fact has always been true: I am a better scientist for the path I've taken. Joining Dr. Sean Garrett-Roe's lab pushed me in ways I had never imagined. Physical Chemistry had never been a particular strong suit of mine, I'd never seen a laser table in my life, and quantum mechanics had always terrified me, and yet, under his guidance and support, I was able to thrive. It has not always been an easy road, but I am sure that I would not have gotten here without Sean's passion, understanding, kindness and his unwavering belief in me.

One of the first things I noticed upon joining the Garrett-Roe lab was the friendly, collaborative environment. Dr. Thomas Brinzer, Dr. Zhe Ren, and Dr. Clinton Johnson were all pivotal in paving the way for me, and were always willing to help when they could, even beyond their own graduation. Sunayana Mitra and Kai Gronborg have been with me every step of the way, sometimes quite literally, and I cannot thank the two of you enough for all the support and guidance you've offered me. Tyler Parrack, Sydney Giles, and Haoyuan Sun, I hope that I've made a positive impact on you all, as those who came before did on me. Thank you. Last, but certainly not least, I need to thank both of the undergraduate researchers I had the pleasure of working with: Sarah Leptinsky, who worked with me for a semester, and Daniella Levin, who worked with me for two years. Being a mentor was one of my most challenging and rewarding experiences, so thank you for allowing me that opportunity.

Graduate School, this PhD, life in Pittsburgh have all been an adventure, but it has not been a solo trip. The many friends I made, both before and during this program, were an invaluable source of joy, support and companionship. My family have always been my biggest cheerleaders, and their belief in me has been a powerful motivator. My parents have never been quiet about their pride in me, and my desire to live up to that has kept me going. Mom, Dad, thank you.

Though he only became my husband in 2019, Joseph has been by my side from the beginning. From moving into and out of third floor apartments, to a mid-PhD wedding, to preparing for an out-of-state move in the middle of a pandemic, I could not be more grateful. There were many days when I wanted to give up – and I came close. In those moments, I'd remind myself that I had to keep pushing: for Joe, our dog Akatsuki, and the future I want to build with them. There have been highs and lows, but I have always known that when I got home, they would be waiting for me, and that gave me the strength to get through it all.

I had no idea, in the final hours of the university being open in March of 2020, that I was performing the last laser experiments of my graduate career. The COVID-19 pandemic has impacted all of us, and it continues to every day. It is only because of the support of my advisor, coworkers, friends, family, and husband that I was able to complete my scientific inquiries and write this document.

1.0 Introduction

1.1 Angstroms and Picoseconds: 2D-IR Spectroscopy

Ultrafast two-dimensional infrared (2D-IR) spectroscopy records time-lapse-style information about a chromophore in its local environment. Infrared spectroscopy functions by causing molecular bonds to vibrate, which occurs on fast time scales and small length scales. These motions, as a result, are sensitive to even very small changes in the matrix around the chromophore of interest, such as carbon dioxide (CO_2), which makes 2D-IR spectroscopy a powerful investigative technique.

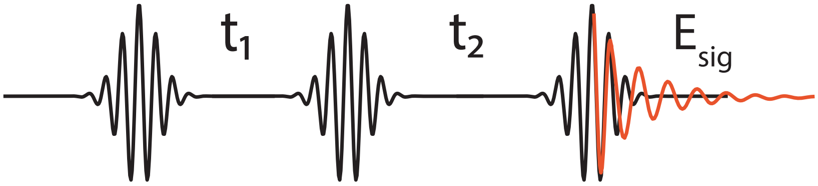

Figure 1.1: 2D-IR spectra result from the interaction of three ultrashort ($\sim$ 200 fs) pulses with a chromophore, and the resulting molecular response. The pulses are separated by time delays, t_1, and t_2. t_1 separates the "pumps", and t_2 is the "waiting time".

2D-IR measurements are achieved using a series of three infrared pulses to interrogate the chromophore (figure 1.1). A time-domain signal is collected over a range of t_1 times separating the first two pulses and is Fourier transformed into the initial frequency axis (ω_1). The delay between the second and third pulses, t_2, is varied over the course of an experiment. The system evolves unperturbed during this t_2 waiting time. The third pulse excites the system, resulting in a coherence state. The oscillating coherence state emits a signal that is directly detected in the frequency-domain and plotted as the final frequency axis (ω_3).

Interpretation of 2D-IR spectroscopy derives from the correlation between the two measurements (dimensions) of the system. This information is reported most typically as a series of waiting-time-labeled contour plots. In simple cases, the result is one blue peak along a diagonal ($\omega_1 = \omega_3$) and a red peak shifted anharmonically along the ω_3 axis (figure 1.2). The blue peak is a negative intensity peak containing the signals for stimulated emission and ground state bleach transitions. The red peak is a positive intensity peak containing the signal for the excited state absorption transition.

These plots contain the information needed to determine timescales of frequency dynamics, intra- and intermolecular kinetic rates, and much more, which can be extracted through a variety of methods, many of which involve understanding both the underlying quantum and statistical mechanics. The spectra are dependent on the local environment around the chromophore which reflects the molecular-scale details about a chromophore.

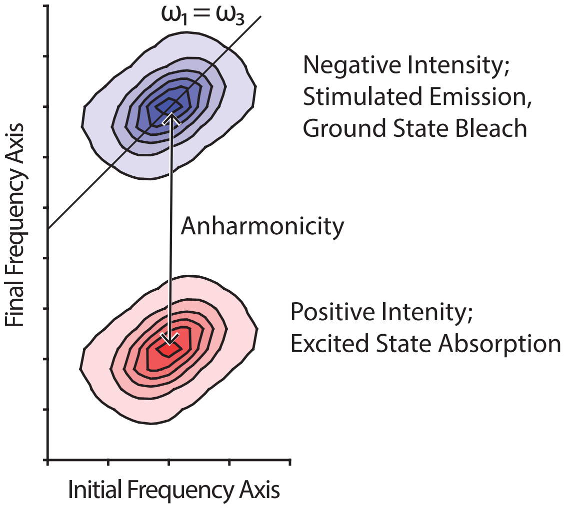

Figure 1.2: 2D-IR spectra usually contain at least two peaks: one blue, negative intensity peak, and one red, positive intensity peak. The center of the blue peak falls on the $\omega_1 = \omega_3$ diagonal, and the red peak is shifted by the anharmonicity along the ω_3 axis.

1.2 Carbon Capture and Storage

Carbon dioxide (CO_2) makes up only around 0.04% of the atmosphere but readily absorbs infrared radiation, which makes it uniquely adept at trapping heat. CO_2 is a common byproduct of countless chemical processes, most prevalently the combustion of fossil-fuels, but also caused by the iron and steel, cement, oil refining and natural gas industries.[1–3] As dependence on these technologies grows, the concentration of CO_2 and, thereby the amount of heat trapped, has become a grave concern.[4–6]

While clean energy technology is far more varied and accessible than it was several years ago, reducing CO_2 and other greenhouse gas emissions needs to be addressed more immediately. Post-combustion CO_2 capture and storage (CCS) is one of several solutions to the carbon crisis.[1–3,7]This process contains several steps: capture, transport, storage, and utilization. Of these steps, the first is the most critical: selective collection of CO_2 from mixed exhaust streams.

There are operational solutions already in use. Amine absorption is the most mature of these technologies and is in commercial use in some places.[1,8,9] Amine absorption works through two main reactions. The first is the selective absorption of CO_2 by a liquid-phase amine reagent, most commonly monoethanolamine (MEA). The second step is the regeneration of the MEA solvent.[10] This process suffers from both oxidative and thermal degradation as well as the toxicity and corrosiveness of the reagents. There is development underway to optimize this process; however, few have proceeded past bench-scale experiments.[1]

While amine-based technologies are mature and available,[8,9] research has progressed towards new materials for post-combustion carbon capture with better chemical stability, smaller plant-footprints, and lower overall costs. Development focuses on several categories of industrial importance: uptake under adsorption conditions, working capacity, selectivity under adsorption conditions, and regenerability.[1–3]

There is interest in understanding fundamental properties and behaviors of CO_2 and its interaction with various matrices in the hope of informing development of CCS materials. 2D-IR spectroscopy has proven to be a powerful, information-dense tool to use in investigating CO_2 (and other chromophores) on a molecular scale in a variety of systems.

1.3 Investigation at the Molecular Level

2D-IR spectroscopy has been used to study a wide variety of chromophores (H_2O, SCN^-, CO_2, N_2O, Amides, Carboxylates) in a wide variety of systems (bulk solvents, surfactant solutions, ionic liquids, proteins, and polymers).[11–28] 2D-IR spectroscopy investigates the vibrational frequency fluctuations of an IR-active chromophore on the time- and length-scales of molecular vibrations. Said best by Brinzer et al., it investigates 'CO_2's molecular environment from CO_2's point of view'.[17] This level of detailed information is a window into the local environment around a chromophore.

The local environment of a chromophore is a measurement that occurs on extremely short length scales and extremely fast timescales, but the overall processes are governed by the same properties that govern bulk properties and dynamics. Onsager's regression hypothesis tells us as much: the average regression of fluctuations will obey the same laws as the corresponding macroscopic irreversible process.[29,30] Additionally, using the fluctuation-dissipation theorem, it is possible to derive a relation between a bulk transport coefficient, such as diffusion, to an auto-correlation function for viscosity.[31,32] These relationships underlie both the power and the usefulness of 2D-IR spectroscopy as an investigative technique.

While investigating the association between local dynamic processes and bulk processes is one interesting avenue, there is also a synergistic relationship between 2D-IR spectroscopy and molecular modeling. 2D-IR observables (linewidth, spectral diffusion timescales, reorientation information) offer a broad range of information about the chromophore and its environment. Theoretical calculations and molecular modeling can deepen the understanding of the results. Conversely, the spectroscopic observables offer a mechanism by which to validate computational results.[33–36]

1.4 Carbon Capture Materials of Interest

1.4.1 Ionic Liquids

Ionic liquids (ILs) are also referred to as room temperature molten salts: typically large, permanently-charged ion pairs that are liquid at room temperature. They are of interest in many industries including carbon capture, natural gas sweetening, chemical catalysis, hydrogen storage and batteries.[3,37–41] Ionic liquids drew the attention of the carbon capture industry for their chemical and thermal stability and their tailorable affinity for CO_2.[3,39,42–45]

2D-IR spectroscopy has been used to investigate the interaction between ionic liquids and CO_2.[17,33,35,46,47] Observations include a dependence of CO_2 antisymmetric stretch frequency (ν_3) on anion, which, supported by density functional theory calculations, suggests that CO_2's frequency dynamics are directly impacted by the motion of the cations and anions around it and, therefore, that CO_2 reports on its interactions with its surroundings.[17] Using a combination of quantum chemical calculations, and experiment, time scales of motion were related to variation both in electrostatic interaction with the environment (such as charge transfer) and non-electrostatic interactions (such as geometric distortion). Given the correlation between initial timescales of relaxation and bulk viscosity in ionic liquids, it was proposed that the dynamics sensed by CO_2 were correlated with anion diffusion.[17,33–36]

Using molecular dynamics simulation coupled with 2D-IR experiments, it was determined that CO_2 inherently samples a charge-dense region of the ionic liquid, where its quadrupole is stabilized, and the timescales of molecular motion would therefore depend on the breakup of ion cages around the CO_2 molecule.[48,49] This is similar to results obtained utilizing polarization-controlled pump-probe spectroscopy. The Fayer group was able to measure population relaxation and anisotropy of CO_2 in imidazolium ILs. CO_2 dynamics occurred on two distinct timescales, interpreted as restricted angular diffusion (wobbling-in-a-cone) and a complete rotational randomization.[46,50]

Ionic liquids have numerous advantages for carbon capture applications, including variety, tunability, and versatility.[40,51,52] Imidazolium-based ionic liquids show very high selectivity for CO_2 over other common gases (N_2, H_2, CH_4).[42,53–55] However, among the most commonly cited downfalls of ionic liquids for carbon capture is high viscosity, which can require the use of high pressures and generate a significant energy cost.[40,56] One solution is to combine the high CO_2 selectivity of ILs with a high-permeability technique, such as membrane separations.[5,57–61]

1.4.2 Membranes

An ideal functioning membrane would act as a molecular-scale filter that separates gas A from gas B with perfect efficiency.[62] As with many systems, the ideal case is not seen in reality; however, there are a number of membrane-based separations systems that show improved performance for gas separation and other industries, such as natural gas sweetening.[57,63–67] Membrane-based processes are advantageous from a thermodynamic perspective. With the correct combination of materials, such as with facilitated transport membranes, equilibrium limitations can be overcome.[1,65] Important characteristics of separation membranes include long term stability, permeability, and selectivity.[62,65]

The permeability and selectivity of a membrane are coupled characteristic quantities. The permeability, or how easily a given molecule is able to flow through the membrane, is related to the selectivity by the equation:

$$\alpha_{A/B} = \frac{P_A}{P_B}, \tag{1}$$

where $\alpha_{A/B}$ is the selectivity for gas A over gas B, and P_A and P_B are the permeability of gas A and B respectively.[68] These quantities are described by the Robeson limit, which empirically defines the trade-off between them.[69] Additionally, many membranes have very high diffusivity, but are not particularly selective for CO_2.[70,71] For this reason, many pure membranes are not ideal candidates for CO_2 sequestration. The combination of membranes and ionic liquids, offer a broad range of materials to investigate, some of which are very promising for CO_2 separations.[60,61,72–80]

1.4.3 Polymer-IL Composite Materials

Ionic liquid-polymer composites are a rapidly growing research area for separations.[1,74,81–84] In addition to the sheer number of ILs and polymers, there are multiple methods of creating the composite material, some of which are better suited to gas separations than others.[58,74,81]

IL-polymer composites are often categorized by the method of synthesis, or the type of force used to bind the ionic liquid to the polymer. The supported ionic liquid membrane (SILM) is a type of composite where the ionic liquid is mostly bound via capillary forces.[72,85] This method of trapping the IL is vulnerable to a high pressure differential; transmembrane pressures that exceed the capillary force can cause the IL to vacate the membrane, which is a limiting factor in their usefulness for gas separations applications.[74]

2D-IR spectra have been measured of both CO_2 and $SeCN^-$ in SILMs.[86–88] The results showed a splitting of the CO_2 antisymmetric stretching mode into two peaks, one that corresponded to the polymer phase, and the other to the ionic liquid phase in the pore membrane. While they report significantly slowed dynamics in the polymer-phase CO_2, they also still report a discrepancy between the relaxation timescales of the IL-phase CO_2 and bulk CO_2, which agrees with experiments on water in reverse micelles, where even when the size of the confinement was large, spectra still showed the effects of confinement.[86,89–91]

Another method for blending polymers with ionic liquids is to create poly-ionic liquids (PILs).[73,81,92–94] These materials are composed of covalently bound chains of the cation, the anion, or both ions. In some cases, success has been found adding some proportion of free ionic liquid to the PILs as well.[92] These materials show high selectivity and excellent gas transport properties, but can be expensive to manufacture.[74,81]

The polymer-IL composite that will be discussed in depth in this thesis is the ion gel, which falls somewhere between the SILM and the PIL.[60,81,95] In this work, ‘ion gel’ refers to a material that is made by physical mixing of cross-linking oligomer or polymer chains, a photoinitiator, and a compatible ionic liquid. Once mixed, the solution is then cross-linked to form a solid gel. The final consistency of the gel is dependent on the choice and ratios of polymer and ionic liquid used. Ideal combinations produce flexible gels with no visible exudate.[60,61]

The abundance of choice in this field leads to a desire for a better understanding of how CO_2 interacts with separation candidates.[16,17,46] Eliminating materials by measuring diffusivity, selectivity and permeability of various candidate membranes is one method of determining the best candidates for CO_2 separations applications.[52,60,61,70,96] If we can understand how CO_2 interacts with materials of varying design and function on a microscopic level, we can perhaps create yet more specific evaluation criteria.

Here, we investigate CO_2's microscopic environment in several polymer and polymer-ionic liquid composite systems. 2D-IR of CO_2 dissolved in an ionic liquid, a polymer, and the 50% by volume (vol%) reveals an unexpected and previously unreported vibrational energy relaxation pathway, which leads to an expansion of the model used to describe the intramolecular vibrational relaxation in CO_2.

In addition to the three polymer/ionic liquid compositions that were examined, a series of vol% mixtures are prepared and 2D-IR is measured in each of them, often with replication. This data set revealed a non-monotonic trend in dynamics timescales, which we describe using a core-shell-matrix model.

Polarization controlled experiments of CO_2 in an ion gel emphasizes reorientation induced spectral diffusion (RISD). In addition to successfully modeling RISD using a wobbling-in-a-cone model with second-order Stark Effect approximation (appropriate for quadrupolar systems), the frequency dependence of anisotropy is exemplified in both experimental data and a Gaussian joint probability density model.

Poly(vinyl acetate) (PVAc) and Poly(methyl acrylate) (PMA) despite structural similarity have different bulk CO_2 interaction behavior. PVAc is highly soluble in supercritical CO_2 but the same is not true of PMA. 2D-IR measurements in these materials reveal similar spectral diffusion timescales, but different intramolecular kinetics, implying that the variation in CO_2 interaction behavior begins at molecular-length scales.

The nuances of how CO_2 interacts with the materials intended for its separation and capture likely govern, and can be used to optimize, carbon capture and storage processes. We offer physical interpretations of the complex data measured with which we aim to provide a more complete understanding of both the separation matrices and the chromophore in question.

2.0 Ultrafast 2D-IR Theory

Extracting, analyzing, and reporting the information gained in 2D-IR spectroscopy draws on the underlying quantum and statistical mechanics of the processes occurring. Here, we will start with a simulated, CO_2-like 2D-IR spectrum and work backwards to understand the importance of frequency fluctuation correlation functions, response functions, and Liouville space pathways. Once we have established the theoretical basis, we will examine phenomenological influences: intramolecular kinetics, population relaxation, and orientational effects.

2.1 Analysis-based Approach: 2D-IR Theory

2.1.1 2D-IR Spectroscopy: Qualitative Overview

The utility of 2D-IR spectroscopy is the result of a real system's deviation from the harmonic oscillator model. For a harmonic oscillator, there is identical spacing between energy levels, which would lead to effectively no signal in a 2D-IR experiment, as the blue (negative) and red (positive) peaks would overlap. For a weakly anharmonic oscillator, the separation between the two peaks is the result of anharmonicity. For CO_2, the primary chromophore discussed in this work, the anharmonicity value is ~ 24 cm^{-1}. This generates distinct and well-defined peaks.

The vibrational potential energy surface of many real systems can be modeled as an anharmonic, three-level system: ground state, first excited state, and second excited state. These states are denoted most commonly as a ket, with the relevant state enumerated (*i.e.* the ground vibrational state is $|\nu_0\rangle$, or $|0\rangle$). In a simple, three level system with adequate anharmonic separation, there is one blue peak corresponding to ground state bleach and stimulated emission pathways (Figure 2.1a,b) and one red peak corresponding to excited state absorption (Figure 2.1c).

2D-IR spectra are generated from a sequence of three infrared pulses and the resulting

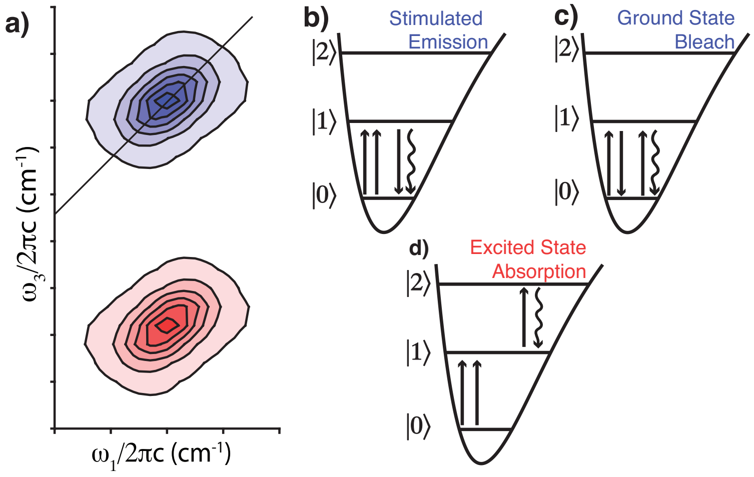

Figure 2.1: Three major pathways generate the two observed peaks in 2D-IR spectroscopy. (a) 2D-IR spectrum simulated at 200 fs, using a Bloch-Kubo lineshape function (equation 10) with $\Delta = 2.0$ cm^{-1}, $T_2 = 3.5$ ps, and $\tau = 60$ ps, with a small amount of randomly generated noise added. The resulting spectrum includes two peaks, separated by anharmonicity, one negative (blue) peak and one positive (red) peak. (b), (c) Vibrational energy pathways that generate the blue (negative) peak. (d) Vibrational energy pathway that generates the red (positive) peak.

molecular response. Signal measured over t_1 is Fourier transformed to create the initial frequency axis, ω_1. After the waiting time, t_2, a third pulse (the probe) excites the sample and then a signal is emitted. This signal is detected in the frequency domain using an array detector and is plotted on the final frequency axis, ω_3.

The shape of a peak in the 2D-IR spectrum reflects the level of frequency-frequency correlation in the system for the t_2 at which it was measured. The shape of these peaks changes over time. This process is known as spectral diffusion and is the randomization of the frequency space occupied by the chromophore as a function of time. This randomization is due to a loss of overall molecular memory. At very short waiting times, peaks show a high degree of correlation as molecules retain more memory of their initial frequency. As the waiting time increases, the peak loses this correlation on system- and chromophore-dependent timescales, which are usually referred to as structural reorganization times or frequency fluctuation correlation times.

These correlation timescales can reflect a variety of interactions between the chromophore and its environment. Measuring the change in shape of the peak is a reproducible method of obtaining information about frequency fluctuation timescales, which is useful when dynamics are the main target of the measurement. For experiments with a broader scope (*i.e.* rotational motion, cross-peak analysis, or intramolecular kinetics), extracted timescales can then be used as input values for a response-function-based spectral calculation, which generates simulated spectra to compare with experiment.

2.1.2 Analysis Method: Change of Shape

There are a number of ways to extract the correlation time of a 2D-IR experiment without a full response function calculation. Common methods include center line slope (CLS)[97–99], ellipticity[100], phase slope, and the inhomogeneity index[101]. Qualitatively, each of these methods provides similar information content.[101] Here, we will discuss the CLS method in detail, as it is used most commonly throughout this work.

CLS analysis is a fast, reproducible, and rigorously investigated method for extracting dynamics from the change of shape in the peaks.[97–99] This method generates slices of the data along the initial frequency (ω_1) axis and fits a line through the minima of the blue (negative) peak (Figure 2.2). The slope of this line is referred to as the "center line slope". This slope, over time, will decrease from its initial value toward, and will even reach, 0 in some cases. The correlation changes over time, and these correlation values (Figure 2.2b, points) are typically fit to a single, bi-, or triexponential model, depending on the complexity of the relaxation process for a given chromophore (Figure 2.2b, solid line).

These models provide a quantitative value of the dephasing time (a measure of initial correlation loss), correlation amplitude (how much correlation is lost during the experiment), and the frequency fluctuation time constant(s). The CLS method does not include a value for the linewidth, as the measure only takes into account the peak minima. This linewidth can, in most cases, be calculated from a linear IR spectrum, and new methods are being

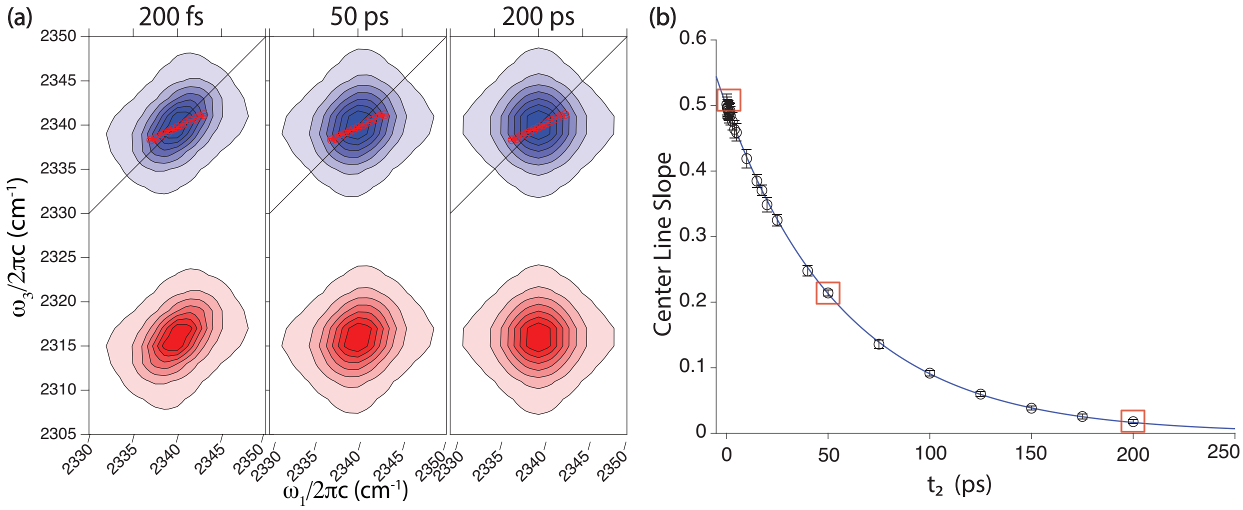

Figure 2.2: One method for tracking the change of shape of 2D-IR peaks over the course of an experiment is center line slope (CLS). (a) Data (simulated as described in figure 2.1) simulated at three t_2 waiting times: 200 fs, 50 ps, and 200 ps. The red line connects the minima of several slices along the ω_1 axis. The slope of the center line reflects the degree of correlation. (b) A plot of CLS values (slope of red lines) at each of several simulated waiting times. This curve (points), fit to an exponential (line), extracts quantitative time constants for frequency fluctuations.

developed that employ machine learning to generate this information where needed.[99]

The CLS method benefits from the analytical simplicity and robustness. Since looking only at the minima (or maxima) of peak slices, it is not influenced by factors that might affect lineshape, such as apodization.[98,99] Generally, when compared with a more comprehensive method of spectral analysis, the time constant(s) agree well.[101]

Simulating a spectrum using response function formalism requires making an educated guess at both the lineshape function and the correlation function. Analysis of the linear IR spectrum and a CLS analysis can be useful tools in determining the form of the lineshape function that will then be propagated through the simulation process.

2.1.3 Analysis Method: Response Function-based Simulation

2D-IR spectra are the product of quantum and statistical mechanical processes and, as such, can be calculated. This predicted spectrum can then be fit to the experimental spectrum in order to extract quantitative information. To perform this kind of fitting, it helps to understand how the equations used to calculate 2D-IR spectra are derived.

This section aims to explain the response-function based simulation process for a simple three-level system, which maps well onto the potential energy surface and 2D-IR spectra of many real chromophores.

2.1.3.1 Electric Field Interactions and Molecular Response

Vibrational spectroscopy functions as a result of the interaction between light and matter. Light at the resonant frequency of a vibrational mode optically excites that chromophore. At this wavelength, the electric field of the pulse, $E(t)$, interacts with the transition dipole moment, $\hat{\mu}$. This interaction can be treated as a time-dependent perturbation.

$$\hat{W}(t) = -\hat{\mu} \cdot E(t) \tag{2}$$

To measure the interaction strength, the macroscopic polarization ($P(t)$) is calculated. $P(t)$ is the emission field that oscillating charges generate. The term $\hat{W}$ is effectively the quantum mechanical operator for the interaction energy between the incident electric field and the molecular dipole. To calculate the macroscopic polarization, we determine the expectation value of the transition dipole.

$$P(t) = \langle \hat{\mu} \rangle = \langle \Psi(t) \; |\hat{\mu}| \; \Psi(t) \rangle \tag{3}$$

The probability of transition is subject to vibrational selection rules. So, for a system of vibrational energy states $|0\rangle$ and $|1\rangle$, the expectation value scales with both the transition dipole strength and the probability of transition.

The full derivation is described in detail elsewhere,[11] but the important outcome of this is:

$$P(t) \propto c_0 c_1 \mu_{01}^2 \sin \omega_0 t. \tag{4}$$

The intensity of the macroscopic polarization is a sine wave scaled by the strength of the transition dipole moment (μ_{01}). The resulting signal is measured as $\cos \omega_0 t$ after a 90° phase shift caused by a sheet of oscillating dipoles.[102]

2D-IR spectroscopy is an ensemble measurement, so molecules in the beam path interact with the applied electric field. To account for this, rather than looking at a single transition dipole, we look at the ensemble average. In order to keep track of these interactions, a density matrix formalism is used,

$$\rho = \begin{pmatrix} \rho_{00} & \rho_{01} \\ \rho_{10} & \rho_{11} \end{pmatrix}. \tag{5}$$

The density matrix is the outer product of the wavefunction and its conjugate ($|\Psi\rangle\langle\Psi|$). The populations in each density matrix element correspond to different transition pathways. ρ_{00} and ρ_{11} are both constant quantities, where the ket and bra vibrational states are the same (population states). The off-diagonal elements, however, represent coherences: population split between two vibrational energy levels. c_0 and c_1 are coefficients, c_n, that scale the contribution of each (n) vibrational energy state to the coherence. These oscillating terms have the form:

$$\begin{aligned} \rho_{01}(t) &= -ic_0 c_1 e^{i\omega_{01} t} \\ \rho_{10}(t) &= ic_0 c_1 e^{-i\omega_{01} t}. \end{aligned} \tag{6}$$

Theoretically, at 0 K and before the first pulse, the density matrix has $\rho_{00} = 1$ and all other elements are 0. The electric field interactions then send population through one of two transition pathways:

$$\begin{aligned} \rho_{00} \rightarrow \rho_{01} \rightarrow \rho_{00} \\ \rho_{00} \rightarrow \rho_{10} \rightarrow \rho_{00}. \end{aligned} \tag{7}$$

For a two-level system, with only a single electric field interaction, these pathways are easily described as above: the pulse of light sends the ensemble into a coherence state (ρ_{01} or ρ_{10}) that oscillates until the energy is lost and the system returns to the ground state. When more energy levels are accessible, so too are more transition pathways. It can become tedious to keep track of them. These pathways are referred to as Liouville space pathways and are depicted by double-sided Feynman diagrams.

2.1.3.2 Liouville-space Pathways and Double-sided Feynman Diagrams

A three level vibrational system contains a ground state ($\nu = 0$), first excited state ($\nu = 1$), and second excited state ($\nu = 2$). To generate the pattern of peaks shown above (Figure 2.1), six double-sided Feynman diagrams are required. These six Feynman diagrams survive the rotating wave approximation, which allows us to disregard nonphysical, rapidly oscillating terms and simplify the expressions used to represent these interactions.[11]

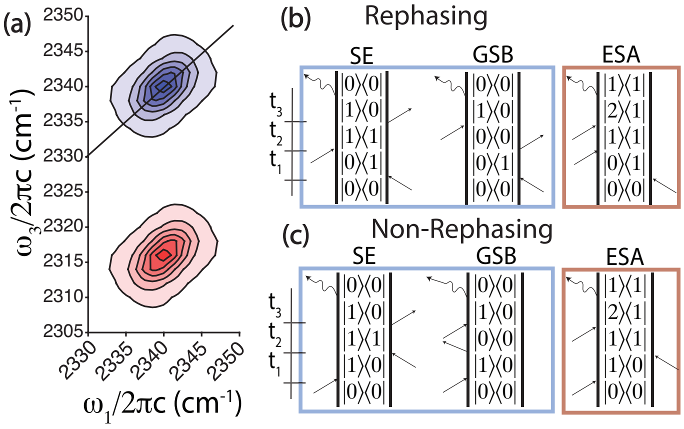

Figure 2.3: The 6 double-sided Feynman diagrams that generate the 2 peaks in a typical 2D-IR spectrum. Stimulated emission (SE) and ground state bleach (GSB) make up the blue peak, while excited state absorption (ESA) generates the red peak. (a) Spectrum simulated using similar parameters to CO_2 in an ionic liquid at early t_2 times. (b) Rephasing diagrams. (c) Non-rephasing diagrams.

The six diagrams are broken up into rephasing and non-rephasing pathways. Rephasing refers to pathways through the system where the frequency of the coherences during t_1 and

t_3 have opposite signs. This allows the system to rephase and generate a photon echo. Non-rephasing pathways do not flip the sign of their coherence from t_1 to t_3. The combination of the two is what is measured in the experiments described here, and what must be calculated.

At very long times, to model total vibrational relaxation, at least one additional diagram is necessary to account for the total loss of energy from the system to the bath. Additional diagrams also become necessary when there are more vibrational modes involved, which will be explored in detail in chapter 4.

Double-sided Feynman diagrams track the flow of population through a given pathway. Each diagram is composed of vertical bars, which represent increasing time from bottom to top. The density matrix is depicted as $|\nu\rangle\langle\nu|$, and arrows are used to indicate interaction of the pulses. An arrow pointing towards the density matrix indicates a climbing up of the vibrational ladder, and an arrow pointing away indicates the opposite. These response functions, described in the next section, include information about the lineshape, the correlation time, and the interaction intensity between the laser and the chromophore. Modulating these factors allows for a consistent method of modeling experimental spectra.

2.1.3.3 Calculating a 2D-IR Spectrum

The molecular response measured (and depicted in figure 2.3) is dependent on both the lineshape of the spectra (such as what is measured in CLS, above) and the molecular response pathway that population takes as a result of interaction with the incident electric field.

The response functions take many forms but can be represented generally. The total third order response includes both rephasing and non-rephasing pathways:

$$\begin{aligned} R_r(t_1,t_2,t_3) &= (-1)^m \mu_B^2 \mu_A^2 \exp(-i\omega_A t_1 + i\omega_B t_3 + i\phi) \exp(-g(t_1) + g(t_2) - g(t_3) \\ &\quad - g(t_1+t_2) - g(t_2+t_3) + g(t_1+t_2+t_3)) \qquad \text{(rephasing)} \qquad (8) \\ R_{nr}(t_1,t_2,t_3) &= (-1)^m \mu_B^2 \mu_A^2 \exp(-i\omega_A t_1 - i\omega_B t_3 - i\phi) \exp(-g(t_1) - g(t_2) - g(t_3) \\ &\quad + g(t_1+t_2) + g(t_2+t_3) - g(t_1+t_2+t_3)) \qquad \text{(non-rephasing)} \qquad (9) \end{aligned}$$

where ω_A is the frequency of oscillation during t_1, ω_B is the frequency of oscillation during t_3, m is the number of arrows on the right of the diagram (the bra side), μ_A is the transition dipole from the first two interactions, μ_B is the transition dipole from the second two interactions, ϕ accounts for residual phase error in the measurement, and $g(t)$ is the lineshape function.

Lineshape functions take many forms. In most of the work herein, we use a Bloch-Kubo lineshape with a fast (homogeneous) mode and an intermediate (spectral diffusion) mode:

$$g(t) = \frac{t}{T_2} + \Delta^2\,\tau^2\left(e^{-t/\tau} - 1 + \frac{t}{\tau}\right). \tag{10}$$

Here, T_2 is the dephasing time, which represents motions too fast for the experiment to capture. τ is the representative correlation time for the system, and Δ is a measure of peak width, which represents the spread of frequencies encompassed by the 2D-IR peak.

These response functions generate a time-domain spectrum that can be Fourier transformed to obtain a frequency domain spectrum that can be directly compared to the experimentally generated spectrum.

2.2 Phenomenological Additions

A response function includes the interaction of an ensemble of chromophores with an incident pulse of light and terms that reflect the evolution of this interaction over time. Experimental 2D-IR spectra can show a variety of behaviors that are not included in the response functions as described above. The process of accounting for a few of these behaviors (population relaxation, intramolecular kinetic exchange, and orientational dynamics) are described in this section.

2.2.1 Population Relaxation

At very long times, an excited chromophore will return to the ground state. This process results from exceeding the vibrational lifetime of the chromophore. By the time the probe pulse interacts, the system has returned back to equilibrium. For molecules such as CO_2, this can happen via inter- or intramolecular pathways. This process is called population relaxation and is also not directly addressed in the pure forms of the response functions.

Depending on system complexity, population relaxation may be represented as a single exponential:

$$e^{-t_2/T_1}, \tag{11}$$

where t_2 is the experiment waiting time and T_1 represents an overall population relaxation time. This value can be achieved in a few ways. The exponential term can be added as a product with the response function, and a value can be extracted using the global fitting methods. Alternatively, where polarization control (see below) is available, an isotropic signal can be calculated. The T_1 can be estimated as the timescale of signal intensity drop-off, once rotational effects have been removed.

For some cases, such as CO_2, it can be necessary to use a more complex form for vibrational relaxation. Chapter 4 will discuss the derivation of the four double-sided Feynman diagrams that outline the population relaxation processes for CO_2. These diagrams and pathways are all accounted for during the process of extracting intramolecular kinetics and take the place of the T_1 exponential.

2.2.2 Intramolecular Kinetic Exchange

2D-IR spectroscopy typically operates by exciting a specific vibrational band and tracking the response of molecules once the vibration is induced. Only diatomic molecules have a single vibrational mode. Because triatomic molecules have three vibrational normal modes, it is possible for energy to transition to other modes without probing them specifically. 2D-IR spectroscopy is sensitive to the initial and final frequency of the measured populations and, therefore, sensitive to population transfer between modes. This process often results in cross-peaks, which have different initial and final frequencies.

For CO_2 in the condensed phase, the IR active antisymmetric stretch (ν_3) has an absorbance frequency around 2340 cm^{-1}. This peak in the linear IR spectrum has a shoulder, shifted about ~ 12 cm^{-1} lower than the center frequency of the main band. This shoulder peak (about 7% as intense as the main band) is the result of thermal population of the degenerate ν_2 bending mode.[17,46]

The resulting 2D-IR spectrum shows both a shoulder peak at short times and cross-peaks that result from energy transfer between the ν_3 and shoulder modes. To comprehensively account for this type of energy transfer, an additional set of Feynman diagrams was derived (chapter 4) and the response for these diagrams are also calculated.

To account for kinetic exchange during the t_2 time, a kinetic matrix also needs to be derived. Here, we will describe a simple equilibrium system, such as the up-down kinetics between the antisymmetric stretch ground state, $|0\,0\rangle$, to the ground state of the thermally excited shoulder, $|1\,0\rangle$. Here, the ket represents $|\nu_2\,\nu_3\rangle$ or the number of quanta of energy in each relevant CO_2 vibrational mode.

In this case, we have only two kinetic terms, k_u and k_d. These refer to the flow of energy up ($|0\,0\rangle \rightarrow |1\,0\rangle$) and down (($|0\,0\rangle \rightarrow |1\,0\rangle$). The population of two states is thus important to this analysis: $|0\,0\rangle$, denoted p_{00} and $|1\,0\rangle$, denoted p_{10}. These states gain or lose population as a function of kinetic pathways available:

$$\frac{dp_{00}(t)}{dt} = -k_u\; p_{00}(t) + k_d\; p_{10}(t) \tag{12}$$

$$\frac{dp_{10}(t)}{dt} = k_u\; p_{00}(t) - k_d\; p_{10}(t) \tag{13}$$

Integrating both sides of the equation results in an exponential function. If we combine all of the kinetic coefficients into a matrix and all of the populations into a vector, it allows the system to be solved analogously to solving for eigenvalues. The resulting system will have the form:

$$V(t) = e^{\mathbf{K}t}V(0), \tag{14}$$

where $V(t)$ is a time-dependent vector of populations, $\mathbf{K}$ is the matrix of kinetic terms, and $V(\mathit{0})$ is a vector of the initial populations of the system.

In the example above, $\mathbf{K}$ is 2x2 matrix of the form:

$$\mathbf{K} = \begin{bmatrix} -k_u & k_d \\ k_u & -k_d \end{bmatrix}, \tag{15}$$

which corresponds exactly with the alignment of kinetic terms in equations 12 and 13. The initial and final population vectors are then defined as:

$$V(t) = \begin{bmatrix} p_{00}(t) \\ p_{10}(t) \end{bmatrix}, \tag{16}$$

for the appropriate value of t.

The process of diagonalizing and solving for the eigenvalues of $e^{\mathbf{K}t}$ is lengthy; using symbolic math functionalities in MATLAB, we are able to obtain the form of $V(t)$ in terms of k_u, k_d, p_{00} and p_{10}:

$$V(t) = \begin{bmatrix} p_{00}(0)\frac{k_d+k_u*e^{-k_u*t-k_d*t}}{k_u+k_d} + p_{10}(0)\frac{k_d-k_d*e^{-k_u*t-k_d*t}}{k_u+k_d} \\ p_{00}(0)\frac{k_u-k_u*e^{-k_u*t-k_d*t}}{k_u+k_d} + p_{10}(0)\frac{k_u+k_d*e^{-k_u*t-k_d*t}}{k_u+k_d} \end{bmatrix}. \tag{17}$$

At room temperature, the energy gap (Δ_{cm}) between the $|0\,0\rangle$ and $|1\,0\rangle$ states is approximately the frequency of the pure bending mode, 667 cm^{-1}. Knowing this energy gap and the relevant temperature allows us to create boundary conditions for values of k_u and k_d for this system.

$$k_{eq} = 2e^{-\Delta_{cm}/k_BT}, \tag{18}$$

where k_B is the Boltzmann constant and T is temperature, and

$$k_{eq} = \frac{k_u}{k_d} \tag{19}$$

are used to generate these boundaries.

For CO_2 at room temperature, this result shows that around 7% of the population from the total ground state, $|0\,0\rangle$, crosses the manifold to the bending ground state.

Each component of equation 17 is applied to the relevant Feynman diagram(s) during response function calculations. Intramolecular vibrational relaxation (IVR) is assumed to occur during the waiting time, t_2. As such, $V(t)(1)$ would be applied to diagrams where population is in the total ground state after interaction with both pump pulses.

The time-dependent values augment the relative intensities of the calculated peaks. After calculation, the values of k_u and k_d are then adjusted by nonlinear least squares fitting to ensure the best possible agreement between simulation and experiment.

CO_2's intramolecular vibrational landscape includes an additional two kinetic coefficients, as well as the relevant excited states of the system described above. Chapter 4 describes the derivation and application of a more complete model for CO_2's IVR but is based on principles described here.

2.2.3 Orientational Dynamics

Above, in equation 2, we established that a molecular response results from the interaction of a transition dipole moment and an electric field. The interaction strength between a transition dipole moment, $\hat{\mu}$, and the polarized, incident laser field, $\hat{E}$, scales with the dot product of the two vectors.

Figure 2.4 shows two example cases of orientation distribution in a population of CO_2 molecules. On the left is an approximately isotropic distribution: the molecules (and thereby their transition dipole moment, which aligns with the bond) are oriented randomly with respect to the polarized electric field. The right shows one variation on an anisotropic distribution. In this case, all of the molecules are aligned with the electric field. Were all the molecules to align perfectly perpendicular to the electric field, however, that would also be anisotropically distributed.

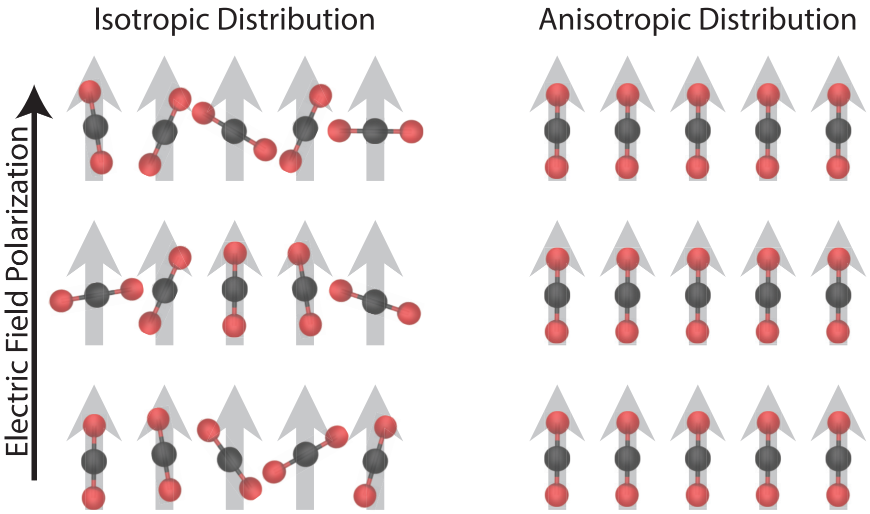

Figure 2.4: Examples of isotropic vs anisotropic distributions.

For a pulse polarized perpendicular to the laser table (denoted here as $\hat{Z}$ polarization), the angle between the pulse and the orientation of a transition dipole is denoted as θ, and the strength of the interaction scales with $\cos(\theta)$.

To consider the strength of the interaction between the electric field ($\hat{E}$) and $\hat{\mu}$, we first define the polarizations: $\hat{Z}$ and $\hat{X}$, where the $\hat{Z}$ or $\hat{X}$ represent the polarization of each incident pulse. Using the dot product between $\hat{\mu}$ and $\hat{E}$, amplitude differences arise between combinations. When we make an assumption that the dipoles are allowed to reorient and factor in the variable spatial orientation, we can derive an expression for the magnitude of the emitted signal that includes the rotational diffusion constant, D, and the time delays.

Assuming that t_1 and t_3 are infinitely short, such as in a pump-probe style experiment, we arrive at:

$$\langle \hat{Z}\hat{Z}\hat{Z}\hat{Z} \rangle \propto \frac{1}{45}[4e^{-6Dt_2} + 5] \tag{20}$$

where $\langle \hat{Z}\hat{Z}\hat{Z}\hat{Z} \rangle$, representing the parallel configuration, is the expectation value of the magnitude of signal generated by four interactions of a $\hat{Z}$ polarized electric field with the transition dipole moment.

For the perpendicular case:

$$\langle \hat{Z}\hat{Z}\hat{X}\hat{X} \rangle \propto \frac{1}{45}[5 - 2e^{-6Dt_2}] \tag{21}$$

which, assuming the magnitude of the electric field and $\hat{\mu}$ are the same in both cases, gives a signal strength approximately $\frac{1}{3}$ as strong as the parallel case at $t_2 = 0$.[11]

$$\frac{\langle \hat{Z}\hat{Z}\hat{X}\hat{X} \rangle}{\langle \hat{Z}\hat{Z}\hat{Z}\hat{Z} \rangle} = \frac{1}{3} \tag{22}$$

During the course of an experiment, we have established that the frequency of vibration fluctuates and that 2D-IR spectroscopy is sensitive to this. Molecules can also rotate during an experiment, which causes a change in the angle θ. Probing with light that is perpendicularly polarized to the pump light weights the measurement towards those molecules that rotated. This is demonstrated in figure 2.5.

We're able to extract a value that is a measure of how ordered the dipole moments of the probed subensemble were at the beginning of the experiment and on what timescale(s)

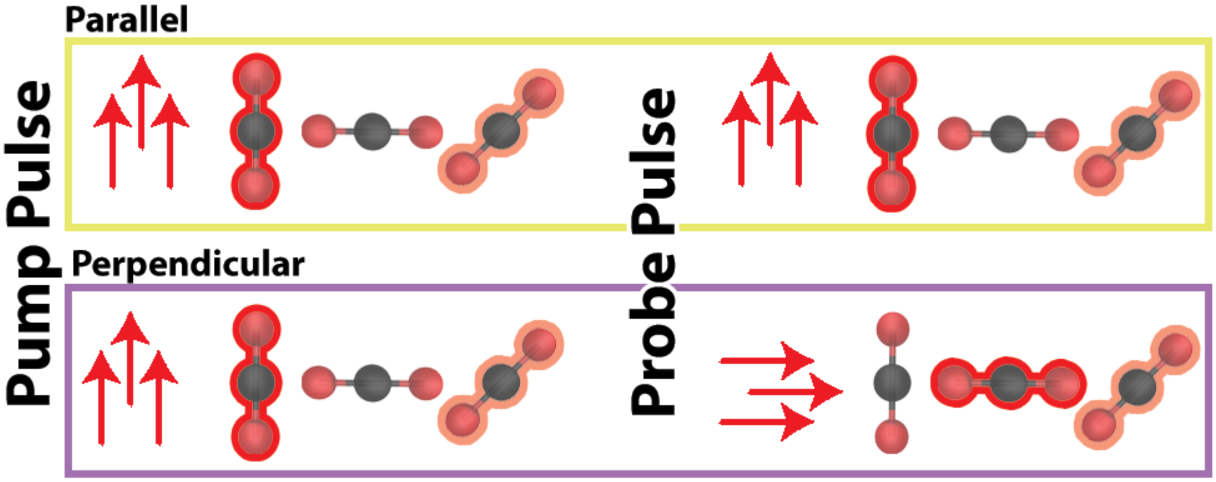

Figure 2.5: Changing the experiment polarization weights the measurement towards different populations.

they relax to the isotropic distribution. This information is obtained by calculating the anisotropy ($\alpha(t_2)$). The magnitude of the anisotropy is a measure of the probability of a transition dipole moment's rotation during the population time. Rotation into both the X- and Y-directions are accounted for by counting the signal strength of the perpendicular signal twice:

$$\alpha(t_2) = \frac{I_{\|} - I_{\perp}}{I_{\|} + 2I_{\perp}}. \tag{23}$$

$I_{\|}$ is the intensity of the parallel signal and $I_{\perp}$ is the intensity of the perpendicular signal at any given t_2 time. At $t_2 = 0$, the anisotropy is equal to its maximum value of 0.4. As the t_2 time increases, the anisotropy value will eventually decay to 0, at which point the transition dipoles have become essentially isotropic.

Anisotropy can be frequency dependent and the value $\alpha(t_2)$ can be calculated for each point in a 2D-IR spectrum ($\alpha(t_2) \rightarrow \alpha(\omega_1, t_2, \omega_3)$) using the intensity of the parallel and perpendicular signals at that frequency pair. We explore the origins of this frequency dependence in chapter 6.

The polarization-dependent molecular response reports an effect known as reorientation induced spectral diffusion, where in a perpendicularly polarized experiment (figure 2.5), spectral diffusion occurs faster than in a corresponding parallel experiment. This is due to the change in frequency distribution that is induced by the rotation of molecules.

This can be modeled for a dipole and quadrupole with a first- and second-order Stark shifts, respectively.[103] As CO_2 behaves like a quadrupole in ionic liquids[48], the second-order Stark shift approximation is used to model this behavior.

3.0 Methods

3.1 CO_2-loading and Sample Cell Design

All described experiments were performed with the sample housed in custom-built brass sample cells and sandwiched between two one (1) inch diameter calcium fluoride (CaF_2) windows. The windows are purchased from Crystran Ltd. The brass sample cells are manufactured by the Dietrich School of Arts and Sciences Machine Shop.

Two designs of brass sample cells were used at various stages of experimentation. The original design of the brass sample cell was intended for use with liquid samples, up to and including liquid flow cells (figure 3.1). The circular cell has a base and a lid, which is affixed with six equally spaced screws. The base of the cell has a cavity designed to hold and compress a pair of CaF_2 windows. The windows are protected from the brass by a 100 µm polytetrafluoroethylene (PTFE) spacer placed on either side of the window pair, which also improves the seal by increasing pressure along the edge of the windows. The windows are separated from each other by a similar PTFE spacer of varying depth depending on the desired path length for the sample.

For flow cells, drilled windows are used. The drilled windows have a pair of 0.7 mm holes drilled 16 mm apart through the window, which provide inlet and outlet pathways for the substance that is being flowed. The original designed sample cells had a pair of attachment points that aligned with the drilled holes. A length of flanged PTFE tubing was compressed against the glass by a polyethylene (PE) screw at both the inlet and outlet points. In most cases, this provided adequate seal and pressure for a liquid (most commonly, an aqueous solution) to be flowed.

Using CO_2 as a chromophore requires dissolving CO_2 into the material of interest. For liquid samples, such as ionic liquids or organic solvents, the desorption of CO_2 is slow enough that a pressurized loading of CO_2 before transferring the sample to the brass cell was sufficient. For pure ionic liquid samples, the IL is dried via vacuum pump for 1.5-3 hours and then bone dry CO_2 is loaded for 3-5 minutes. An aliquot of IL is transferred to the cell,

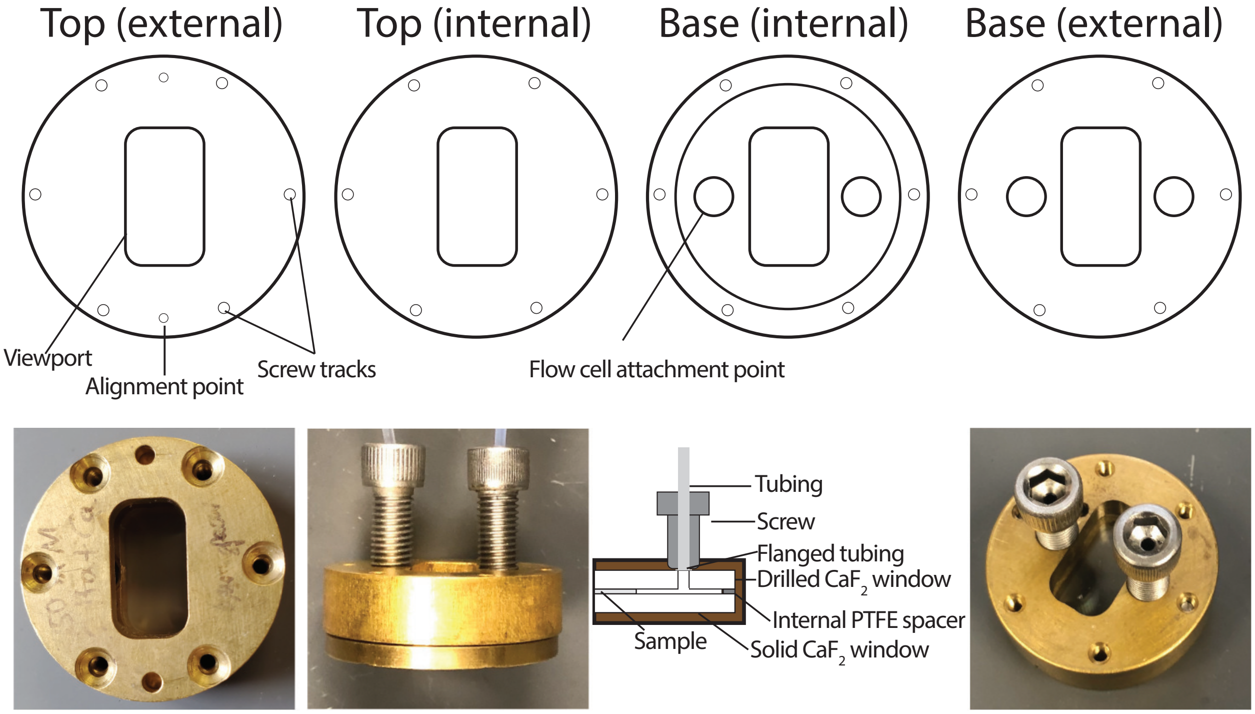

Figure 3.1: Original brass sample cell design.

pressed between two undrilled windows, and will then be adequately stable for the duration of an experiment.

Measuring 2D-IR spectra of CO_2 in a polymer was not particularly amenable to the methods used for ionic liquid samples. A series of alterations to both CO_2 loading procedures and the brass sample cell design were required. Initially, the original cell design was used as a gas flow cell. It was assembled as described above, with the addition of a layer of Parafilm® around the outer edges of the CaF_2 windows to help with leakage and stainless steel flow cell screws for a tighter seal around the flanged tubing (figure3.1).

The gas flow cell operated by flowing CO_2 into the cell, around the material, until the sample absorbed enough CO_2 for measurement. In most cases, a "maintenance flow" of CO_2 was also used during the 2D-IR experiment, in order to combat the fast diffusion and maintain a constant concentration of CO_2 in the material. This constant flow of CO_2 meant that a cell that failed to seal was leaking gaseous CO_2 into the purged environment and thereby obscuring the spectra being measured. Creating a sample cell that was adequately gas tight for experiment was time consuming, tedious, and offered many places for mistakes to be made in sample preparation.

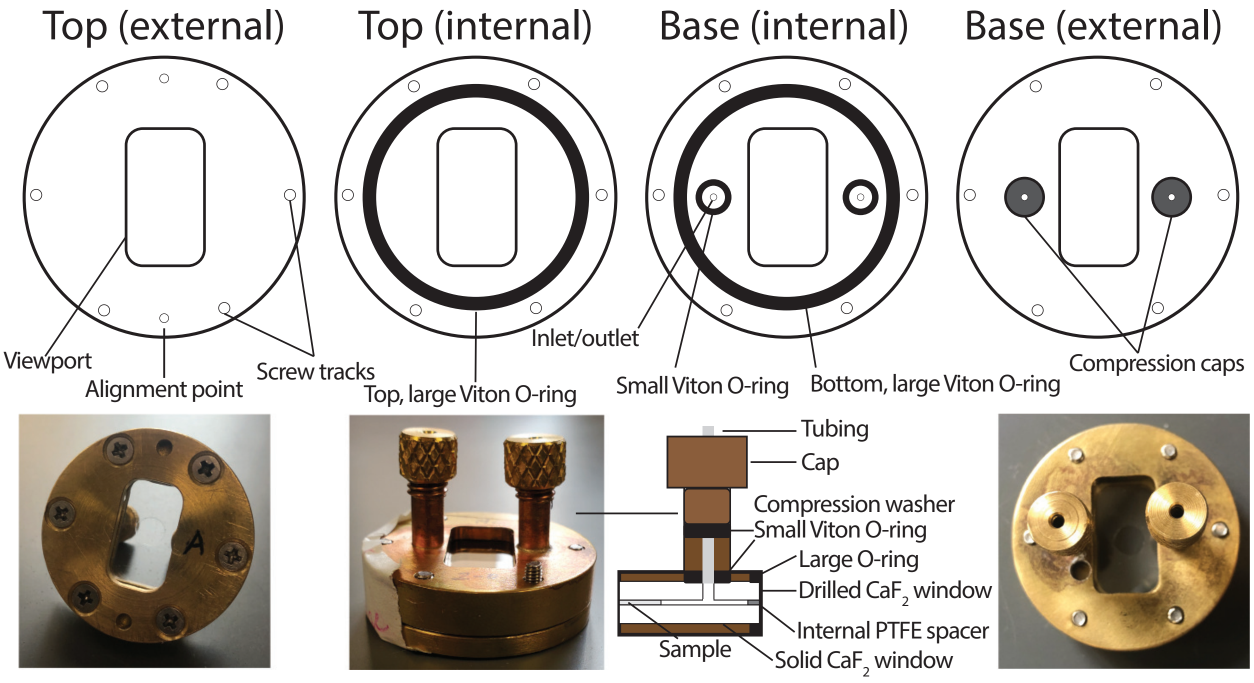

Figure 3.2: Updated brass sample cell design.

In November of 2018, the sample cell design was updated and new cells were manufactured (figure 3.2). These cells were designed with gas flow in mind and eliminated several of the previous trouble points: uneven flanges, the soft polyethylene screws (later replaced with stainless steel), and need for external PTFE spacers. The base and lid of the sample cell were modified to include a channel for a pair of larger Viton$^{\mathrm{TM}}$ O-rings that sandwiched the CaF$_2$ windows and offered more consistent pressure on the internal PTFE spacer, leading to a better seal.

The PE screws were replaced with brass necks that relied on compression of a number of Viton$^{\mathrm{TM}}$ O-rings to grip tubing and create an airtight environment. These cells performed far more consistently and were able to tolerate far higher gas flow pressures than their predecessors before beginning to leak.

Utilizing the improved cell design, a solid sample could be made, sealed into the brass cell, and then CO_2 flowed into the sample cell until the sample had taken up enough CO_2 for an experiment to be performed. The new cell design also reduced water exposure in situations where that was a concern. The updated cell design was successfully used for liquid flow cells for systems with a long enough path length that back pressure was not an issue.

3.2 2D-IR Workflow

2D-IR spectroscopy is measured utilizing an ultrafast laser system comprised of a Coherent Vitesse oscillator and a Coherent Legend Elite chirped pulse amplifier. These commercial systems generate 805 nm pulses of light at a 5 kHz repetition rate with a total energy output of around 5 W, and with a pulse duration of sub-200 fs. Approximately 1 W is directed into a home-built optical parametric amplifier (OPA),[104] where it can be tuned to the appropriate frequency for the experiment and directed into the 2D-IR spectrometer.

Generally in the OPA there are three important crystals that manipulate the incoming 805 nm light to generate mid-IR light needed to interrogate the chromophore of interest. The first step is white light generation, which occurs by focusing a small portion of the incoming light onto a sapphire crystal (figure 3.3a,b). The white light is then directed into a type II β-barium borate (BBO) crystal, where it interacts with the 805 nm light to undergo optical parametric amplification. The resulting signal is reflected back through the BBO a second time for further amplification. This process involves the conversion of a high frequency pulse into a lower frequency pulse and generates a third beam of light (referred to as the idler) at the difference between the frequencies (figure 3.3b,c) in order to conserve energy. The BBO is a birefringent crystal, and its angle is adjustable so that the frequency that is selected from the white light continuum is the appropriate energy to generate the desired mid-IR frequency after difference frequency mixing.

After the BBO, the final major optical process in the OPA is difference frequency mixing, which occurs in an $AgGaS_2$ crystal. In this optical process, a new beam is generated at the frequency difference between the incoming beams (figure 3.3c,d). This is the final desired

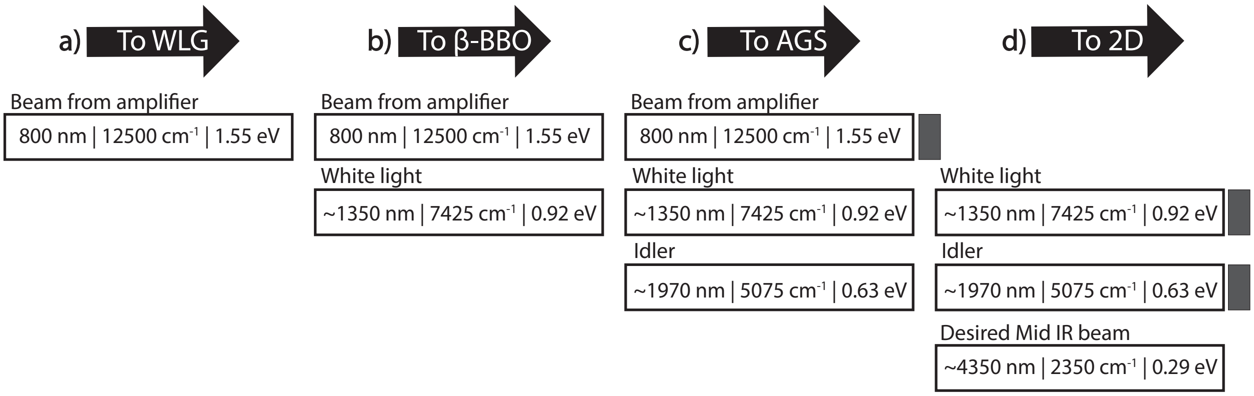

Figure 3.3: The optical parametric amplifier (OPA) generates mid-IR pulses through a series of optical transformations. a) The beam from the amplifier (∼800 nm) is directed onto a sapphire crystal, which generates white light. b) The white light and original ∼800 nm beams are directed into a BBO crystal, which performs optical parametric amplification. c) The selected frequency (from the white light continuum) and the idler beam are then directed to the AGS crystal. d) The beams then undergo difference frequency mixing in order to generate the ∼2350 cm^{-1} mid-IR pulses that will be directed into the 2D-spectrometer.

mid-IR frequency, and this beam is directed into the 2D-IR spectrometer. A full description of the polarization, filtering, and phase control processes that occur in the OPA has been reported elsewhere.[105]

Light entering the 2D-spectrometer is split into separate beam paths: pumps, probe, and reference. The pump beam is split using a beam splitter. The pumps are then spatially aligned but temporally separated using a Mach-Zender interferometer. This also controls the first delay time (t_1) by changing the travel distance of the second pump pulse. A portion of these pumps is sent to a single-channel detector, which records an interferogram of the pump-pump overlap that tracks the phase. The Mach-Zender also contains a separate series of mirrors translated only vertically on which a helium-neon (HeNe) laser is projected. The HeNe is also split into two beams, one of which is vertically polarized, and the other is directed through a $\lambda/4$ wave plate to generate circularly polarized light. The linear and circularly polarized light is split by a polarization cube onto two separate photodiodes. The interference between these beams is used to measure the displacement of the Mach-Zender interferometer.

The second delay time (t_2) is the delay between the second pump pulse and the probe beam, which is modulated using a translation stage. The translation stage utilized has a maximum t_2 of 250 ps, or a maximum travel distance of 7.5 cm.

For polarization controlled experiments, a $\lambda/2$ mid-IR waveplate and a wire grid polarizer are placed in the path of the pump pulses. The waveplate is set to $45°$, and the polarizer is automated to switch between parallel and perpendicular orientations.

The pumps and probe all spatially overlap at the sample holder, which is designed to accommodate the brass sample cells as described above. A reference beam is also directed through the sample a small distance away from the path of the pumps and probe.

The signal field is emitted along the path of the probe pulse. The signal, ω_3, is diffracted across a 150 l/mm grating onto a liquid N_2-cooled 2×32 channel mercury cadmium telluride detector. In this frequency window, the 32 pixels record a spread of 80 wavenumbers, for a resolution of 2.5 cm^{-1} per pixel. Signals are transmitted to a lab computer using a Femtosecond Pulse Acquisition System (Infrared Systems Development Corp.) and analyzed by MATLAB-based software (Mathworks).

The OPA and 2D-spectrometer are housed inside boxes that, when the lids are in place, form a sealed environment. A purge system has been installed to send dry nitrogen into the OPA, 2D-spectrometer, and the glove bag that encloses the few optics between the 2D box and the detector. This system is critical for CO_2 spectra, as the detectors would otherwise be overwhelmed with the absorbance of atmospheric CO_2.

3.3 Modular Global Fit Codebase

The data acquisition processes generate a structure format for the data that includes experimental details (*i.e.* t_2 time, scan number and count, experiment date and time) as well as the data, both the Fourier transformed frequency-frequency contour plot and the time-domain t_1 interferogram. The frequency-frequency contour plot is most often utilized for analysis purposes, such as CLS, described above (chapter 2).

Global fitting the output spectra has been, at times, a very laborious process. In order to fit the complex CO_2 spectra that resulted from polymers experiments, a new codebase was developed to create a modular, tailorable, user-friendly workflow for global fitting. Here, we will walk through both the end-user functions and the object oriented programming they are based on.

Object oriented programming, in this context, allows for the generation of objects called superclasses. Subsequent classes will then inherit all the functionality within the superclass. The class inheritance structure of the OO_spectrum codebase is depicted in figure 3.4. It is possible, such as with **aDArrayBnd**, for a class to inherit the functionality of multiple classes.

Global fitting, as a process, calculates a χ^2 value: the sum of the square error between the data and the simulated spectrum. In order to calculate a spectrum similar to the experimental data, information must be provided. Additionally, as the point is to allow the code to modulate the value of free parameters in an effort to reduce the χ^2 value, it is necessary to have the ability to designate these parameters as either fixed or free.

fitParam and its child class **fitParamBnd** are the commands that format input data into the structure expected by children classes. As the name may imply, the parameters are given a name, a value, and a flag that indicates how to treat them with respect to the fit: free or fixed. **fitParamBnd** adds inputs for upper and lower bounds on the starting value. This function collects and sorts input parameters into simple, accessible arrays, which assists with both organization and data visualization later on.

As discussed in chapter 2, there are additional process that occur in experimental spectra that are not a native function of the lineshape or correlation (jointly: the response function). These phenomenological additions are introduced to the simulation algorithms using the **additionalDynamics** command. This is most often used by its child class: **aDArrayBnd**. **additionalDynamics** uses inputs of name, function, and index to apply the *function* to the correct diagrams/molecular responses, as designated by the *indices*. **aDArrayBnd** allows for the creation of an array of additional dynamics, each with their own bounded inputs,

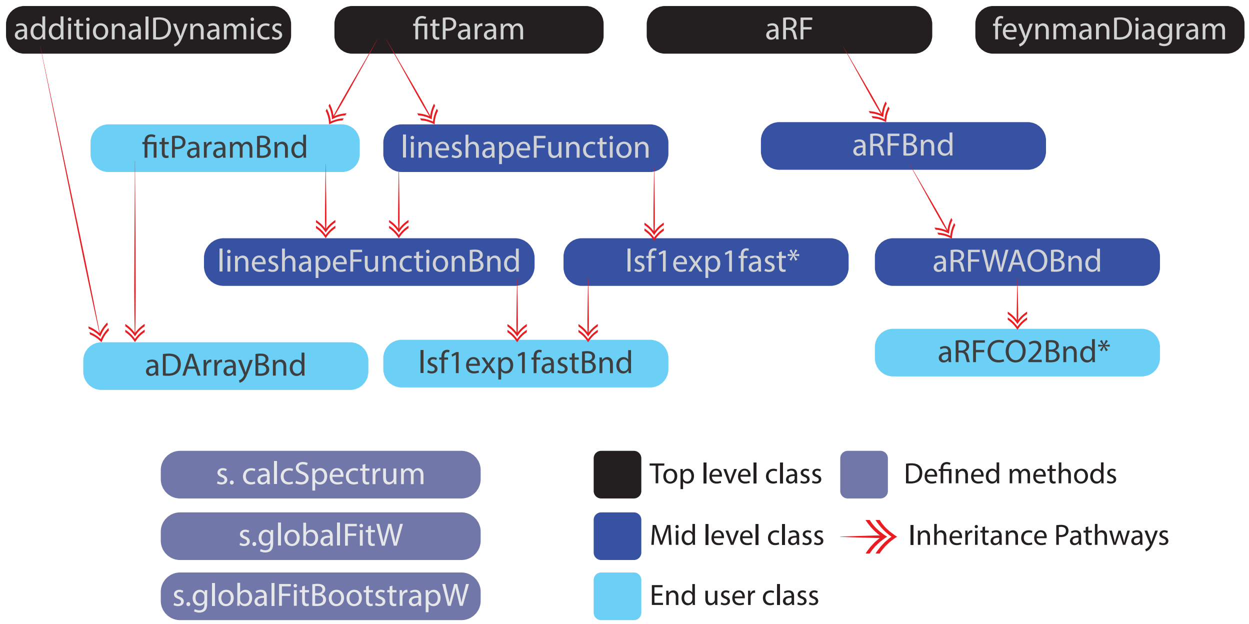

*several other lineshape function and analytical response function variations exist, including: **lsf1exp, lsf1expBnd, lsf2exp1fast, lsf2exp1fastBnd, lsfArrayBnd, aRFEANBnd, aRFTwoLevelSystem,** and **aRFTLSBnd**. For multiple related data sets, like temperature dvependence or polarization control experiments, **multiMeasurement** stores and organizes the individual aRF structure for each.

Figure 3.4: A class inheritance tree for the object oriented spectrum codebase used to simulate and globally fit 2D-IR spectra.

which can be flagged as either free or fixed, courtesy of its inheritance of **fitParamBnd**.

The shape and time-dependence of a given peak in a 2D-IR spectrum are governed by two important functions: the lineshape function (g) and the correlation function (c_2). **lineshapeFunction** is a derivative of **fitParam** that is designed to generate the g and c_2 functions that will be used in later stages of the calculations. A series of functions inherit the properties of **lineshapeFunction**, but here we will specifically discuss **lineshapeFunctionBnd**, which logically adds upper and lower bounds, and **lsf1exp1fast**. The functional forms of both g and c_2 are generated inside the **lsf1exp1fast** class, which then shares its properties with its bounded form, **lsf1exp1fastBnd**.

The outputs of both **lsf1exp1fastBnd** and **aDArrayBnd** are important inputs for the next family of classes: the analytical response functions. **aRF** is the superclass of this family and contains the methods for key steps like setting up axes, interpolating the calculated spectra, and calculating the residuals and χ^2 value. The method **s.calcSpectrum** is defined in **aRF**. **aRFBnd** inherits all of the functionality of **aRF** but also adds the constrained function minimalization (fmincon) functionality. Bootstrapping[106] is also defined in **aRFBnd**. Both **s.globalFitW** and **s.globalFitBootstrapW** are defined within **aRFBnd**. (The use of 's' here is shorthand and is the name of the structure containing all of the input variables.)

To adequately replicate a complex system using these analytical response functions, there are a number of valuable inputs that are not inherent to either **aRF** or **aRFBnd**. **aRFWAOBnd**, where WAO is a shorthand for "weakly anharmonic oscillator", initializes flags for the various types of Feynman diagrams and applies the additional dynamics, lineshape parameters, anharmonic shifts, and transition dipole moment scaling. This also includes the first instance of the **feynmanDiagram** class. **feynmanDiagram** calculates the response function for each diagram in the time domain and performs the appropriate Fourier transformations based on rephasing/non-rephasing flags.

The end-user version of the **aRF** class is unique to a chromophore and sometimes to an experiment. **aRFCO2Bnd** specifically contains inputs for the energy gap (dE_{cm}) between the main antisymmetric stretch band and the hot band shoulder, the temperature, and the frequency shift between the two bands. Additionally, the **aRFCO2Bnd** version includes and properly flags all 32 of the Feynman diagrams needed to replicate a CO_2 spectrum.

Several external data inputs are also required. A structure called *aRFOptions* is used to collect all of the input parameters, which can either be directly defined (such as the number of bootstrap repetitions or the frequency axes) or can utilize the **fitParamBnd** format to indicate the inputs as free or fixed fit parameters. Running the **s.calcSpectrum** command will generate a *simMatrix* which contains the spectrum as simulated with the input values. The *dataMatrix* and *weightMatrix* are added separately, where *dataMatrix* is experimental data formatted into a matrix of the shape $[\omega_3]$ x $[\omega_1]$ x $[t_2]$, and the *weightMatrix* has the same shape but includes weighting factors based on the number of scans included in the experiment for each time point to adjust for intensity variation.

Running **s.globalFit**, or any of its variants, **s.globalFitW**, **s.globalFitBootstrap**, or

s.globalFitBoostrapW, will perform the functional minimization (fmincon) fit, a weighted fit, a bootstrapped fit, or a weighted, bootstrapped fit, respectively. The best fit parameters (*s.pfit*) can then be fed back into **s.calcSpectrum** to simulate error-minimized spectara.

Below, table 3.1 summarizes the classes listed above, along with crucial methods defined within the class. Methods that are repeated in a child class typically include a new piece of information, such as a functional form.

There are additional classes that have been generated to handle different chromophores, different lineshapes, multiple measurements, or complex systems where several different lineshape functions are needed to fully replicate a spectrum. The flexibility of the analysis process makes this a powerful, useful tool for analyzing a wide range of 2D-IR spectra. This methodology is utilized to extract cross-peak kinetics in chapters 4 and 7.

Table 3.1: OO_Spectrum Classes and Methods

Class	Important Methods	Primary Function(s)
fitParam	-	Defines parameters of the fit, designates as free or fixed
additionalDynamics	-	Defines name, function, and indices for additional processes
fitParamBnd	-	Adds upper and lower bounds to parameters
aDArrayBnd	makeParamStruct	Organizes multiple sets of add.Dyn. into a bounded array
lineshapeFunction	makeG; makeC2; updateG	Defines functions to calculate g (lineshape function) and c_2 (correlation funtion)
lineshapeFunctionBnd	-	Adds upper and lower bounds to lineshape function parameters
lsf1exp1fast	makeG; makeC2	Defines functional forms of g and c_2
lsf1exp1fastBnd	-	Adds upper and lower bounds
aRF	calcSpectrum; makeParamStruct; setupTimeAxis; setupFreqAxis; err_fun; resample; residuals; addDiagrams	Defines steps to generate the simulated spectrum: axes initialization, setting time and frequency spacing, interpolation, error calculation, and residual calculations
aRFBnd	globalFit	Defines global fitting (fmincon) methods and adds checks for the presence of bounds
aRFWAOBnd	setupResponseFunction; calcResponseFunction; calcPhaseShift; calcAnhShift; calcTDM; calcAdditionalDynamics	Initializes labels for Feynman diagrams, calls feynmanDiagram to calculate response functions, applies additional dynamics, anharmonic shifts, and transition dipole moment
aRFCO2Bnd	calcBendShift; calcThermalPopulations	Adds simulation of the shoulder band and cross-peaks specific to CO_2, calculates peak shifts, identifies and indexes all 32 Feynman diagrams
feynmanDiagram	calcResponseTime; timeToFreqRephasing; timeToFreqNonRephasing	Calculates response of each indicated diagram in the time domain, performs Fourier transform based on rephasing or non-rephasing flags

4.0 Intramolecular Vibrational Relaxation of CO_2 in Ion Gels

4.1 Chapter Summary

Ultrafast two-dimensional infrared spectroscopy (2D-IR) and Fourier-transform infrared spectroscopy (FTIR) were used to measure carbon dioxide (CO_2) in 1-ethyl-3-methylimidazolium bis(trifluoromethylsulfonyl)imide ([emim][Tf_2N]), cross-linked low-molecular weight poly(ethylene glycol) diacrylate (PEGDA), and an ion gel composed of a 50 vol% blend of the two. The center frequency of the antisymmetric stretch, ν_3, of CO_2 shifts monotonically to lower wavenumbers with increasing polymer content, with the largest linewidth in the ion gel (6 cm^{-1}). Increasing polymer content slows both spectral diffusion and vibrational energy relaxation (VER) rates. An unexpected excited state absorbance peak appears in the 2D-IR of cross-linked PEGDA due to VER from the antisymmetric stretch into the bending mode, ν_2. Thirty-two response functions are necessary to describe the observed features in the 2D-IR spectra. Nonlinear least squares fitting extracts both spectral diffusion and VER rates. In the ion gel, CO_2 exhibits spectral diffusion dynamics that lie between that of the pure compounds. The kinetics of VER reflect both fast excitation and de-excitation of the bending mode, similar to the IL, and slow overall vibrational population relaxation, similar to the cross-linked polymer. The IL-like and polymer-like dynamics suggest that the CO_2 resides at the interface of the two components in the ion gel.

4.2 Introduction

Composite materials of ionic liquids and polymer membranes combine the selectivity of ionic liquids (ILs) with the advantages of membranes for potential next generation carbon capture technologies. Room temperature ionic liquids have emerged as potential alternatives to amine absorption systems of carbon capture.[3,107] This promise motivated the determination of both the performance limiting macroscopic properties (viscosity, thermodynamics of gas solubility, and gas transport) and investigation of the intermolecular interactions[108] that cause them.[52,53,109] Bulk ILs, however, have proved impractical for gas separations, largely because of their high viscosity.[3,42,44,74] While conventional membrane-based separations work under milder conditions, consume less energy, and occupy smaller footprints than bulk amine absorbers in general,[110] they have low CO_2 / N_2 selectivity and poor gas permeability. IL-polymer composite materials can side-step these limitations, and the encapsulated IL does not need to flow. The ILs beneficially plasticize the membrane, improve gas transport, and increase the solubility selectivity.

IL-polymer composites are diverse and include ion gels[60,61,84], supported ionic liquid membranes (SILMs)[86,87], and poly-ionic liquids (PILs).[73,111] These composite materials differ in the method of trapping the IL.

Ion gels are polymer films impregnated with IL. They are made by either swelling a polymer film or cross-linking a polymer in an IL-polymer mixture. Depending on miscibility, compatibility, and casting method, this process can produce a stable gel with trapped IL. Benefits of ion gels include the potential for both physical and chemical interaction between the polymer and the ionic liquid, along with commercial availability of the components. Supported ionic liquid membranes (SILMs) are porous polymer films that are filled with ionic liquid, which is held primarily by capillary forces.[43,72,112] This film construction limits carbon capture utility because large transmembrane pressures can evacuate the membrane.[74]

Poly-ionic liquids (PILs) include polymerized anions, cations, or both. PIL membranes[92] impregnated with “free IL” lie near the 2008 Robeson limit,[69] with high CO_2 permeability and relatively high CO_2/N_2 selectivity.[92] PIL membranes span a broad range of potential applications, from gas separations materials to solid electrolytes with the potential for triggerable changes.[113,114] Wide-spread implementation of PILs, however, may be limited by the film expense and complexity.[60]

To each of these composite materials, ILs add their unique properties, as ILs are structurally heterogeneous fluids. X-ray and neutron scattering experiments[115–117] supplemented by MD simulations[118–120] have established that ILs exhibit nano- or mesoscopic ordering. The charge-carrying moieties of the cations and anions aggregate and the non-polar alkyl-chains aggregate, generating structure on multiple characteristic length-scales. The characteristic length-scales can be described in a very general way by the types of structural features on that length-scale (from short to long): adjacency, charge-alternation, and polarity alternation.[121,122]

Structural heterogeneity influences the dynamics measured in ILs.[123,124] The dynamic timescales reflect both the varied microenvironments in the liquids, and the type of interaction between the molecular reporter and the IL.[125] Short time dynamics ($<$ 1 ns) in polar and non-polar domains can markedly be different.[126–129] The long-time dynamics ($>$ 1 ns) reported in many kinds of spectroscopic observables involve the reorganization of the polar and non-polar domains.[130–133] The vibrational modes of CO_2 can also serve as spectroscopic reporters of the local structure and dynamics around the CO_2. The relevant vibrational eigenstates of this system with their associated quantum numbers are the symmetric stretch, ν_1; the bend ν_2; the vibrational angular momentum, l; and the antisymmetric stretch, ν_3; denoted $|\nu_1\nu_2^l\nu_3\rangle$. The symmetric stretch and the vibrational angular momentum play no direct role in this discussion, so we suppress their labels, for example, $|0\,0^0\,0\rangle \equiv |\nu_2\nu_3\rangle = |0\,0\rangle$.

2D-IR spectroscopy provides spectroscopic observables that are tight constraints on models of liquid structure and dynamics. Because the vibrational frequency of a molecule is most influenced by its nearest neighbors, 2D-IR can report the structure and dynamics of a probe molecule in its first solvation shell. As the solvation shell fluctuates, the vibrational frequency changes as well. The random walk in vibrational frequency space is called spectral diffusion and causes a characteristic change in the shape of 2D-IR spectra. The reorientation of a molecule with respect to the laboratory frame causes a change in the amplitude of the 2D-IR signal, as does vibrational energy relaxation. Polarization-resolved experiments can separate the effects of lifetime and reorientation on the 2D-IR spectra, providing a 2D frequency-resolved map of orientational anisotropy[134], and can even separate the effects of structural reorganization and reorientation on the vibrational frequency fluctuations.[50,135] All of these observables can be modeled in molecular dynamics simulations. For the case of CO_2 in an archetypal IL, the 2D-IR experimental observables provide constraints on the modeling[17,35] and the modeling provides molecular explanations of the spectroscopy.[33,34,36,48]

In bulk ILs, this kind of experimentally-validated computational investigation has revealed the mechanism of selective CO_2 solvation.[36] The IL forms a solvation shell that complements the quadrupole of the CO_2 molecule. The electrostatic interactions account for almost all the enthalpy of solvation, and the additional structure of the solvation shell explains, at least qualitatively, the negative entropy of solvation. N_2, on the other hand, does not induce this restructuring in the liquid.[36]

The dynamics in ILs change in composite materials and at interfaces in complex ways. In some experiments, interfaces, including between ILs and substrates, ILs and surrounding liquids, and ILs in composite materials, can induce changes in IL dynamics and even average structure in the IL, which can extend to remarkably long time- and lengthscales. Reflectance IR and second harmonic generation (SHG) suggest reordering of ILs under sheer flow at mica interfaces extending over micrometer lengthscales.[136] 2D-IR of IL droplets in an oil bath suggest changes in the ultrafast dynamics over micrometer lengthscales, while 2D-IR of ILs in SILMs as a function of pore size suggest that the dynamics due to the interfaces change back to the bulk values on a few tens of nanometers lengthscales.[137] This area is still actively under investigation and suggests the kinds of complex changes in structure and dynamics that can occur by incorporating ILs into more complex environments and materials.[86,87,138]

Though most 2D-IR studies focus on vibrational frequency fluctuations, both vibrational energy relaxation (VER) and the frequency fluctuation dynamics reflect the stochastic coupling of the vibrational chromophore to its bath. Both effects can be written in terms of time correlation functions of the appropriate coupling elements. In this formalism, the Fourier transform of the time correlation function of the coupling between vibrational energy levels evaluated at the frequency of their energy difference is the rate of population relaxation between the two levels, k_{ij}.[139,140]

The spectral diffusion dynamics can be extracted directly from the shapes of 2D-IR spectra via:

$$c_2(t) = \langle \delta\omega(t)\delta\omega(0) \rangle \, . \tag{24}$$

Here, $c_2(t)$ is the two-point frequency fluctuation correlation function, $\delta\omega(t)$ is the instantaneous fluctuation of the frequency at time t, $\omega(t)$, from the average frequency, $\langle\omega\rangle$, (*i.e.*, $\delta\omega(t) = \omega(t) - \langle\omega\rangle$). In other words, the 2D-IR spectra report the dynamics of the system-bath coupling both in the frequency fluctuations and in the VER rate.

Because both VER and FFCFs depend on time correlations of the bath, both report the dynamics of the molecule in the fluctuating environment. There are, however, important differences in the characteristic motions that each process reports. The VER rate depends on high energy fluctuations (*i.e.*, ω_{ij} is typically an intramolecular vibration of several thousand wavenumbers). On the other hand, c_2 typically reports only low frequency modes (*i.e.*, the fastest timescales are typically on the order of 100 fs, corresponding to intermolecular modes on the order of < 300 cm^{-1}). This difference reflects the amount of energy exchanged with the bath, or equivalently, the density of modes (spectral density) at the relevant frequencies. In this formulation, both VER and frequency fluctuations report the stochastic dynamics of the surroundings of the spectroscopic chromophore.

VER of CO_2 in solution is often adequately described as a simple exponential loss of population in the vibrationally excited mode, occurring with a timescale T_1. The T_1 time for CO_2 in water is on the order of 10 ps.[141] In ionic liquids, vibrational relaxation rates of CO_2 are ~ 60 ps.[17,46,142] The focus of this work, however, is to characterize both inter- and intramolecular flow of energy after vibrational excitation.

Previous 2D-IR experiments in ionic liquids have observed the flow of energy into and out of the bending mode reported by the antisymmetric stretch. In the linear absorption experiment, CO_2 displays a "hot-band" located ~12 cm^{-1} lower than the ν_3 antisymmetric stretching mode. This hot-band results from the anharmonic coupling of the stretch and the bend, contrary to older literature.[143] The thermal population of the doubly degenerate state with one quantum of bend is roughly 7% at room temperature. Because the stretch and bend are coupled, the excitation of the bend causes the observed shift in the ν_3 mode. 2D-IR experiments demonstrated that equilibration occurs between the total ground state $i = |0\,0\rangle$ and the thermally-excited bend state, $j = |1\,0\rangle$.[17,46] Our investigation will build on this knowledge and expand the understanding of CO_2's VER in these complex materials.

Calculating VER from simulations remains less developed than calculating vibrational frequency trajectories and remains an open theoretical challenge. Explicit calculation of the full non-equilibrium nuclear wave-function dynamics is out of reach, so many approximate methods are being developed and tested. Dynamics on excited vibrational potentials have all the complexity as dynamics on excited electronic surfaces. High frequency ($\hbar\omega > k_B T$) modes are coupled both to a bath and to each other. As recently noted[144], even conical intersections – in this context between vibrational states – can play a role in efficiently bringing excited state population back to the vibrational ground state in at least some cases. At the same time, there are solid grounds to expect that the appropriate correction factors can rescale non-equilibrium classical dynamics to reproduce more complex quantum calculations.[145]

Semiclassical approaches offer alternative methods to calculate VER. For example, a linearized semiclassical method based on a local harmonic approximation (LHA-LSC) has been developed to calculate VER rates for a number of solutes, including CO_2.[146] Coherence transfer and the coupling of thermal fluctuation in low-frequency modes to high frequency modes were demonstrated using a semi-classical optimized mean trajectory method.[147,148] This approach was able to reproduce the experimentally observed cross-peaks in 2D-IR spectra that arise from the thermal excitation and de-excitation of the bending mode.[17] For CO_2 in an atomic liquid, VER rates derived from classical and semiclassical simulations differ by orders of magnitude. Classical simulations produced significantly slower rates, due to the large energy mismatch between the high-frequency vibration ($\sim$ 2500 cm^{-1}) and thermal energy ($k_B T \sim 200$ cm^{-1}, where k_B is the Boltzmann constant).[146] 2D-IR experiments contain information about VER processes, and extracting these rates offers a method of testing and validating the proposed simulation methodologies. These theoretical efforts reflect the importance of understanding VER as a fundamental step in many complex chemical processes.

Increasing knowledge about the utility of CO_2 as a probe of its local environment has prompted further exploration of its molecular scale interaction behavior. Understanding this interaction allows for more comprehensive modeling, prediction, and explanation of CO_2's behavior. As such, our strategy is to utilize CO_2 as a probe of local structure and dynamics in an ion-gel-type IL-polymer composite material, along with the corresponding parent materials. The polymer chosen was a low molecular weight cross-linked poly(ethylene glycol) diacrylate (cl-PEGDA) gel. This gel is one of many polymers of interest in carbon capture and separations applications owing largely to its very high CO_2-philicity.[149] The ionic liquid examined was 1-ethyl-3-methylimidazolium bis(trifluromethylsulfonyl)imide ([emim][Tf_2N]), an ionic liquid with previously established good solubility of, and affinity for, CO_2.[42,142]

This paper will focus largely on measuring and modeling the characteristic VER in these materials. The frequency fluctuation dynamics will be addressed in a subsequent publication.

In this work, we show linear (Section 4.4.1) and ultrafast two-dimensional infrared spectra (Section 4.4.2) of CO_2 in an ionic liquid, a cross-linked polymer gel, and an ion gel. We then develop a quantitative kinetic model to understand the origins of the unexpected features in the spectra, and describe the overall model for intramolecular vibrational relaxation of CO_2 (Section 4.4.3).

4.3 Methods

4.3.1 Materials

Bulk 1-ethyl-3-methylimidazolium bis(trifluoromethylsulfonyl)imide ([emim][Tf_2N]) was obtained from IoLiTec (figure 4.1a). Poly(ethylene glycol) diacrylate (PEGDA, M_n=700, figure 4.1b) and 2,2-Dimethoxy-2-phenylacetophenone (DMPA, photo-initiator) were obtained from Sigma-Aldrich. Bone dry CO_2 gas (99.8 % purity) was obtained from Matheson TRIGAS.

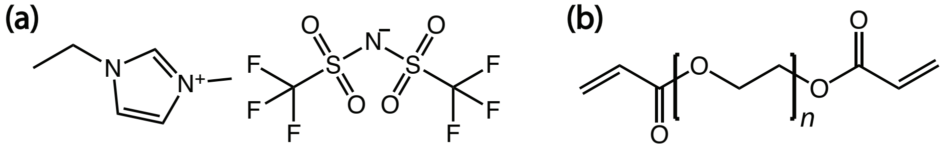

Figure 4.1: a) Ionic liquid 1-ethyl-3-methylimidazolium bis(trifluromethylsulfonyl)imide ([emim][Tf_2N]). b) Poly(ethylene glycol) diacrylate, M_n = 700 g/mol, $n \sim 14$.

4.3.2 Sample Preparation

Two distinct types of sample preparation were necessary. For measurements of a pure IL sample, the ionic liquid is vacuum dried prior to use, and a glove bag is utilized to control water contamination. CO_2 is loaded using a purpose-built vacuum sealed vial that enables mixing of the gaseous CO_2 and the IL. The sample is heated to ∼70 °C, and stirred while CO_2 is flowed into the vial for 10 minutes. Once loaded with CO_2, ~1 µL is placed between CaF_2 windows separated by a 25 µm polytetrafluroethylene (PTFE) spacer, secured into a brass sample cell and then immediately placed into the N_2-purged Fourier transform infrared (FTIR) spectrometer for measurement before transferring to the 2D-IR spectrometer.

For cross-linked samples, 1% by weight DMPA is added to the desired mixture of vacuum dried parent materials, and the sample is allowed to stir for a minimum of 3 hours. Precautions are taken to prevent a premature photo-initiation. After allowing sufficient time for mixing, in a glove bag 0.5-1.5 µL of the sample mixture is placed between two CaF_2 windows, pressed to the depth of the PTFE spacer by a hollow cylinder weight, and exposed to a 36 W UV lamp (MelodySusie) for ~2 minutes for cross-linking. To enable CO_2 loading, gels are made on drilled CaF_2 windows. To load CO_2, the custom, airtight flow cell assembly is placed into the N_2-purged FTIR spectrometer. Gas lines are attached to the cell, allowing a small pressure (< 10 kPa) of CO_2 to flow into the airtight cell and exhaust via exit tubing to atmosphere.

CO_2 uptake is monitored via the intensity of the dissolved CO_2 anti-symmetric stretch peak (~ 2340 cm^{-1}, figure 4.2). Polymer thickness was adjusted to obtain a saturated absorption of ~ 0.3 O.D. For the 50 vol%, a 25 µm spacer was used. For the pure cl-PEGDA gel, a 12 µm spacer was used in order to give similar CO_2 concentrations.

4.3.3 Spectroscopy

FTIR spectra are taken on a N_2-purged Thermo Fischer Nicolet FTIR spectrometer, taking 4-8 scans with 0.5 cm^{-1} resolution. 2D-IR spectra are collected utilizing a Ti:Sapphire chirped pulse amplifier laser system ($\lambda = 805$ nm, 5 kHz repetition rate, 120 fs pulse duration) (Coherent Vitesse/Coherent Legend Elite). The mid-IR pulses are generated using a home-built optical parametric amplifier (OPA), designed to suppress noise.[104] After the OPA, the spectral bandwidth is around ~200 cm^{-1}. The pulses are tuned to 4.3 µm, with ~2.2 µJ entering the 2D-IR spectrometer.

The 2D-IR spectrometer employs a pump-probe geometry.[150] A Mach-Zender interferometer controls the first delay time, and a translation stage controls the second. The signal field is emitted along the path of the probe pulse. The signal, ω_3, is diffracted across a 150 l/mm grating onto a liquid N_2-cooled 2×32 channel mercury cadmium telluride detector. Signals are transmitted to the lab computer using the Femto-second Pulse Acquisition Spectrometer (IR Associates), and all data is organized and analyzed using Matlab software (MathWorks).

4.3.4 Global Fit Analysis

The global fitting method used to analyze and simulate experimental 2D-IR spectra utilizes response functions generated from all relevant rephasing and non-rephasing Feynman diagrams (Supporting Information). Coupled kinetic equations account for transitions between population states during t_2, and the resulting phenomenological rates account for both inter- and intramolecular vibrational relaxation processes. Orientation dynamics are accounted for by an additional set of parameters applied to these simulated spectra. The simulated spectra are optimized using nonlinear least squares regression analysis to minimize errors. To normalize for variation in signal-to-noise ratio, the sum of square error is weighted by the number of experimental scans taken at each t_2 time. The number of scans range from 8 at early times to 120 at long times. Error bars on fitted parameters were estimated by bootstrapping[106] ($n_{\text{boot}} = 100$) to obtain 95% confidence intervals on all fitted values. In bootstrapping, the global fit is repeated using random data points drawn with replacement from the full data set. The errors are estimated based on the observed variation in fitting parameters. To compare the amplitude of peaks in the experimental data and simulated spectra, the total (sum) amplitude of a selected region was plotted as a function of time. Taking a sum allowed for accurate representation of the sign of the data and accounted for any competition behavior between peaks of opposing sign.

4.4 Results and Discussion

4.4.1 Linear IR Spectroscopy

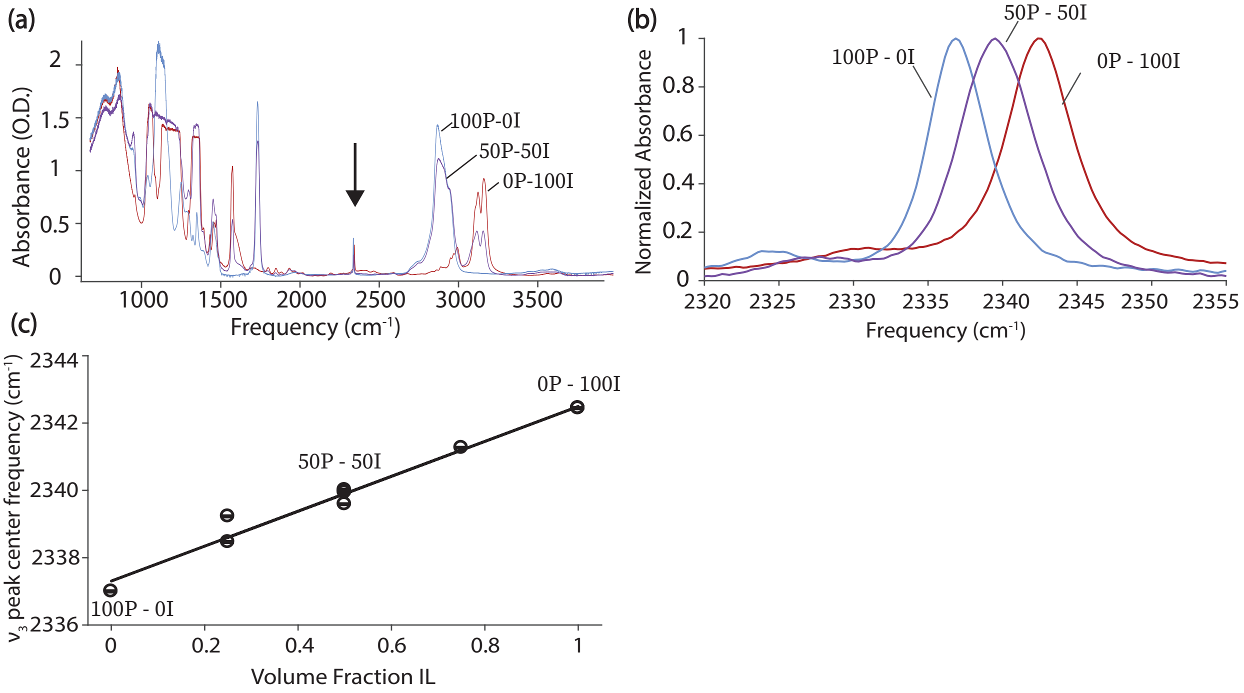

Figure 4.2: FTIR analysis identifies CO_2 as a strongly-absorbing, matrix-sensitive IR chromophore. a) The CO_2 peak sits in a spectrally clear region around 2340 cm^{-1} (arrow). b) The CO_2 peak shifts with changing volume percent ionic liquid. c) The CO_2 antisymmetric stretch (ν_3) peak for a series of blends are fit to a Voigt function to determine center frequency. Center frequency as a function of ionic liquid content results in a linear correlation of slope 5.2 cm^{-1} with an intercept of 2337 cm^{-1}. For each volume fraction, several mixtures were made and measured. Small compositional changes can result in differences in ν_3 frequency, especially the 0.25 and 0.50 IL fraction samples. For the 0 and 1 IL fraction samples the data markers overlap.

In these composite materials, CO_2 senses the ionic liquid-polymer composition. CO_2's ν_3 antisymmetric stretch vibration appears near 2340 cm^{-1}, a region in both the ionic liquid and cross-linked polymer samples that is largely free of other strong absorptions (figure 4.2a).

Varying the composition shifts the vibrational frequency by ~ 6 cm^{-1} between the pure IL (0P-100I) and cl-PEGDA (100P-0I). As the fraction of ionic liquid increases, the peak shifts linearly to higher frequency, ranging from 2337 cm^{-1} to 2342 cm^{-1} (figure 4.2b,c). The width of the ν_3 band is narrowest in the 100P-0I film (4.9 cm^{-1}), broadens in the 50P-50I film (6.0 cm^{-1}), and narrows again in the 0P-100I sample (5.4 cm^{-1}).

In addition to the main band, the shoulder (hot-band) is present. A fraction of CO_2 molecules, given by the Boltzmann factor, are thermally excited to the first excited state of the bending mode. These molecules absorb at lower frequency due to the anharmonic coupling of the antisymmetric stretch (ν_3) and the bend (ν_2). The hot-band is red-shifted by 12 cm^{-1} and has around 7% the intensity of the main antisymmetric stretch band (figure 4.2b).

Solvatochromic shifts of CO_2's ν_3 vibration are seen in a variety of samples.[17,46,86,143] Vibrational frequency decomposition[17,33] identified geometric distortion, electrostatics, and charge transfer as factors in the center frequency shift. In neat ionic liquids, geometrical distortion of CO_2 as a result of charge transfer from the anion explained the variation in vibrational frequency with anion identity. Due to the structural complexity of the mixed ionic liquid-polymer environment, similar computational studies for this system are beyond the scope of this work. Nevertheless, we can qualitatively address the influences on the vibrational frequency. A reasonable proxy for electrostatic interaction is the dielectric constant, values of which for the polymer and ionic liquids are very similar (~ 12).[151,152] This rules out electrostatics as a major contributor to the vibrational frequency shift in this system as well.

In a SILM, the CO_2 antisymmetric stretch mode split into two peaks, explained as CO_2 in two regions; the IL-filled pores and polyethersulfone (PES) polymer support. When scaled for the reduced-mass difference for the ν_3 mode in $^{12}CO_2$ and $^{13}CO_2$, the vibrational frequency is ~ 2340 cm^{-1} in the encapsulated IL ([emim][Tf$_2$N]) and ~ 2335 cm^{-1} in the PES.[86] (The ~ 3 cm^{-1} shift between the frequency reported in Ref.[86] and our reported value may be a result of the confinement in the polymer support, and another subtle indication of the surprisingly long range effect of IL encapsulation.) We do not see a splitting of the CO_2 peak in our work, implying a more homogeneous environment for all samples.

The remaining possible explanations are that the CO_2 interacts specifically with electron rich carbonyl groups of the PEGDA in a mechanism similar to the previous ionic liquids. Alternatively, the dense packing of the film may provide a sterically constrained environment like in long-chain alkanes, which also absorb in this region, *e.g.* hexadecane 2335.1 cm^{-1}.[143]

4.4.2 Experimental 2D-IR

2D-IR measurements in the composite materials also reflect the IL-polymer ratio. 2D-IR measurements for cl-PEGDA, 100P-0I; [emim][Tf_2N], 0P-100I; and the 50 vol% ion gel, 50P-50I; were taken for t_2 values ranging from 200 fs to 250 ps (figure 4.3a). All samples exhibited similar early time spectra including two diagonal peaks containing the stimulated emission (SE) and ground state bleach (GSB) of the antisymmetric stretch and the shoulder (regions I-II, figure 4.3b, blue). Also present are the two anharmonically shifted excited state absorption (ESA) peaks. For CO_2 the anharmonic shift is ~ 24 cm^{-1} (regions III-IV, figure 4.3b, red). As the t_2 waiting time is increased, the peak shape changes; peaks begin inhomogenously broadened and become more rounded. This change in shape is characteristic of spectral diffusion. A quantitative analysis of spectral diffusion in these samples will be the focus of future work.

The focus of this work is the dynamics of the cross-peaks and the inter- and intramolecular vibrational energy flow that they report (figure 4.3d). In general, cross-peaks appear off the diagonal and can result from mechanical or vibrational coupling, chemical exchange, and population or coherence transfer.[11] For CO_2, cross-peaks arise from reversible population transfer between the antisymmetric stretch and the shoulder, constrained by the temperature dependent equilibrium constant, K_{eq}. By 75 ps in all samples, the shoulder peaks (regions II and IV) have disappeared due to the downhill flow of energy from $|1\,0\rangle$ to $|0\,0\rangle$ (figure 4.3d, k_d).

At long t_2 times (> 75 ps), the CO_2 spectrum in cl-PEGDA (100P-0I) gains an additional, unexplained red peak in region V (figure 4.3a, arrow). A model of reversible energy exchange between the manifolds of states (between zero and one quantum of bend) predicts a pattern of two blue cross-peaks and two red cross-peaks. This unexpected red peak contradicts this

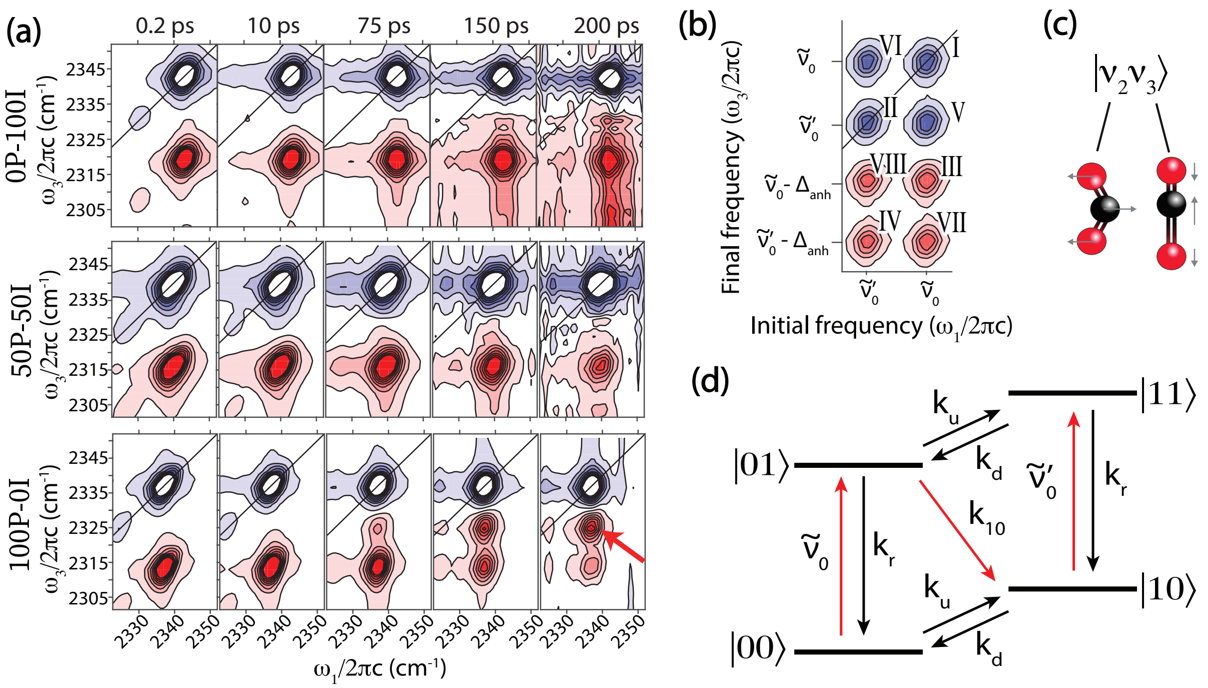

Figure 4.3: a) Experimental 2D-IR of CO_2 reveal an unexpected peak at long times (> 75 ps) in the 100P-0I sample (red arrow). To highlight smaller features, the fourteen contours are drawn at equally spaced intervals, centered around zero, beginning at half the most negative value. Full data sets are available in the supporting information. b) The third-order transitions of the antisymmetric stretch of CO_2 generate peaks in eight regions of the 2D-IR spectrum. c) Kets are labeled with bend and antisymmetric stretch quantum numbers. d) The energy-level diagram and kinetic rate constants. The red arrows, including the crossover pathway, k_{10} ($|0\,1\rangle$ to $|1\,0\rangle$) trace the pathway that generates the hot ground state.

model by appearing where a blue peak is predicted. In addition to having the opposite of the expected sign, this peak appears more slowly and eventually becomes more intense than the antisymmetric stretch's excited state absorption peak.

The unexpected red peak has the features of an excited state absorption from $|1\,0\rangle$. The red peak in region V reports an initial frequency that corresponds to the energy gap between

$|0\,0\rangle$ and $|0\,1\rangle$. During t_2 a population transfer occurs, and energy moves from $|0\,1\rangle$ to $|1\,0\rangle$. Its final frequency reports the energy gap between $|1\,0\rangle$ and $|1\,1\rangle$ (figure 4.3d, red arrows). This process of vibrational relaxation to a state other than the ground state is often referred to as a "hot ground state" (HGS). In this instance, some molecules initially with no quanta of bend relax not to the total ground state but to the bend excited state with one quantum of excitation.

In the condensed phase, a HGS is essentially any IR-excitation-induced photoproduct, and, as such, HGSs have been observed in many systems. This behavior has been most thoroughly explored in water and alcohols. The OH or OD stretch relaxes both directly to the ground state and indirectly through the bending mode.[153] Eventually, the energy pools in low frequency, intermolecular modes of the liquid which are anharmonically coupled to the OH/OD stretch and shift its vibrational frequency.[154–166] In a similar spirit, a HGS was used to probe dynamics in the protic ionic liquid ethylammonium nitrate (EAN).[167] Essentially the same effect has been used in other systems to track the intramolecular flow of vibrational energy through molecules, using specific functional groups as local thermometers.[168–170] In a few remarkable cases, infrared light can even drive a photoisomerization, such as the cis-trans isomerization of HONO.[171] Prior to our exploration, there has been no report of an HGS for CO_2.

Though the intermolecular flow of energy between the bath and CO_2's bending mode had been analyzed experimentally[17,142] and theoretically[147], this intramolecular vibrational energy flow had not been noted previously. Reversible exchange of thermal energy between $|0\,0\rangle$ and $|1\,0\rangle$ predicted a blue cross-peak in this position (figure 4.3d). The appearance of this peak implies a competition between the processes that formed the hot ground state and the blue cross-peak. In the 0P-100I and 50P-50I systems, there is no distinct peak in region V, implying a balance between the pathways (figure 4.3a). The same cancellation effect may also explain why the feature was not noted in ionic liquid experiments. Understanding this competition both qualitatively and quantitatively requires development of a comprehensive model that accounts for both IVR and spectral diffusion dynamics in CO_2, and is the aim of this work.

4.4.3 Modeling Population Transfer

To test our proposed origin for the hot ground state, we developed a detailed kinetic scheme for the states of the system that participated in population transfer during the waiting time, t_2. Spectral diffusion during t_2 obscured our efforts to extract population kinetics directly from integrating peak areas (data not shown), so we developed a quantitative model that is able to treat both spectral diffusion and population transfer on equal footings. The approach combines the kinetics of population transfer during t_2 with third-order response function formalism in the cumulant approximation.

To track the flow of energy into and out of each of the four participating population states of CO$_2$, we write a kinetic rate matrix, K,

$$K = \begin{array}{c} \\ |00\rangle\langle 00| \\ |01\rangle\langle 01| \\ |10\rangle\langle 10| \\ |11\rangle\langle 11| \end{array} \begin{array}{c} \begin{array}{cccc} |00\rangle\langle 00| & |01\rangle\langle 01| & |10\rangle\langle 10| & |11\rangle\langle 11| \end{array} \\ \begin{pmatrix} -k_u & k_r & k_d & 0 \\ 0 & -k_r - k_u - k_{10} & 0 & k_d \\ k_u & k_{10} & -k_d & k_r \\ 0 & k_u & 0 & -k_r - k_d \end{pmatrix} \end{array}. \qquad (25)$$

The matrix includes rate coefficients for the four important kinetic pathways (figure 4.3d). Rates k_u and k_d describe the previously defined thermal excitation and de-excitation pathways. The vertical relaxation rate, k_r, represents the direct relaxation from an excited state into the corresponding ground state. The crossover rate, k_{10}, describes the relaxation of energy from $|0\,1\rangle$ to $|1\,0\rangle$, crossing between manifolds. Diagonalizing K provides the time dependence of population beginning in each vibrational state. The time-dependent kinetic equations combined with a time-dependent response function formalism generates a model capable of accurately replicating all of the features visible in the experimental data.

There are 32 double-sided Feynman diagrams needed to describe the diagonal peaks, the cross-peaks due to thermal equilibration of the bending mode, and intramolecular vibrational energy relaxation (figure 4.4).

Four diagonal peaks result from six rephasing diagrams (figure 4.4a,b) and six non-rephasing diagrams (Supporting Information). Pathways starting in the total vibrational ground state include SE and GSB (peak 1a), and ESA (peak 2a), and the same holds for the pathways starting with one quantum of bend excitation (peaks 1b, 2b respectively). The sign of each diagram is governed by the number of interactions from the right.

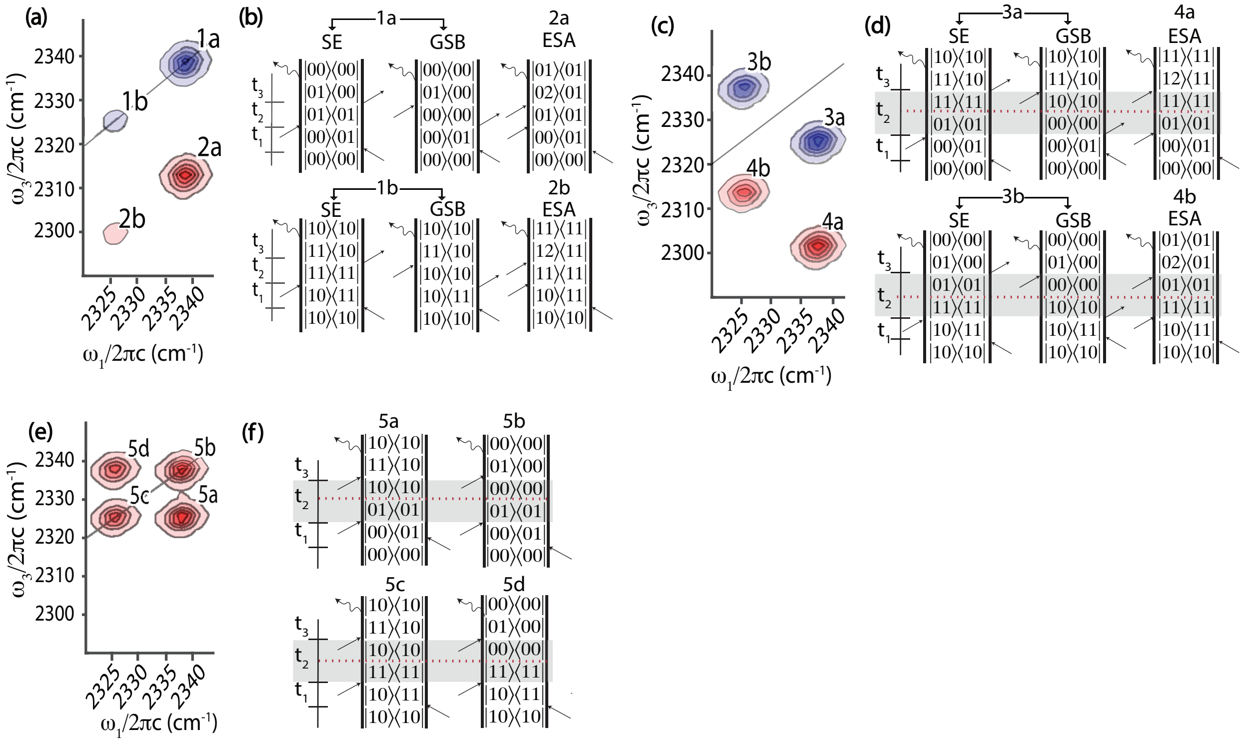

Figure 4.4: The 16 rephasing diagrams used to model the 2D-IR spectra. a,b) The four diagonal peaks, two from the pure antisymmetric stretch and two from the shoulder, are generated by six rephasing Feynman diagram pathways. c,d) Cross-peaks appear due to the thermal excitation and de-excitation of the bending mode during t_2 (red dashed line). e,f) Vibrational relaxation generates four peaks which overlap peaks 1a,b and 3a,b.

Thermal excitation and de-excitation of the bend during t_2 cause four cross-peaks, 3a/b and 4a/b, to appear (figure 4.4c,d). Peaks 3a and 4a result from an upward exchange between $|0\,0\rangle$ and $|1\,0\rangle$ governed by the up rate (figure 4.3d, k_u). Peaks 3b and 4b result from the opposite process, exchanging downward, governed by the down rate (figure 4.3d, k_d). Interaction with the bath causes molecules to either gain or lose one quantum of bend, moving up or down between the two manifolds of vibrational states.

In this perturbative treatment, total vibrational relaxation causes the signal to disappear through a cancellation of terms. Without the cancellation there would be persistent blue peaks at very long times. All blue peaks are composed of SE and GSB pathways. The SE contributions scale with the population in the first excited state, $|0\,1\rangle$, whereas GSB contributions scale with ground state population, $|0\,0\rangle$. While population in the $|0\,1\rangle$ state decreases consistently with time, population in the $|0\,0\rangle$ vibrational ground state decreases initially due to thermal equilibration with $|1\,0\rangle$, but otherwise remains constant. Because the peak in region V results from the competition between two pathways, it was necessary to fully describe the related VER pathways. Four additional diagrams are needed to describe VER (figure 4.4e,f). During t_2, energy initially deposited into the antisymmetric stretch by the laser can relax either into the bath or into a combination of the bath and other intramolecular modes. Peaks 5b and 5c reflect relaxation of energy from the antisymmetric stretching mode, leaving the number of bend quanta unchanged (none for peak 5b or one for peak 5c). Peak 5a results from population transfer between $|0\,1\rangle$ and $|1\,0\rangle$. This formally two-quantum transition is a thermal process, and optical selection rules do not govern it. This peak falls in the same location and with the same sign as the unexpected peak in the cl-PEGDA spectrum (figure 4.3a, red arrow) and follows the above described pathway (figure 4.3d, red arrows). Peak 5d results from energy flow from $|1\,1\rangle$ to the total vibrational ground state $|0\,0\rangle$. While this transition does not have a direct kinetic pathway in our model, there are a number of routes that energy could take during t_2 to form this peak (*e.g.* $|1\,1\rangle$ to $|0\,1\rangle$ via k_d and then $|0\,1\rangle$ to $|0\,0\rangle$ via k_r). These diagrams generate the four red absorption peaks that, in the long-time limit, exactly cancel the four blue ground state bleach peaks, resulting in no net 2D-IR signal.

Determining a representative lineshape function allows for accurate representation of the change in peak shape over time. In this work, we assume a two-point frequency correlation function, c_2, with a delta-function representing motions in the motional narrowing limit and an exponential for motions in the spectral diffusion regime,

$$c_2(t_2) = \frac{\delta(t_2)}{T_2} + \Delta^2 e^{-t_2/\tau}, \tag{26}$$

with fitted results for T_2, Δ, and τ. The solvent reorganization timescales decreased with increasing IL content – agreeing with previous assertions that the peak shape appeared to change more slowly in polymer-containing samples.[86] T_2 is the dephasing time and is inversely representative of motions too fast to be captured with our experiments. T_2 decreases with increasing IL content, indicating more fast motions in the ionic liquid samples. The Δ values are a measure of frequency space sampled. In this sample set, Δ has an unexpected increase in the 50P-50I sample.

This increase in linewidth for the 50P-50I sample is also reflected in the linear spectrum (figure 2b). It is possible that this broadening results from the the complex environment of the composite sample. Likely, this mixed-matrix sample offers a qualitatively large number of conformations and local solvation environments for CO_2 given the presence of both IL-like, polymer-like, and interfacial regions.

Our model contains several assumptions. To reduce the number of free parameters, we assume that the rate of excitation and de-excitation of the bend is the same for the ground and excited states of the antisymmetric stretch. In other words, we assume a single set of k_u and k_d suffices because the difference between $\tilde{\nu}_0$ and $\tilde{\nu}_0'$ (figure 4.3d) is negligible. We also neglect potential splitting of the doubly-degenerate bending mode. In a related film, poly(methyl methacrylate), the splitting was observed to be ~ 8 cm^{-1},[172] which is negligible for our purposes.

We also employed several assumptions regarding the spectral diffusion dynamics of CO_2 which are justified based on prior work in ionic liquids. To model the lineshape, we truncate the cumulant expansion at the second order, which was shown to be a reasonable approximation.[35] We also only account for population transfer dynamics during t_2, not during t_1 or t_3, as the shoulder is well resolved and there is no coalesence of the shoulder and main band.[17] In calculating our spectra, we again employ the Condon approximation, assuming the transition dipole moment is constant with vibrational frequency.[33] Finally, we decouple rotations and frequency fluctuations. As such, the reported spectral diffusion dynamics include both reorientation-induced spectral diffusion (RISD) and structural spectral diffusion (SSD) components.[46,50]

Modeling that includes an appropriate lineshape function and accounts for population transfer kinetics reproduces the experimental data well (figure 4.5). The simulated spectra at early times include both the main diagonal antisymmetric stretch peaks and the shoulder bands with appropriate intensities (Regions I-IV). As time progresses, the cross-peaks begin

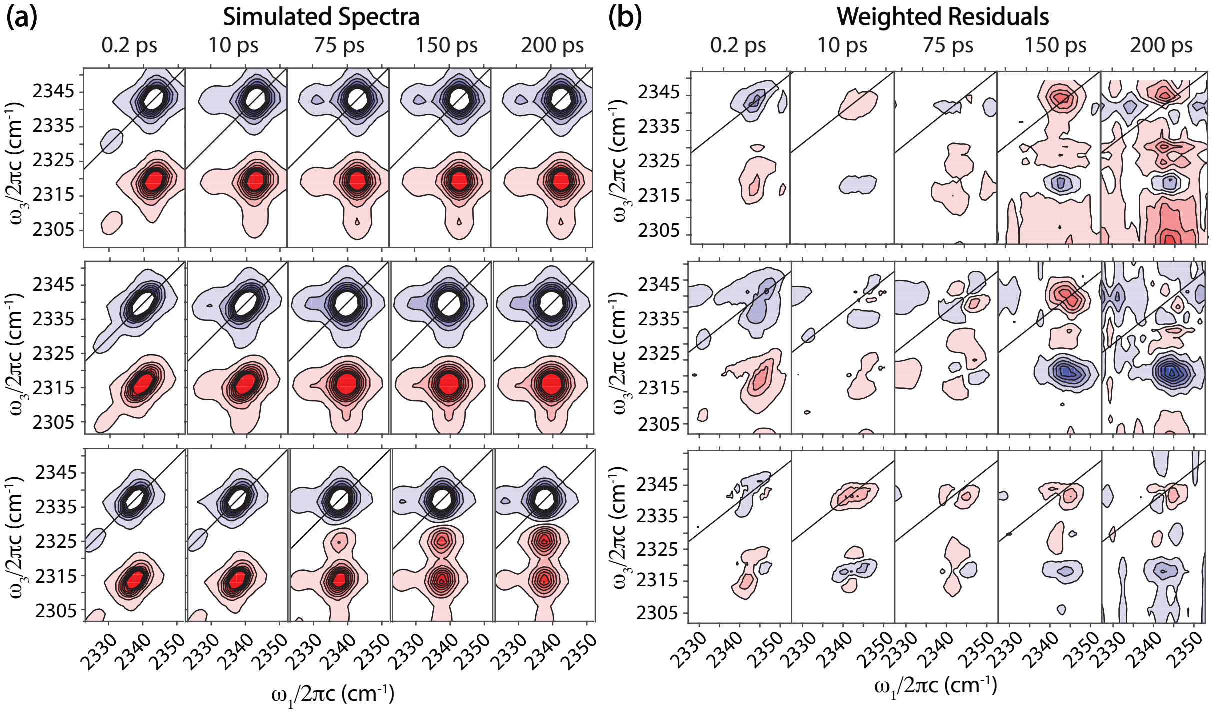

Figure 4.5: Kinetics-adapted response functions accurately reproduce the experimental spectra. a) The simulated spectra are shown at the same t_2 times as the experimental data, and with the same contour lines. b) Residual intensities are plotted on the same scale as the simulated spectra and experimental data.

to appear on reasonable timescales (Regions VI-VIII). In region V, the blue cross-peak does not appear in any of the systems with the same intensity as its counterpart in region VI, as observed in the experiment. In the 100P-0I sample, the model reflects the hot ground state peak in region V. In addition to the appropriate appearance and disappearance of peaks in the spectra, the observed spectral diffusion is reproduced.

In general, the agreement between simulated and experimental spectra is good, as the maximum intensity of appropriately weighted residuals are only around 3% of the experimental spectra for all samples. In the 50P-50I sample, the ESA decays systematically faster than in the simulated spectra. Several alternative kinetic models were explored to replicate this observation. The loss of intensity is not due to the k_{10} pathway being reversible. We suspect that an IR-dark state is present in the system that provides an additional relaxation pathway and causes the intensity loss and is not reflected by our model. In addition to the degenerate bend (ν_2) and antisymmetric stretch (ν_3) CO_2 has a symmetric stretch (ν_1) that occurs at $\sim$ 1300 cm^{-1} but is IR-dark and would not be visible in a 2D-IR investigation. IR-pump – Raman-probe experiments, which have been demonstrated[153], might be able to quantify this process. Nevertheless, the kinetic analysis was not sensitive to this small systematic error.

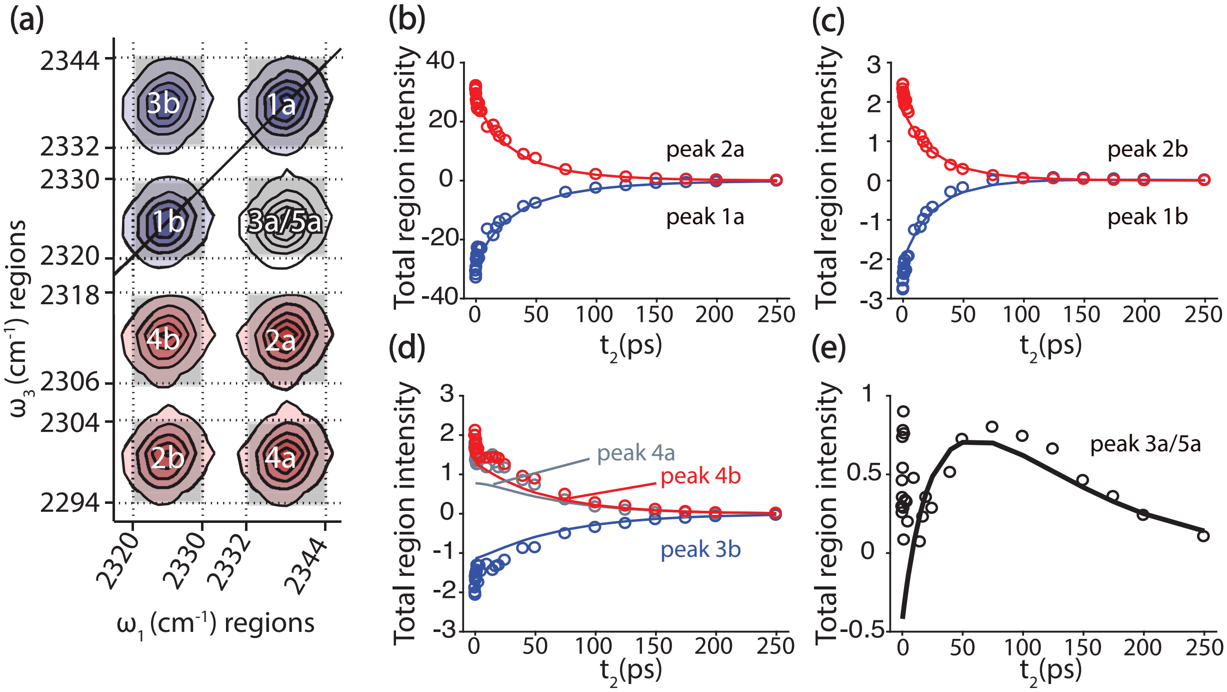

Figure 4.6: For the 100P-0I sample, there is good agreement between the simulated spectra and the experimental data. a) A schematic indication of the the eight regions of interest quantified in the simulated and experimental spectra. Region V, peaks 3a and 5a, can have either positive or negative sign depending on the competition of the opposing signals. b, c, d) The model (lines) and experiment (circles) agree very well for both diagonal (b,c) and cross-peaks (d). e) The fit reproduces the positive amplitude observed in the experiment because peak 5a outcompetes peak 3a.

To extract a measure of peak kinetics that could be compared to the simulated spectra, we selected each of the eight peak regions and extracted a total intensity from each spectrum (figure 4.6a). Intensities of the antisymmetric stretch (1a/2a) and the shoulder (1b/2b) diagonal peaks match (figure 4.6b,c). The cross-peaks, which are more strongly impacted by peak overlap (3a/4b) and the available experimental frequency window (4a) and the presence of noise in the system, still show good agreement (figure 4.6d). Region V shows variation at early times in the experimental amplitudes due to subtle differences between the experimental and simulated lineshape of the main bands (1a/2a). Once spectral diffusion begins, the simulated spectra accurately track the experimental kinetics in region V (figure 4.6d). The results of this analysis for the 0P-100I and 50P-50I samples are shown in the supporting information.

Spectral diffusion times increase with polymer content (table 4.1). The time constant, τ; and the dephasing time, T_2; both increase as polymer content increases. As the fraction of polymer increases, the dynamics reported by CO_2 slow.

The dephasing times in 100P-0I and 50P-50I samples are similar (~ 4.4 ps) and somewhat larger than in the pure ionic liquid (3.1 ps). The Δ value for the 50P-50I sample was significantly larger than the other two samples, implying a greater variety of local environments are explored. These spectral diffusion dynamics as a function of polymer content will be the focus of a future paper.

Table 4.1: Lineshape Function Best Fit Parameters

Sample	T_2	Δ (cm^{-1})	τ (ps)
100P-0I	4.5 ± 0.05	1.84 ± 0.02	82 ± 11
50P-50I	4.3 ± 0.07	2.3 ± 0.02	38 ± 4
0P-100I	3.1 ± 0.06	1.62 ± 0.05	16 ± 3

Quantitative values for each of the identified kinetic rates can be extracted from the fits (table 4.2). The rates k_u, k_{10} and k_r are free parameters of the fit, and k_d was calculated using

$$K_{eq} = \frac{k_d}{k_u}, \tag{27}$$

where $K_{eq} = \exp(-\Delta E_{10-00}/k_B T)$ fixes the relationship between k_u and k_d, and the energy gap between the ground state and the bend first excited state, ΔE_{10-00}, is 667 cm^{-1}. For the 0P-100I sample, the indirect relaxation from antisymmetric excited state, $|0\,1\rangle$, through bending manifold, $|1\,0\rangle$, to the ground state, $|0\,0\rangle$, is fast enough that our model was unable to determine a separate rate for the direct relaxation process $|0\,1\rangle \rightarrow |0\,0\rangle$, given by k_r.

The timescales reported for the equilibrium up- and down processes of the pure IL agree with literature values. The values extracted from our sample were $\tau_u = 1/k_u = 94$ ps and $\tau_d = 1/k_d = 7.4$ ps. Giammanco *et al.*[142] reported values for [emim][Tf_2N] of $\tau_u = 140$ ps and $\tau_d = 13$ ps.[142] In a similar ionic liquid ([bmim][Tf_2N]), Brinzer *et al.*[173] obtained values of $\tau_u = 400$ ps and $\tau_d = 33$ ps. The rates are slower, possibly as a function of the higher viscosity.

Table 4.2: Kinetics Best Fit Parameters

Sample	$\mathbf{k_u}$ **(ns^{-1})**	$\tau_\mathbf{u}$ **(ps)**	$\mathbf{k_d}$ **(ns^{-1})**	$\tau_\mathbf{d}$ **(ps)**
100P-0I	1.2 ± 0.1	850 ± 50	14 ± 1	71 ± 4
50P-50I	18 ± 1	50 ± 4	230 ± 20	4.3 ± 0.3
0P-100I	11 ± 1	90 ± 9	130 ± 10	7 ± 1

Sample	$\mathbf{k_{10}}$ **(ns^{-1})**	$\tau_\mathbf{10}$ **(ps)**	$\mathbf{k_r}$ **(ns^{-1})**	$\tau_\mathbf{r}$ **(ps)**
100P-0I	6.2 ± 0.4	160 ± 10	14.5 ± 0.4	69 ± 2
50P-50I	13 ± 2	80 ± 10	7 ± 2	144 ± 50
0P-100I	22.2 ± 0.3	45 ± 1	-	-

We expected that the prominent ESA in Region V of the 100P-0I sample would indicate crossover between manifolds faster than the other samples. Fitting results depicted the opposite trend. The τ_{10} crossover rate in the 100P-0I sample is slower than the 50P-50P and 0P-100I samples by factors of 2 and 4, respectively. The τ_{10} crossover rate is also around two times slower than τ_d or the direct relaxation rate, τ_r, in the 100P-0I sample.

Vibrational relaxation rates depend on the density of accepting modes at the appropriate energy difference. Others have recognized that the FTIR absorption spectrum can sometimes serve as a reasonable proxy for the total density of states.[174,175] We examined the FTIR spectra of each sample at the frequency that corresponded to the energy gap between manifolds, ω_{cross}. In this system, the difference between $|0\,1\rangle$ and $|1\,0\rangle$ is $\sim$ 1670 cm^{-1}. This frequency lies in the region between the strong absorptions of the PEGDA carbonyls (1700 cm^{-1}) and the Tf_2N sulfonyls ($\sim$ 1550 cm^{-1}). Assuming that the frequency of the bending mode is a constant, 667 cm^{-1}, in all samples, the amount of energy the bath must accept varies between samples because the center frequency the antisymmetric stretch shifts with composition (figure 4.7a).

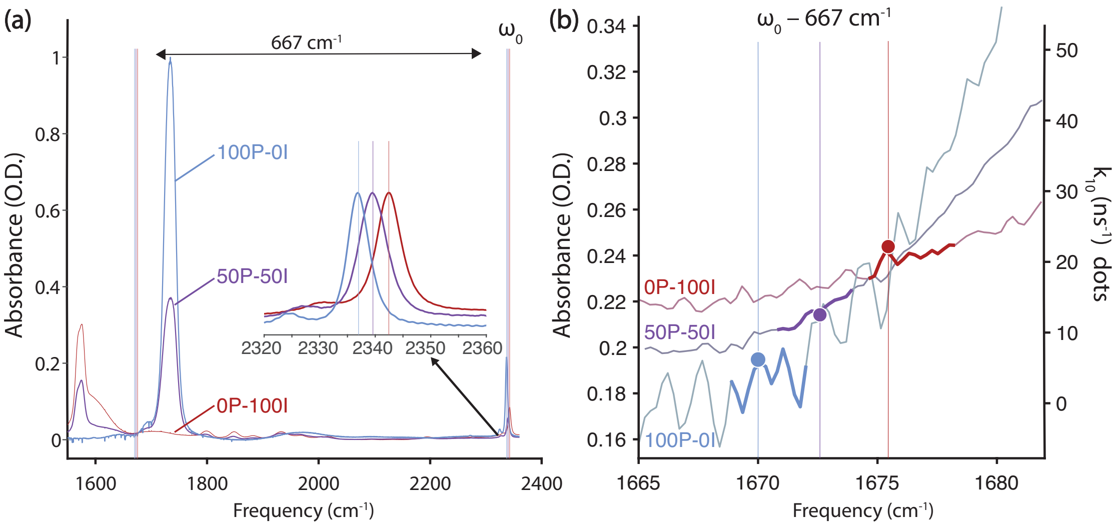

Figure 4.7: a) The energy gap between $|0\,1\rangle$ and $|1\,0\rangle$, $\omega_{\text{cross}} = \omega_0 - 667$ cm^{-1}, varies with IL vol%. b) k_{10} values (dots) scale relative to the background absorbance at the frequency corresponding to this energy gap. The left y-axis describes FTIR absorbance (lines), and the right y-axis describes the crossover rate (dots). Vertical lines indicate the gap frequency determined from panel (a). The FTIR of the 100P-0I contains small, sharp absorption lines that could not be removed by atmospheric correction.

At the ω_{cross} frequencies, there are no distinct peaks, but there are differences in background absorbance. The 100P-0I sample, which had the lowest ω_{cross}, also had the lowest background absorbance and the lowest k_{10} value. The k_{10} coefficients for the 50P-50I and 0P-100I samples scaled with the background absorbance at their relative ω_{cross} values (figure 4.7b). The k_{10} term reflects the capacity of the matrix to accept the energy lost in this crossover transition.

In addition to k_{10} being slow, all of the kinetic rates in the 100P-0I sample are slower than in the other samples. The largest difference is the characteristic equilibration time for the bending mode. These dynamics are constrained by the amplitudes of the peaks in regions VI and VIII. (Region VII is at the edge of the recorded spectral window in ω_3 and Region V contains signals from competing Liouville-space pathways 3a and 5a.) Chemical kinetics between two states characterized by a forward and backward rate, k_f and k_b, have a characteristic equilibration time given by the decay of the population correlation function $k_c = k_f + k_b$, or $1/t_c = 1/t_f + 1/t_b$. Unlike the case of the k_{10} values, this characteristic equilibration time does not vary monotonically with composition. Approximating the total ground state and the first bend excited state as a two-level system, the correlation time in the 100P-0I sample is 65.7 ps which is an order of magnitude slower than in the other samples. The fastest exchange between manifolds occurs in the 50P-50I ion gel system (4 ps) which is still two times faster than the 0P-100I sample (7 ps).

A density of states explanation such as the one above for the crossover rate, k_{10}, may also explain the rapid equilibration behavior. Due to the strong absorptions of the CaF_2 windows in addition to the the sample, however, we cannot measure the vibrational density of states at the bending mode frequency ($\sim 667\ \mathrm{cm}^{-1}$) in the current experiment. 2D-IR in an attenuated total reflection (ATR) configuration[176] might be able to access this information. Lacking this information, we cannot determine if the difference in bending mode excitation and de-excitation is due to differences in the vibrational density of states or the magnitude of the system-bath coupling.

The apparent amplitude and sign of the peak in Region V depend on a subtle balance of kinetic terms. Both peak 3a (blue) and peak 5a (red) result from population in $|1\,0\rangle$ at the end of t_2. Peak 3a is a ground state bleach/stimulated emission peak and peak 5a is an excited state absorption peak. These pathways have opposite signs and can cancel. The GSB and SE diagrams must accept energy from the bath while the ESA terms must lose energy to the bath in order to transition between the two manifolds of states. Diagonalizing the kinetic matrix (Eq. 25) extracted equations for the time-dependent population of each of the four energy states that participated in population transfer during t_2. To represent the overall sign of the relevant double-sided Feynman diagrams, we assign the k_{10} pathway a positive sign, and the k_u pathways a negative sign (figure 4.3d). To represent the overall sign of the relevant double-sided Feynman diagrams, we assign the k_{10} pathway ($|0\,1\rangle \xrightarrow{k_{10}} |1\,0\rangle$) a positive sign, and the k_u pathway ($|00\rangle \xrightarrow{k_u} |1\,0\rangle$) and $|0\,1\rangle \xrightarrow{k_u} |1\,1\rangle$) a negative sign.

The sum of the population growth curves for these pathways reproduces the shape of the experimental amplitude in region V (figure 4.8a-c). With the exception of very early times, where peak overlap from 1a/2a influences the region, both the 100P-0I and 0P-100I samples show good agreement between the experimental data and the predicted signal. For the 50P-50P sample, the experimental signal appears to have a slightly more positive signal than is predicted by the kinetic equations. Given the small amplitude of the transients, the relatively large Δ value for this sample (table 4.1), and the noise due to systematic fluctuations in the lineshape, it is likely that the total signal intensity in this region is affected by sources that are outside the scope of the kinetic predictions. Notably, however, both the 0P-100I and 50P-50I total region V intensities are smaller than the 100P-0I sample, as observed in the experiment.

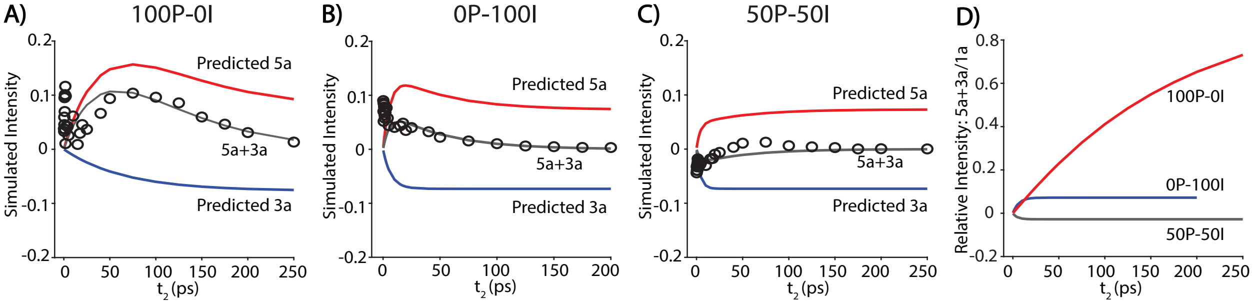

Figure 4.8: The relative appearance of the region V peak depends on the competition between the blue cross-peak (3a) and the red HGS peak (5a). a-c) show the population growth of the $|10\rangle$ state via the k_u pathway (Predicted 3a), and the k_{10} pathway (Predicted 5a), along with the combination of the two (grey) overlaid with a normalized experimental trace of spectral region V (points). d) Normalizing the predicted total population as a function of time (5a + 3a) by the population of the ground state exemplifies the differences between samples.

How prominent the peak in Region V appears depends on the amplitude of the peak relative to the amplitude of the peaks around it. Because the main bands are all decaying more quickly (figure 4.6), the apparent or relative signal in Region V grows. To demonstrate this effect, we normalize the predicted population in Region V by the predicted population of the ground state, Region I (figure 4.8d). The relative amplitude reproduces the prominence of the red peak in Region V for the 100P-0I sample, and the very small features in the other samples. For the 100P-0I sample, there is an increasingly positive signal in region V relative to the main bands. The 50P-50I sample has a small negative signal in this region, and the 0P-100I sample has a small positive signal, but both stay very close to zero. This implies that in both the 0P-100I and 50P-50I systems, net upward exchange ($|0\,0\rangle \rightarrow |1\,0\rangle$) is very similar to the flux downward exchange ($|0\,1\rangle \rightarrow |1\,0\rangle$) of energy between the manifolds. Imbalance in these pathways, such as in the 100P-0I sample, causes the prominent hot ground state peak.

These results suggest a physical picture. The overall structural reorganization timescale in the 50P-50I sample falls between its parent compounds, but the intramolecular kinetics are more similar to the ionic liquid. This implies that CO_2's environment contains influences of both the ionic liquid and the polymer components. In other interfacial systems, reverse micelles[177–180] and planar interfaces[176,181,182], the dynamics are different from the bulk usually within one or two solvation shells from the interface. CO_2 is known to have both a quadrupolar solvation[48] in ionic liquids, and is highly soluble in imidazolium-based ILs.[42] The room-temperature volumetric solubility, a function of the enthalpy of solution, for CO_2 in [emim][Tf_2N] is $\sim$ 2.4 $cm^3 cm^{-3} atm^{-1}$.[44] For CO_2 in cross-linked PEGDA, this value is around $\sim$1.6 $cm^3 cm^{-3} atm^{-1}$.[183] Given similarities between the intramolecular kinetics of the 50P-50I sample and the 0P-100I sample, and the slightly higher solubility of CO_2 in the ionic liquid, CO_2 in the ion gel sample likely localizes in a mostly-ionic liquid region that is near the polymer interface.

4.5 Conclusion

We utilized FTIR and 2D-IR to investigate CO_2 in a PEGDA-[emim][Tf_2N] ion gel and each parent compound. The vibrational frequency of the antisymmetric stretch, ν_3, of CO_2 is sensitive to the composition of its environment, shifting as much as 6 cm^{-1} between the pure ionic liquid and the pure polymer. The antisymmetric stretch absorption in the 50P-50I sample is a single broad band. Rather than segregation into separate ionic liquid and polymer environments, the CO_2 likely resides near the interface of the polymer and the IL.

2D-IR experiments revealed an unexpected hot ground state in the 100P-0I sample due to intramolecular vibrational relaxation from the antisymmetric stretch into the bend. A set of 32 Liouville-space pathways describes intra- and intermolecular vibrational relaxation including thermal equilibration of the bending mode. Experimental spectra are fit to response functions that include both dynamics due to spectral diffusion and population transfer during t_2. The dephasing time (T_2) and solvent reorganization time (τ) both increase with polymer content. The Δ values for both of the pure compounds are similar, but the 50P-50I sample has a larger spread of frequencies. In an upcoming publication, we will examine the dynamics of a PEGDA-IL ion gel and the parent compounds in further detail.

VER in the pure cl-PEGDA sample occurs more slowly than in the other two. The rate of crossover from $|0\,1\rangle$ and $|1\,0\rangle$, τ_{10}, scales with background absorption at a frequency of ω_{cross}, the gap between the two states, suggesting that a difference in the vibrational density of states at the appropriate energy difference is the controlling factor. For the pure ionic liquid sample (0P-100I), the kinetics of exchange between the $|0\,0\rangle$ and $|1\,0\rangle$ states agree with literature values. The 50P-50I sample has faster between-manifolds kinetic exchange but slower total vibrational relaxation than the pure IL.

Competition between k_u, which generates a blue peak, 3a, and k_{10}, which generates a red peak, 5a, explains trends in the appearance of the hot ground state seen in the experimental data. The increased rate of exchange between manifolds in both the 0P-100I and 50P-50I samples causes approximately equal intensities of peaks 3a and 5a, leading to no observed peak in this region. This effect may explain why peak intensities in this region have been small when measured in other measurements of CO_2 in ionic liquids.[17,142]

The molecular-level environment CO_2 experiences has already been linked to bulk properties like viscosity.[17] As such, there is much interest in investigating these environments further and in a broader scope of materials. The reported kinetics and dynamics of CO_2 in the 50 vol% ion gel reflects both IL-like and polymer-like attributes, which indicates that CO_2 is able to specifically probe the interfacial regions of this type of material. This work presents a new model for how vibrational energy is redistributed in CO_2, identifies and explains a previously unreported hot ground state of CO_2, and describes a method for extracting both kinetics and dynamics simultaneously using kinetics-adapted global fitting methods.

4.6 Acknowledgements

The authors acknowledge financial support from the National Science Foundation (CHE-1954848). C.J. Kelsheimer acknowledges funding from the Science, Mathematics and Research for Transformation Scholarship (2016-present). C.J. Kelsheimer also thanks Thomas Gasmire of the University of Pittsburgh Dietrich School of Arts and Sciences Machine Shop, Dr. Jennifer Laaser, Dr. Thomas Brinzer, Ms. Sunayana Mitra and Mr. Kai Gronborg for their assistance.

5.0 Environment Distribution in Ion Gels: A Core-Shell-Matrix Hypothesis

5.1 Chapter Summary

Using ultrafast two-dimensional infrared (2D-IR) spectroscopy, we measure frequency fluctuation dynamics of carbon dioxide (CO_2) in a series of ion gels composed of cross-linked poly(ethylene glycol)diacrylate (PEGDA) and 1-ethyl-3-methylimidazolium bis(trifluoromethylsulfonyl)imide ([emim][Tf_2N]). Thirteen total samples across six proportions were prepared, and linear and two-dimensional infrared spectra of CO_2 were measured in each of them, with replication where possible. Linear IR measurements show a linear solvatochromic shift of the ν_3 band center frequency from high frequency (pure ionic liquid) to low frequency (pure polymer) and a higher full width at half max for all mixture samples when compared to the pure substances. Center line slope analysis of the 2D-IR data reveals an unexpected, nonlinear trend in dynamics timescales. To understand this, we propose that within an ion gel, there are three possible environments: core, shell, and matrix. CO_2 experiences different dynamics in each of these environments. To support this hypothesis, we show that the non-linear trend can be fit to a model composed of three volumetric regimes and a pair of equlibria to examine the partitioning of CO_2 between the phases as a function of volume percent ionic liquid. The environment of, and therefore the interaction of CO_2 with, an ion gel is complex, even relative to the pure parent compounds, and this analysis attempts to unravel one of these complexities.

5.2 Introduction

Despite pressing environmental concerns, the continued demand for fossil fuel-based energy generation will cause the continued increase in atmospheric concentration of anthropogenic greenhouse gases such as carbon dioxide (CO_2).[1,107] To combat this, carbon capture and storage has been proposed and implemented as a method of removing the most damaging of gases from the exhaust flue.[1,4,7] Currently, amine absorption systems of carbon capture dominate the market, despite high energetic costs.[1,10,184]

One potential replacement for the amine absorption system is an ionic liquid (IL) based system, which has lead to the investigation of the physical, chemical, and mass transport properties of these materials.[1,3,184] For gas separation applications, high viscosity inhibits flowing the ionic liquid through a separations system, or flowing CO_2 through the ionic liquid This slow mass transport results in inefficient and energetically expensive separation.[3,42,44,74] Combating this, membrane-based separations work at mild conditions and have low energy consumption, small plant footprints and easily scaled syntheses.[110,185]

Ion gels[60,61,84], supported ionic liquid membranes (SILMs)[86,87], and poly-ionic liquids (PILs)[73,111] are composite materials and access the benefits of both separation processes. SILMs entrap CO_2 primarily through capillary forces. This limits the range of transmembrane pressures this membrane can withstand.[74] PILs have shown significant promise in terms of gas separations properties but can be expensive to synthesize, requiring specialized materials and knowledge.[69,74,92] Ion gels combine an IL and a polymer, and are mixed prior to polymerization. This allows for both physical and chemical entrapment of the ionic liquid within the cross-linked membrane structure. Favorable combinations of IL and polymer lead to optically clear, manipulable, dry gels.[60,81,95] Ion gels can be made by mixing any ionic liquid and commercially-available cross-linking polymer together and then polymerizing them. This leads to a significant number of potential combinations of IL and polymer, and allows the material to be optimized for stability, polymer and IL miscibility, and CO_2 capture efficiency.[60,61,81,95]

2D-IR spectroscopy is a third-order nonlinear technique that, using three ultrafast pulses of IR light, elucidates information about the coupled dynamics of a chromophore and its environment.[11] Our group has used 2D-IR spectroscopy to investigate frequency dynamics in ionic liquids, polymers, micelles, and other systems.[16,17,20,178,186,187] Atomistic modeling led to an understanding of the underlying causes of a static frequency shift between ILs and spectral diffusion.[33–35,48] Shin *et al.*[86] investigated a SILM type composite membrane consisting of a poly-ether sulfone gel and an imidazolium-based IL. For both CO_2 and $SeCN^-$, dynamics were significantly slowed when measured in the polymer environment.[86,87]

In our previous work, we examined the interaction between CO_2 and a set of samples that included a 50% v/v ion gel and compared it to its parent compounds, a sample of pure ionic liquid, and a cross-linked polymer gel.[187] This work showed that CO_2's antisymmetric stretching frequency, intramolecular vibrational relaxation processes, and frequency fluctuation dynamics were dependent on the composition of the material.

We hypothesize that there are three types of environments that CO_2 may experience within the composite materials: the polymer-like *matrix*, the IL-like *core*, and the interfacial *shell*. Both reorientation and frequency dynamics of water confined in systems such as water in oil reverse micelles or nanodroplets were previously explained using a core/shell model, where the core represented the bulk-like interior of the reverse micelle, and the shell was the water strongly hydrogen bonded to the ionic surfactants. These strong interactions slowed the dynamics at the interface.[89–91,180,188,189]

We predict that these materials are well-mixed and homogeneous, and we believe that CO_2 is going to interact preferentially with ionic liquid. As such, the interfacial *shell* is not a phase boundary, but rather a region of the material where CO_2 interacts with both ionic liquid and polymer. This is different from *matrix*, where CO_2 interacts only with polymer, and *core*, where the CO_2 interacts with ionic liquid surrounded by other ionic liquid molecules.

In this work, we investigate how the composition of an ion gel affects the energetic and molecular environment experienced by CO_2. We use a combination of techniques including Fourier-transform infrared spectroscopy (FTIR) and 2D-IR to investigate the effect of volume percent composition (from 100% ionic liquid to 100% cross-linked polymer) on the environment experienced by and frequency dynamics observed for CO_2 in these materials. We compare these experimental results to the core-shell-matrix model.

5.3 Methods

The ionic liquid ([emim][Tf_2N]) is obtained from IoLiTec (figure 5.1a). Poly(ethylene glycol) diacrylate (PEGDA, $M_n = 700$, figure 5.1b) and photoinitiator, 2,2-Dimethoxy-2-

phenylacetophenone (DMPA), are obtained from Sigma Aldrich. Bone dry CO_2 (99.8% purity) was obtained from Matheson TRIGAS.

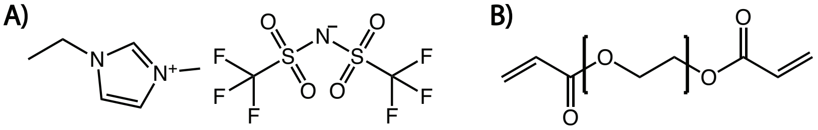

Figure 5.1: A) Ionic liquid 1-ethyl-3-methylimidazolium bis(trifluromethylsulfonyl)imide ([emim][Tf_2N]). B) The repeat unit of Poly(ethylene glycol) diacrylate. The molecule used in this work has ∼14 repeat units.

For all samples that include PEGDA, 1% by weight DMPA is added, and the sample is allowed to stir for a minimum of 3 hours. The sample mixtures are made in a glove bag to reduce water content. Samples are labeled in the format (100-X)P - (X)I, where X is the volume percent ionic liquid (*i.e.* a gel made with 75% polymer and 25% IL would be labeled 75P-25I).

For the pure ionic liquid sample, CO_2 is loaded using a vacuum sealed sample vial. The sample is heated to ∼70 °C and stirred while CO_2 is flowed into the vial for 10 minutes. Once loaded with CO_2, ~1 µL is placed between two CaF_2 windows separated by a polytetrafluroethylene (PTFE) spacer, and is then immediately placed into the N_2-purged FTIR spectrometer for measurement before being transferred to the 2D-IR spectrometer.

To form a cross-linked gel, $\leq$ 1 µL of the sample mixture is placed between two CaF_2 windows, pressed to the depth of the PTFE spacer by a hollow cylinder weight, and exposed to a 36 W UV lamp (MelodySusie) for ~2 minutes for cross-linking. To enable CO_2 loading, gels are made on drilled CaF_2 windows. To load CO_2, the flow cell assembly is placed into a N_2-purged FTIR measurement chamber. Gas lines are attached to the cell, allowing a small pressure ($<$ 10 kPa, per tank regulator) of CO_2 to flow into the cell and exhaust via exit tubing to atmosphere.

Solid samples are enclosed in the sealed N_2 environment of the FTIR chamber and exposed to CO_2 until the intensity of the CO_2 antisymmetric stretch peak ($\sim$ 2340 cm^{-1}, figure 5.2) stabilizes. The height of this peak was also used to determine the ideal depth of the polymer, aiming to match the peak height for the antisymmetric stretching peak in the IL sample. Variable sample depths (6-25 µm) were used to control for maximum CO_2 absorption. FTIR spectrum comparisons, where relevant, are corrected for these path length discrepancies.

FTIR spectra are taken on a N_2-purged Thermo Fischer Nicolet FTIR spectrometer, taking 4-8 scans with 0.5 cm^{-1} resolution. 2D-IR spectra are collected utilizing a Ti:Sapphire chirped pulse amplifier laser system ($\lambda = 805$ nm, 5 kHz repetition rate, 120 fs pulse duration) (Coherent Vitesse/Coherent Legend Elite). The mid-IR pulses are generated using a home-built optical parametric amplifier (OPA), designed to suppress noise.[104] The pulses are tuned to 4.3 µm, with energies of ~2.2 µJ as they enter the spectrometer.

The 2D-IR spectrometer employs a pump-probe geometry.[150] A Mach-Zender interferometer controls the first delay time, and a translation stage controls the second. The signal field is emitted along the path of the probe pulse. The signal, ω_3, is diffracted across a 150 l/mm grating onto a liquid N_2-cooled 2×32 channel mercury cadmium telluride detector. Signals are gated, integrated, digitized, and transmitted to a lab computer using a Femtosecond Pulse Acquisition System (Infrared Systems Development Corp.), and all data is organized and analyzed using Matlab software (Mathworks).

Center line slope analysis was used as the measure of CO_2 dynamics.[98] Error bars on frequency fluctuation correlation function (FFCF) plots reflect the uncertainty in center line slope. The FFCF was modeled with a biexponential, including two amplitudes (A) and two timescales (τ). For linear spectra, in order to analyze the variation in center frequency, the CO_2 region was modeled as the sum of two Voigt functions separated by a variable difference in center, using a bounded minimization.

5.4 Results and Discussion

5.4.1 Linear IR Spectroscopy

The antisymmetric stretch, ν_3, absorbs around 2340 cm^{-1} in all samples. A shoulder band appears at 12-13 cm^{-1} lower frequency than the main band. This shoulder results from thermal excitation of the ν_2 bending mode which is anharmonically coupled to the ν_3 mode.[17] This band is between 5 and 9% of the main band intensity for all samples, which is reasonable, given the theoretical estimate of 7% from the Boltzmann distribution. The CO_2 antisymmetric stretch absorption peaks for each sample are background subtracted, normalized, and color coded by their vol % (figure 5.2).

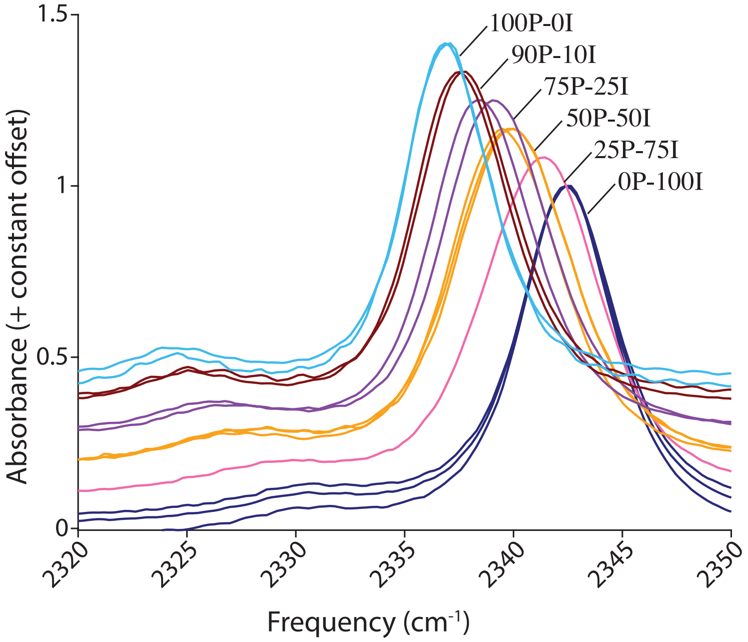

Figure 5.2: FTIR of all CO_2-ν_3 vibrational bands and shoulders for the 6 gel compositions. The spectra are offset along the Y-axis by a constant value that changes with composition, but the X-axis is not manipulated in any way.

This portion of each spectrum is fit to the sum of two Voigt functions with variable amplitudes and offset by the separation, in wavenumbers, between the main ν_3 band and the shoulder. The ratio of shoulder to main band intensity fell within a reasonable range

(5-9%) of the theoretical 7% population of the one-quantum-of-bend (1qb) mode at room temperature.[17]

Two trends in the FTIR analysis confirm earlier observations.[187] CO_2 in the pure polymer (100P-0I) has the lowest center frequency, and the pure IL (0P-100I) has the highest. In each of the ion gels, the center frequency falls linearly between the pure compounds. The shoulder offset falls between 12 and 13 cm^{-1}, and therefore the center frequency of the shoulder peak also follows the same linear trend (figure 5.3a). Prior investigation into solvatochromic shifts, in ionic liquids, identified geometric distortion and electrostatics as influences on CO_2's center frequency.[17,33] The dielectric constants are similar, which rules out electrostatics as a primary contributor to the solvatochromic shift.[151,152] Likely, increasing polymer content creates greater steric hindrance. This shifts the frequency lower. A similar effect is seen in long-chain alkanes (*e.g.* hexadecane 2335.1 cm^{-1}).[143]

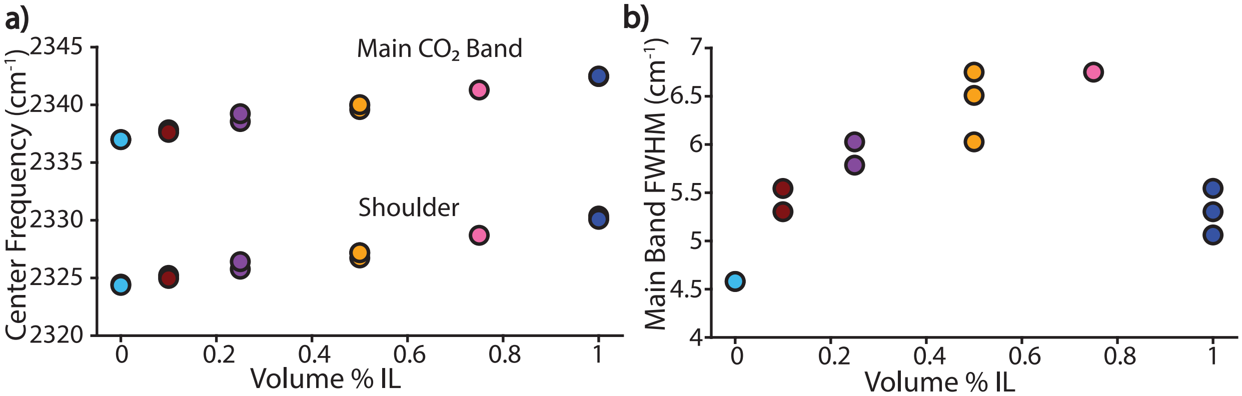

Figure 5.3: a) There is a linear relationship between vol% IL, the center frequency of the main ν_3 band, and the center frequency of the shoulder. b) The FWHM does not follow a linear trend, with the smallest FWHM values corresponding to the pure substances and all mixtures broadening by at least 1 cm^{-1}.

The full width at half maximum (FWHM) does not scale linearly with the IL vol% (figure 5.3b).The lowest FWHM, 4.6 cm^{-1}, belongs to the 100P-0I samples. The 0P-100I, pure IL sample is the next lowest, with FWHM of 5.1-5.6 cm^{-1}. All of the composite materials show broader lines than both pure substances. We have previously postulated that the variety in environments (IL-like, polymer-like, and interface-like) in the 50P-50I gel causes this line broadening. The trend in this work support the conclusion that in systems where the environment can be complex, such as an interface, CO_2 can experience a greater range of instantaneous frequencies.

5.4.2 Experimental 2D-IR Spectra

Thirteen sets of 2D-IR data were measured. Data from all of the experiments is available in the supporting information, but a representative sample set, the three 50P-50I samples, is provided in figure 5.4.

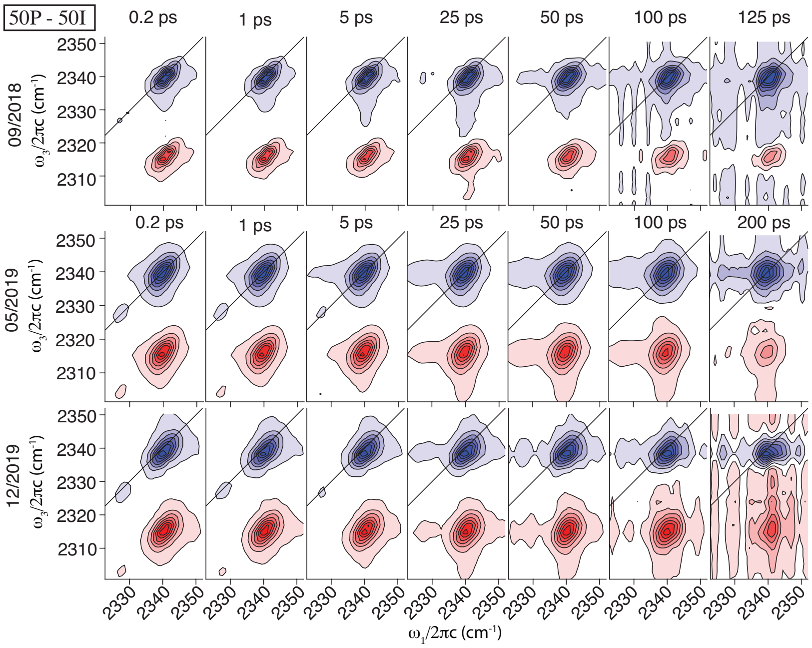

Figure 5.4: 2D-IR spectra for three samples of 50P-50I. For the first set of spectra, 09/2018, data was not measured beyond $t_2 = 125$ ps. All spectra have two main bands at 2340 cm^{-1} on the ω_1 axis, one blue and one red. The top row, 09/2018 spectra, appear to have a slightly smaller peak compared to the two 2019 samples, and the shoulder (12 cm^{-1} red-shifted along the diagonal) is low enough in intensity that it only shows up in the earliest spectrum. The two samples in 2019 are more consistent and measure out to 200 ps. In general, the change of peak shape is consistent for all three samples despite discrepancies between the measurements.

In each of the earliest spectra (0.2 ps) there are two large bands: one blue, negative peak and one red, positive peak. Additionally, in each of these spectra there is the shoulder peak along the diagonal, shifted 12 cm^{-1} lower. When the spectrum is limited to only the smallest 50% of intensities, the shoulder bands are more easily visible.

The peaks change shape over time. The large blue peak in all three 0.2 ps spectra appears to have a high degree of correlation, evidenced by the peak being relatively narrow along the diagonal. Over time, the peak broadens. Notably, in this sample, even at longer times, the peak does not appear particularly round, which is a hallmark of spectral diffusion. This is characteristic of polymer-containing samples.

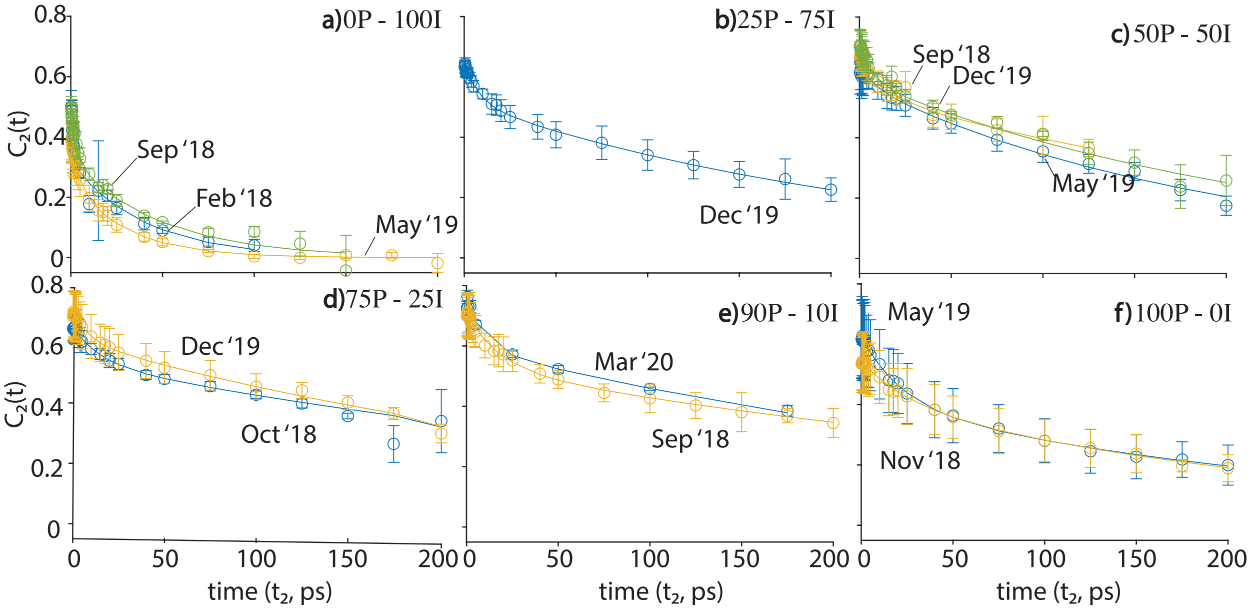

Figure 5.5: Frequency fluctuation correlation function (FFCF) plots were calculated for all samples. Here, we can see that generally, despite temporal and sample variability, the dynamics reported stay reasonably consistent. Error bars represent uncertainty in the center line slope fit.

The change of peak shape is measured using center line slope and plotted as a function of t_2 (figure 5.5, points). Aside from the 25P-75I sample (b), which was only measured once, each of the samples show a high degree of agreement in the shape of the curves measured.

To extract frequency fluctuation correlation functions (FFCF), the curves are fit to a biexponential decay (figure 5.5). These functions consist of two amplitude coefficients and two time coefficients, representing generally the amount of correlation lost and on what timescale this loss occurred. Table 5.1 records the outputs of these fits, including errors representing the 95% confidence intervals for the fit values.

Table 5.1: Correlation Function Fit for All Samples

Sample	A1	τ_1 (ps)	A2	τ_2 (ps)	τ_{corr} (ps)
0P-100I	0.24 ± 0.04	1.1 ± 0.3	0.32 ± 0.02	40 ± 4	13.1 ± 0.8
0P-100I	0.17 ± 0.03	3.1 ± 1.3	0.33 ± 0.02	49 ± 4	16.5 ± 0.9
0P-100I	0.15 ± 0.03	4.0 ± 1.9	0.26 ± 0.02	30 ± 2	8.4 ± 0.5
25P-75I	0.12 ± 0.02	8.5 ± 2.4	0.52 ± 0.02	242 ± 24	126 ± 7
50P-50I	0.13 ± 0.03	13.1 ± 4.7	0.55 ± 0.03	312 ± 54	172 ± 16
50P-50I	0.06 ± 0.03	7.8 ± 10	0.58 ± 0.03	192 ± 18	112 ± 6
50P-50I	0.12 ± 0.02	7.1 ± 3.0	0.59 ± 0.01	233 ± 17	139 ± 6
75P-25I	0.12 ± 0.02	15 ± 4	0.53 ± 0.02	436 ± 49	235 ± 14
75P-25I	0.10 ± 0.02	8.9 ± 4.0	0.61 ± 0.01	344 ± 20	210 ± 7
90P-10I	0.18 ± 0.02	18.5 ± 4.3	0.53 ± 0.02	479 ± 65	256 ± 18
90P-10I	0.16 ± 0.04	9.4 ± 8.3	0.59 ± 0.04	387 ± 114	232 ± 36
100P-0I	0.13 ± 0.03	26 ± 9	0.41 ± 0.03	260 ± 32	111 ± 8
100P-0I	0.23 ± 0.02	23 ± 4	0.40 ± 0.02	284 ± 29	118 ± 7

The total correlation time, τ_{corr}, is calculated by integrating the analytical fit to FFCF curve from $t = 0$ to ∞ (table 5.1). It can also be considered a weighted average of the two timescales of molecular motion. This quantity is a useful point of comparison between samples.

In general, the fits and time constants extracted is self-consistent between samples of the same composition. Looking at the FFCF plots (figure 5.5), the initial time constant is reflected as the slope of the data for early t_2 times, which does appear to grow less steep with the addition of the polymer component. Additionally, beyond the IL, all of the FFCFs start at larger initial correlation values and even at very long times do not appear to decay to zero, as is seen in the pure IL sample.

To assess water content impacts, the integrated correlation time (τ_{corr}) was compared to the water content extracted from FTIR spectra, using an approximate molar absorptivity for dissolved water of 100 $\text{M}^{-1}\text{cm}^{-1}$.[20] There was no reproducible effect of water content on the dynamics recorded (figure 5.6), and so water content was disregarded as an explanation

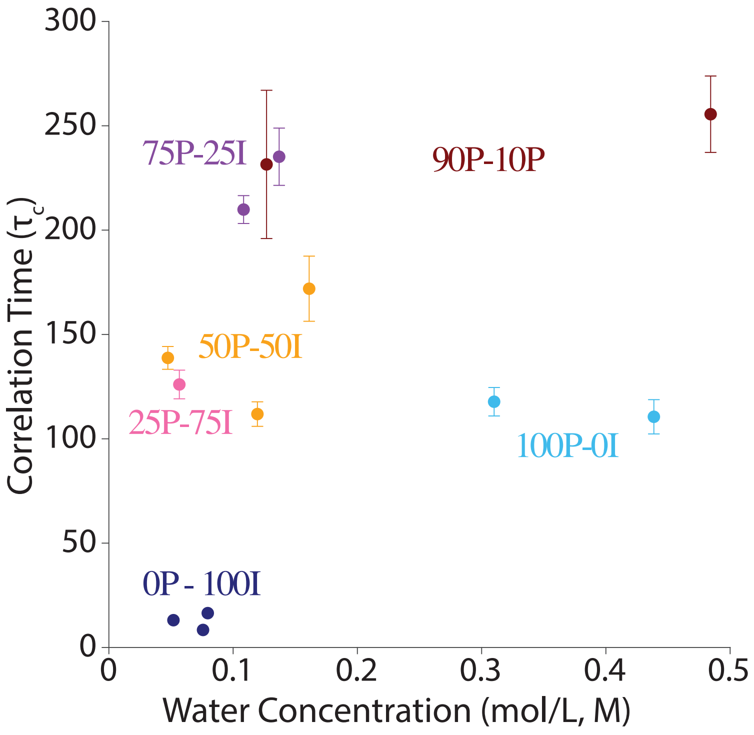

Figure 5.6: The integrated correlation time (τ_{corr}) shows no clear impact of water content. The water content was extracted from FTIR spectra.

for variation in the time constants reported by CLS analysis.

In our previous work, we reported a linear trend of τ_{corr} as a function of vol% measured for the 100P-0I, 50P-50I, and 0P-100I sample sets. We expected, upon measuring additional samples, for them to fall along a linear trend line, as would be the case for a simple ideal-mixing scenario. Figure 5.7 shows that this is not the case.

Correlation time as a function of vol% IL initially increases at low vol% IL and then decreases as the vol% grows larger (figure 5.7a). The correlation time is a weighted average of the two time constants extracted. To investigate this, we also plot the time constants individually as functions of vol% (figure 5.7b,c) which shows that, of the two, the long time constant (τ_2) is the dominating influence on the trend seen for the τ_{corr} values.

In order to explain this unexpected relationship between vol% and dynamics, we investigate the three phases we hypothesize are present in the material: core, shell, and matrix.

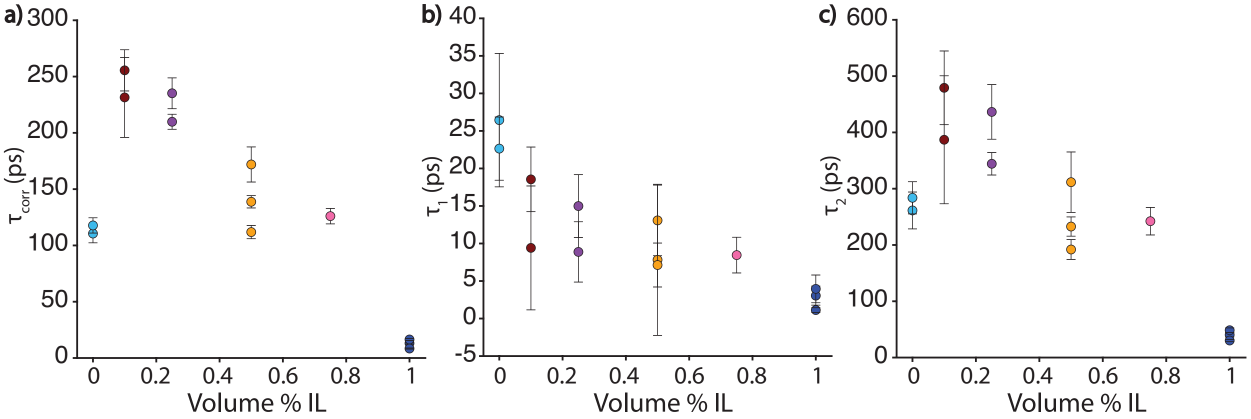

Figure 5.7: Values extracted from FFCF fits do not follow a linear trend as functions of vol% IL. a) The total correlation time becomes significantly slower at low vol% IL values, and then decreases consistently towards the pure IL. b) The first time constant, τ_1, decreases with increasing vol% IL. c) The second time constant,τ_2, appears to be the dominant influence on the correlation time, increasing at low vol% IL and then decreasing.

The goal of this process is to use the vol% IL dependent CO_2 proportions in each environment in order to interpret the non-monotonic trend of correlation time with vol% IL. We assume that the total correlation time for the composite system is a weighted combination of the correlation time for CO_2 in each type of environment.

To construct the model for our three-environment system, it was first necessary to identify the volume distribution of the various components as a function of vol%. All volumes are normalized to a total volume of 1 µL and are therefore reported as vol%. The volume distribution of the sample has three regimes: nucleation, growth, and coalesence.

At $\text{vol}\%_{\text{IL}} = 0$, all of the environment is matrix: there is no core, and there is no shell. We begin in the nucleation regime. As we add ionic liquid, up to a value V_{crit}, all ionic liquid is added as individual nuclei of a minimum radius, r_{min}, and is assumed to be shell. Beyond V_{crit}, we enter the growth regime, where the volume of core begins to grow. The volume of shell is interpreted as an outermost layer of ionic liquid around the inner core, where the total radius is $d_s + r_{core}$ for each nucleus. The total ionic liquid volume is spread between some number of nuclei, n, where $n_{crit} = V_{crit}/V_{min}$ – or the number of individual ion pair spheres needed to add up to this critical volume. The third regime, coalesence, begins at $0.74{*}V_T$. Above this volume fraction, the spheres must overlap. We approximate this as a linear loss of shell and gain of core. As the cores continue to grow, the shell portions begin to overlap and thereby decrease, eventually leading to the full IL-like environment (figure 5.8 a,b).

Once the volumes of total core, shell, and matrix have been established, we then calculate the partitioning of CO_2 between these environments as a function of vol% IL with coupled equilibria

$$[M - \mathrm{CO_2}] + [S] \xrightarrow{K_{MS}} [S - \mathrm{CO_2}] + [M], \tag{28}$$

$$[S - \mathrm{CO_2}] + [C] \xrightarrow{K_{SC}} [C - \mathrm{CO_2}] + [S], \tag{29}$$

where $[M]$ and $[M - \mathrm{CO_2}]$ refer to the concentration of matrix and CO_2 in the matrix, respectively, and S, $S - \mathrm{CO_2}$, C, and $C - \mathrm{CO_2}$ follow the same pattern for shell and core. The constants K_{MS} and K_{SC} govern the matrix-shell and shell-core equilibria. The abrupt change in dynamics observed between $\mathrm{vol\%}_{\mathrm{IL}} = 0$ and 0.15 (figure 5.7a) suggests that the matrix-shell equilibrium lies far to the right. We use this to separate the two equilibria and treat them separately. In this approximation, by V_{crit}, when the volume of core begins to grow, all of the CO_2 present is in the shell, and residual CO_2 in the matrix can be neglected.

We hypothesize that the partitioning of CO_2 between shell and matrix strongly favors the shell. Alternatively, between shell and core, the equilibrium is not shifted as far to the right, but does favor the core. Mass balance implies

$$\begin{aligned}[M_0] &= [M] + [M - \mathrm{CO_2}]\\ [S_0] &= [S] + [S - \mathrm{CO_2}]\\ [C_0] &= [C] + [C - \mathrm{CO_2}],\end{aligned} \tag{30}$$

and

$$[\mathrm{CO_2}]_T = [M - \mathrm{CO_2}] + [S - \mathrm{CO_2}] + [C - \mathrm{CO_2}]. \tag{31}$$

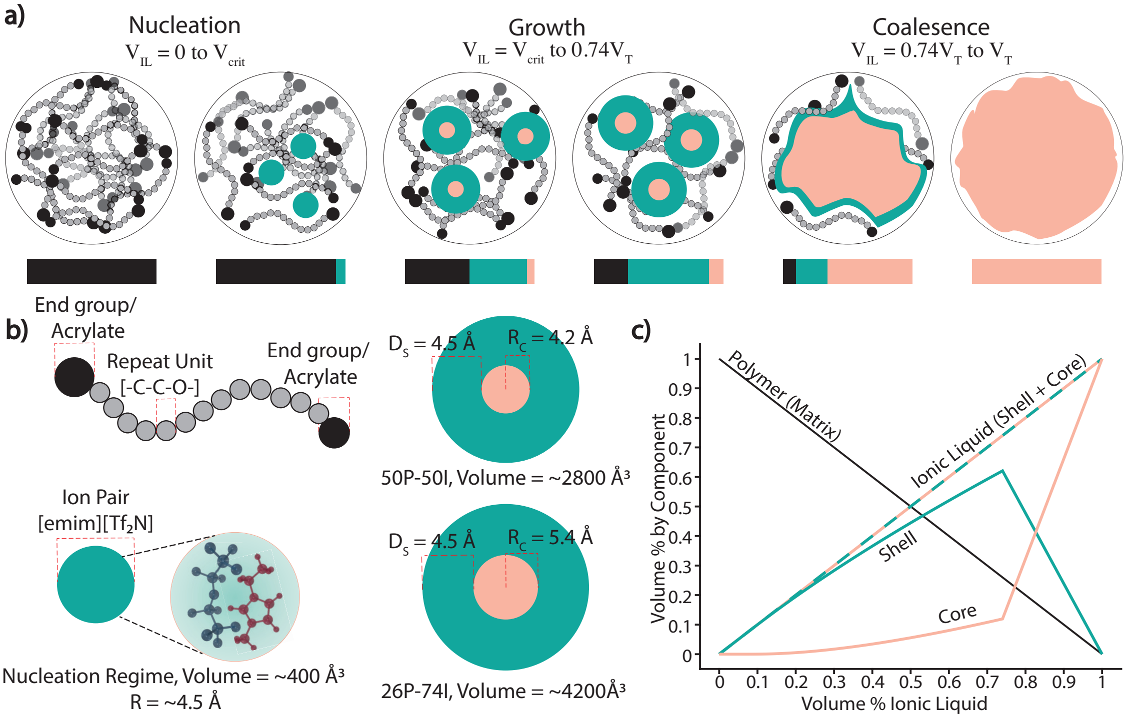

Figure 5.8: The ion gel environment depends on the proportion of IL and the division of that IL into shell and core. a) The nucleation regime contains only matrix and shell. Up to V_{crit}, spherical ion pairs populate free volume in the polymer matrix. In the growth, above V_{crit}, the core grows in size, and the shell becomes an outer layer. The coalesence regime is beyond the maximum sphere packing limit, and from there core grows steadily and shells condense, causing a decrease in the shell volume. b) PEGDA molecules have an average molecular weight of 700 g/mol and is composed of its acrylate end groups and $\sim$13 repeat units. The shell, initially an ion pair, has a radius of $\sim$ 4.5 Å. As the ionic liquid region begins to grow, it expands to 7x and 10x the volume of this initial ion pair, with the core composing 11% and 15% respectively. The spheres are no longer distinct in coalescence. c) The volume of polymer decreases linearly from 1 to 0, and ionic liquid increases from 0 to 1. Shell and core add up to the total ionic liquid, and the total volume is constant.

Using the above equations and assumptions, and approximate concentrations of pure PEGDA (1.6 M), pure [emim][Tf_2N] (3.8 M), and CO_2 (0.15 M), we calculate vol% dependent proportions of CO_2 in each of the three environments (figure 5.9a). For demonstration purposes, the K_{MS}, K_{CS}, and critical volume fraction (V_{crit}) were selected to give us the best agreement with experimental data (figure 5.10, table 5.2).

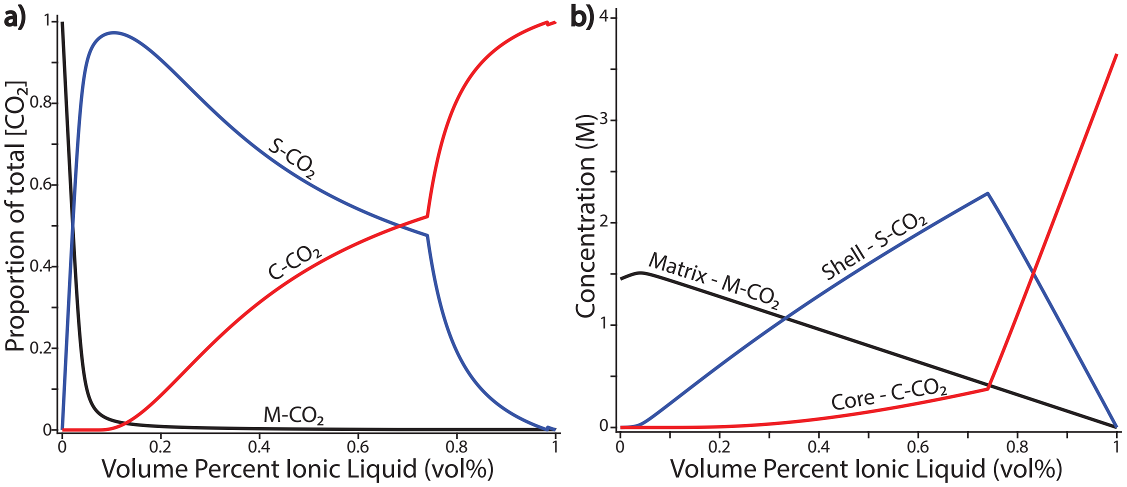

Figure 5.9: The environment CO_2 experiences depends on the composition of the ion gel. a) The portion of total CO_2 in each environment as a function of vol% IL. Low vol% IL leads to a rapid growth of the shell-type environment, and continued addition of ionic liquid leads to the loss of the shell environment, and an increasing core environment. b) The concentration of each environment with the amount of CO_2-saturated environment subtracted. The matrix begins just below its maximum value of 1.6 M, The shell and core follow the same trend as their volumes (figure 5.8).

To calculate the total correlation time for the system, we weight the sum of the time constants by their vol% IL dependent value,

$$\tau_{corr}(X) = A_M(X)\tau_M + A_S(X)\tau_S + A_C(X)\tau_C. \tag{32}$$

X is the vol% ionic liquid, and $A_M(X)$, $A_S(X)$, and $A_C(X)$ are the vol% dependent CO_2 portion calculated above. τ_M is the average of the experimentally determined correlation times for CO_2 in a pure matrix environment (100P-0I, table 5.1). τ_C is the average of experimentally determined correlation times for the pure core, or pure IL environment (0P-100I, table 5.1). τ_S is another adjustable parameter that is set to a value near the highest correlation time recorded, as a measure of correlation time in a mostly-interfacial, or primarily-shell, sample (table 5.2). Using equation 32 and the parameters in table 5.2, the resulting curve fits the correlation time data (figure 5.10). The agreement between model and experiment is consistent with our proposed hypothesis of three environments within the ion gel. The overall dynamics CO_2 reports is fixed by the composition of the ion gel.

Table 5.2: Core-Shell-Matrix Parameters

Variable Parameters		Fixed Parameters	
V_{crit}	0.07	τ_C	114.2 ps
K_{MS}	250	τ_M	12.6 ps
K_{SC}	6.25		
τ_S	255 ps		

2D-IR reports the dynamics of CO_2 as it interacts with its local solvation shell, which depends on the relative motion of the CO2 and its solvation shell. Reorientation-induced spectral diffusion (RISD) is the result of CO_2 moving in a fixed shell, and structural spectral diffusion (SSD) is the result of the shell moving around a fixed CO_2. In chapter 6, we demonstrate that spectral diffusion in ion gels is dominated by RISD, *i.e.*, the CO_2 moves in a more or less fixed environment.

Previously, we hypothesized that the dynamics and kinetics that CO_2 experiences in a composite material reports the interfacial environment. The kinetics of intramolecular vibrational relaxation for CO_2 in the ion gel (a 50 vol% sample) differed from both the pure IL and the pure polymer, indicating that the environment CO_2 experienced was different than in the parent materials.[187] The core-shell-matrix model here reinforces this conclusion. At very low IL vol%, we see an initial, high proportion of shell environment and a slow growth of the core as IL vol% is increased. CO_2 in ion gels of various compositions experiences a unique, blended environment.

An additional factor to note is the impact of cross-linking these membranes. Due to the short PEGDA chains (∼13 repeat units), the effect of the acrylate cross-links cannot

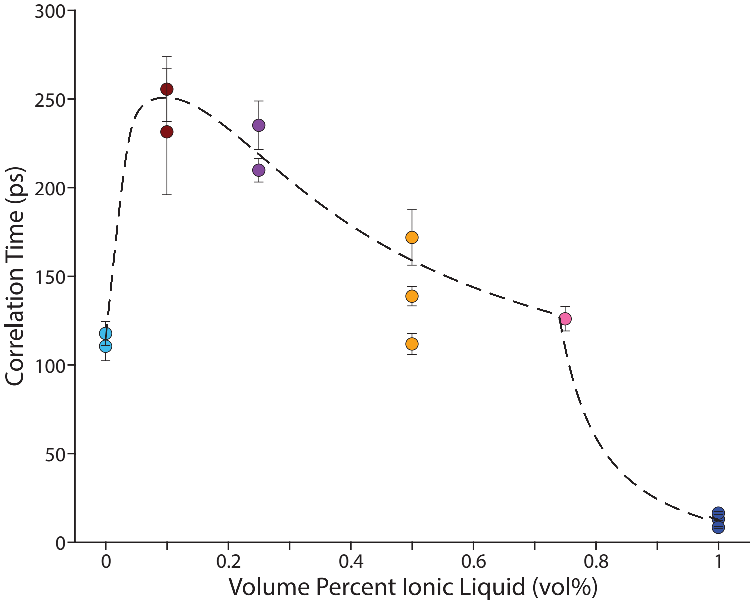

Figure 5.10: Using the vol% IL dependent proportions of CO_2 in each environment to scale the contribution of each time constant produces a function that traces the shape (dashed line) of the experimental correlation times (points). This line is calculated by selecting the inputs for a best fit.

be discounted. The cross-links reduce the motion of the poly(ethylene glycol) chains, and in turn, the molecules they interact with. Increasing IL content could impact this cross-linking in several ways: both the disruption of inherent packing structure, and mobilization or lubrication of the PEG regions. In work by Kusuma *et al.*[61], increasing IL content or the cross-link complexity led to higher permeability and lower selectivity.[61] This coincides with our trend of increased dynamics as ionic liquid content increases, which may disrupt, or increase the distance between, the cross-linking to a greater degree.

The model constructed to reproduce these observations has implications for material design. At low IL vol%, we observe slow CO_2 dynamics. Slow dynamics may reduce the effective diffusion coefficient for CO_2 through the material, leading to a decrease in permeability. If the goal of adding ionic liquids to the polymers is to improve separation behavior, the reduced permeability may limit the separation efficiency. On the other hand, the increase in residence time in the shell regions could lead to an increase in selectivity. Further testing is needed to understand the bulk implications of this model.

5.5 Conclusion

In this work, we investigated a series of 6 [emim][Tf$_2$N]-PEGDA ion gels, ranging from the pure polymer (100P-0I) to the pure ionic liquid (0P-100I). 2D-IR spectra were analyzed using center line slope fitting in order to extract FFCFs and a measure of structural reorganization timescales. The resulting plot of correlation time versus vol% IL was then fit to a core-shell-matrix model.

The FTIR experiments agree with prior observations of a solvatochromic shift in the center frequency of the ν_3 peak of CO$_2$ (figure 5.3a).[17,46,86,143] We identify steric hindrance and conformation restrictions as a result of added polymer component as a likely cause for this shift in center frequency. Additionally, FTIR experiments showed that the mixed-matrix samples had larger FWHM values as compared to the pure substances. This is likely due to the variety of environments generated by the core, shell, and matrix regions in the gel.

The FFCFs extracted from 2D-IR spectra showed good agreement between samples of the same composition (figure 5.5). There was a clear impact of the presence of PEGDA even at the lowest (25P-75I) portion, where the starting correlation and the rate of the decay are already impacted, by up to an order of magnitude in the case of correlation time (table 5.1). There was no clear impact of water composition on the dynamics recorded (figure 5.6).

The plot of correlation time as a function of vol% IL resulted in an unexpected trend (figure 5.7a,5.10). At 90 vol% IL, CO$_2$ dynamics are almost two times slower than in the pure IL. They then accelerate with increasing vol% IL beyond the 90P-10I sample. This non-monotonic trend deviated from the mostly linear trend that was extracted using global fitting.[187]

A model explains the trend as the partitioning of CO$_2$ into three environments in the ion gel: an IL-like core, an interface-like shell, and a polymer-like matrix. We used a paired equilibria to estimate the vol% dependent fraction of CO$_2$ in each of three environments. These fractions were used to weight the time constants for matrix and core (fixed by experiment) and shell (variable) (figure 5.10, equation 32, table 5.2).

The model, with the inputs listed in table 5.2, agrees well with the experimental data, most notably the small difference in dynamic timescales between 50P-50I and 25P-75I, compared to the order of magnitude difference between 25P-75I and 0P-100I. The increased FWHM and core-shell-matrix models, taken together, imply that even within a small spatial range, the matrix that the chromophore experiences can vary. The non-linear trend of correlation times and the strong dependence of this trend on the slow relaxation (τ_2) implicates the structural reorganization of the gel (and perhaps shifting of population between environments) as a key factor in determining the interaction of CO_2 with these samples.

5.6 Acknowledgements

The authors would like to acknowledge Thomas Gasmire, of the University of Pittsburgh Machine Shop for fabrication of sample cells. Additional thanks to the National Science Foundation (CHE-1954848, S. G.-R.), and the Science, Mathematics and Research for Transformation (SMART) Scholarship (C.J.K. 2016-present).

6.0 Modeling the Frequency-dependent Two-dimensional Anisotropy

6.1 Chapter Summary

Polarization-controlled ultrafast two-dimensional infrared (2D-IR) spectroscopy measurements of CO_2 in a 50% by volume cross-linked poly(ethylene glyol) diacrylate / 1-ethyl-3-methylimidazolium bis(trifluromethylsulfonyl)imide ion gel show frequency dependence in their anisotropy. The slow frequency fluctuation dynamics (correlation times above 100 ps) in ion gels create an ideal system to examine effects of reorientation-induced spectral diffusion (RISD). The RISD effect is extracted using a wobbling-in-a-cone model with a 2nd order Stark effect approximation (appropriate for quadrupolar systems). Frequency dependent anisotropy was examined by calculating an anisotropy value for every frequency pair on the 2D-IR contour plot. Using a model built on the approximations of inhomogeneous broadening and Gaussian statistics as well as the the extracted polarization-weighted FFCFs from experiment, we show that the frequency dependence in the measured 2D anisotropy is the result of RISD.

6.2 Introduction

Polarization controlled ultrafast two-dimensional infrared (2D-IR) spectroscopy offers insight into the local environment of a chromophore.[11] In general, 2D-IR spectroscopy uses three ultra-short pulses and the resultant molecular response to interrogate a chromophore about the fluctuation of its surroundings. Various polarization schemes allow for control over cross-peaks, elimination of diagonal peaks, and isolation of rotational dynamics and their effect on the overall frequency fluctuations..[11,190–192]

2D-IR spectroscopy is a third-order nonlinear spectroscopy that utilizes three ($\sim 200\ fs$) pulses of infrared light. The first two pulses are referred to as pumps, and are separated by a time, t_1. During this time, the initial frequency distribution is measured. The system then evolves unperturbed during a time, t_2, referred to as the waiting time or population time. The probe pulse then generates a coherence state, which causes the emission of a signal field. This signal field is recorded as the final frequency distribution of the system.

Control over the polarization of each pulse during a 2D-IR experiment allows for modulation of the spectra measured. The intensity of excitation scales with $\cos(\theta)$ where θ is the angle of incidence between the transition dipole moment ($\hat{\mu}$) and the incident electric field ($\hat{E}$). If the initial pulses define an initial polarization axis, which will be called $\hat{Z}$ polarization, the molecules that will be most intensely excited are those with the smallest θ. The probe pulse is either left the same or rotated by 90° to be perpendicular to the pumps, called $\hat{X}$ polarization. Molecules that were strongly excited by the $\hat{Z}$ pulses are unlikely to be strongly excited by the $\hat{X}$ pulse unless they have rotated.

Rotational anisotropy, $\alpha(t)$, is normally measured in a pump-probe experiment as the difference in parallel, $I_{\parallel}$, and perpendicular, $I_{\perp}$, signals normalized by the isotropic signal,

$$\alpha(t) = \frac{I_{\parallel} - I_{\perp}}{I_{\parallel} + 2I_{\perp}}. \tag{33}$$

Though rotational anisotropy is a standard ultrafast measurement, detailed interpretation of the frequency integrated rotational anisotropy is complicated by non-Condon effects, frequency-dependent vibrational relaxation rates, and spectral diffusion, as highlighted by Lin *et al.*[193]. Calculating rotational anisotropy directly from 2D-IR spectra – that is, without averaging over the pump and probe frequencies – may alleviate these effects.

One of the first demonstrations of two-dimensional (2D) anisotropy was by Ramasesha *et al.*[134], who noted the impact of reorientation during hydrogen bond switching in water and identified inertial orientational dynamics, which occur faster than could be measured by their experiment. Ramasesha *et al.*[134] also calculated 2D-anisotropy plots derived from experimental spectra.[134] Anisotropy is a measure of how ordered the distribution of transition dipole moment vectors is compared to an isotropic (fully randomized) distribution. The 2D-anisotropy can be calculated for every point in the 2D-IR spectrum,

$$\alpha(\omega_1, t_2, \omega_3) = \frac{I_{\parallel}(\omega_1, t_2, \omega_3) - I_{\perp}(\omega_1, t_2, \omega_3)}{I_{\parallel}(\omega_1, t_2, \omega_3) + 2I_{\perp}(\omega_1, t_2, \omega_3)}. \tag{34}$$

$I_{\parallel}(\omega_1, t_2, \omega_3)$ is the 2D-IR spectrum measured with parallel polarizations, and $I_{\perp}(\omega_1, t_2, \omega_3)$ is the 2D-IR spectrum measured with perpendicular polarizations as functions of the population time, t_2, initial frequency, ω_1, and final frequency, ω_3.

2D-anisotropy plots of water showed that strongly hydrogen bonded molecules are less likely to rotate from their initial orientation than non-hydrogen-bonded molecules. This is a more complicated frequency dependence of 2D-anisotropy compared to what arises in systems that do not experience hydrogen bonding. Additionally, the spectral diffusion of water is very fast, completing in ~ 1 ps.[134]

When reorientation of chromophore molecules happens faster than the spectral diffusion, the frequency fluctuation correlation functions (FFCF) often differ between the parallel and perpendicular polarization conditions; the perpendicular polarization condition decays to zero more quickly than the parallel. Rivera *et al.*[194] noted this discrepancy in vibrational sum frequency generation (VSFG) experiments, calling it reorientation-induced spectral diffusion (RISD). In VSFG experiments, RISD causes the underlying spectral lineshape to become time dependent.[194]

Kramer *et al.*[135] then expanded the theory to 2D-IR spectroscopy, showing that the configuration of incident light polarization generated differences in the measured spectra, and that these measured spectra reported different spectral diffusion timescales.[135] They built a quantitative model based on first- and second-order Stark effects. First-order Stark effects are a reasonable approximation for the relationship between a dipole and an incident electric field; however, they found that for a quadrupolar molecule like CO_2, a second-order Stark effect was a better model. They also showed that the frequency fluctuation correlation function (FFCF) is the product of a RISD component ($R_p(t)$) and structural spectral diffusion (SSD, $F(t)$) component,

$$C_p(t) = F(t)R_p(t). \tag{35}$$

Here, the subscript p is used to designate which polarization condition is being described, which can be either $ZZZZ$ or $ZZXX$ in this work. The product of the two functions $R_p(t)$ and $F(t)$, $C_p(t)$, is the polarization weighted frequency-fluctuation correlation function (PW-FFCF).[103,135]

The frequency-dependence of the reorientation dynamics has not been treated systematically. Kramer *et al.*[135] described a model for quantifying the effects of RISD in 2D-IR spectroscopy. RISD describes the reorientation-dependence of frequency fluctuation dynamics. Frequency-resolved rotational anisotropy measurements have shown a frequency-dependence.[134,195] Additional studies have reported that an energetic bias can cause dramatic effects in the orientational distribution, and long-lived differences in parallel and perpendicular FFCFs.[186] No quantitative model has described the association between RISD and frequency-dependence of 2D-anisotropy. That is the goal of this work.

The overall rate of spectral diffusion in polymers, ion gels, and other composite materials is considerably slower than in the bulk ionic liquid.[86,187] Slow structural spectral diffusion allows RISD to be observed, which can be indicated by discrepancies between the PW-FFCFs extracted from measurements in $ZZZZ$ and $ZZXX$ polarizations. As we were interested in examining these features, the 50 % by volume (%bv) ion gel composed of 1-ethyl-3-methylimidazolium bis(trifluoromethylsulfonyl)imide ([emim][Tf_2N]) and poly(ethylene glycol) diacrylate (PEGDA) was chosen as an example system.

In order to model the effects of orientation amplitudes and PW-FFCFs on 2D-anisotropy plots, we will use a Gaussian joint probability density. This model takes inputs from fitting the experimental system in order to investigate the link between RISD and 2D-anisotropy. This frequency dependence has been noted but not explained in the literature. This effect has been seen in other systems with prominent RISD[195] and utilizing the ion gel system, we characterize it carefully, and explain its origin.

In this work, we present polarization controlled 2D-IR spectra of CO_2 in our example system. We present frequency fluctuation correlation functions derived via the center line slope method[98] and fit to a wobbling-in-a-cone model with a second-order Stark shift.[103] The values attained through this fitting become the parameters of the Gaussian joint probability density model. To examine the frequency dependence of anisotropy, we will present both time-dependent 2D-anisotropy plots for both the experimental data and the Gaussian model to show that the characteristic frequency dependence of anisotropy is a necessary consequence of the coupling of reorientation and frequency fluctuation of the molecules.

6.3 Methods

The ionic liquid ([emim][Tf_2N]) was obtained from IoLiTec, and was used as received. Poly(ethylene glycol) diacrylate (PEGDA, $M_n = 700$) and the photoinitiator, 2,2-dimethoxy-2-phenylacetophenone (DMPA) were obtained from Sigma Aldrich. Bone dry CO_2 (99.8 % purity) was obtained from Matheson TRIGAS.

A glove bag is utilized to avoid excess water contamination. DMPA (1 % by weight) is added to the volumetric mixture of 50% PEGDA and 50% [emim][TF_2N]. The sample is allowed to stir for a minimum of 3 hours. To form the cross-linked gel, 1 µL of the sample mixture is placed between two CaF_2 windows, pressed to the depth of the 25 µm PTFE spacer by a hollow cylinder weight, and exposed to a 36 W UV lamp (MelodySusie) for ∼ 2 minutes for cross-linking.

To enable CO_2 loading, gels are made on drilled CaF_2 windows and housed in a flow cell assembly.[196] The assembled sample cell is placed into the N_2-purged FTIR measurement chamber. Gas lines are attached to the cell, allowing a small pressure ($<$ 10 kPa) of CO_2 to flow into the airtight cell, and exhaust via exit tubing to atmosphere. The PTFE spacer depth is chosen such that, at saturation, the antisymmetric stretch peak ($\sim 2340\text{cm}^{-1}$) has an absorbance of 0.3 OD.

FTIR spectra are taken on a N_2-purged Thermo Fischer Nicolet FTIR spectrometer, taking 4-8 scans with 0.5 cm^{-1} resolution. 2D-IR spectra are collected utilizing a Ti:Sapphire chirped pulse amplifier laser system ($\lambda = 805$ nm, 5 kHz repetition rate, 120 fs pulse duration) (Coherent Vitesse/Coherent Legend Elite). The mid-IR pulses are generated using a home-built optical parametric amplifier (OPA), designed to suppress noise.[104] After the OPA, the spectral bandwidth is $\sim 200\ \text{cm}^{-1}$. The pulses are ∼ 2.2 µJ and are tuned to a wavelength of 4.3 µm.

The 2D spectrometer employs a pump-probe geometry.[150] A Mach-Zender interferometer controls the first delay time, and a translation stage controls the second. The signal field is emitted along the path of the probe pulse. The signal field and probe pulses are diffracted across a 150 l/mm grating onto a liquid N_2-cooled 2×32 channel mercury cadmium telluride detector. Signals are gated, integrated, digitized, and transmitted to the lab computer using the Femtosecond Pulse Acquisition System (Infrared Systems Development Corp.), and all data is organized and analyzed using MATLAB software (Mathworks).

Polarization control is achieved using a combination of a $\lambda/2$ mid-IR waveplate (Altechna, 4500 nm) and a BaF_2 wire grid polarizer (ThorLabs, 2-12 µm) in the path of the pump pulses. The polarizer is automated to switch between parallel (0°) and perpendicular (90°) orientations. In order to reduce laser drift and noise fluctuations within the same waiting time, parallel and perpendicular measurements are performed in pairs. At each waiting time, the parallel experiment is measured, the polarizer switches orientations, and then the perpendicular measurement is recorded. To reduce the systematic effect of long-term drift in the laser, the waiting times collected in a randomized order.

When anisotropy is high, the parallel signal can be up to three times larger than the perpendicular signal.[11] Doubling the integration time for the perpendicular measurement proved sufficient to produce spectra of comparable quality to the parallel measurements.

Center line slope measures frequency correlation in 2D-IR spectra.[98] The CLS curves are then fit to a wobbling-in-a-cone model with a second-order Stark shift.[103,135] The l-th order orientational correlation functions, $L_l(t)$, are approximately

$$L_l(t) = S_l^2 + (1 - S_l^2)e^{-t/\tau_{\text{eff}}^{(l)}}. \tag{36}$$

The S_l are order parameters, which are related to how restricted the orientational motion of a given chromophore is. Functionally they are an offset. In the long time limit, the orientational correlation function decays to S_1^2. $\tau_{\text{eff}}^{(l)}$ is a function of both cone angle (θ) and the diffusion constant (D_w). The full forms of these functions are reproduced elsewhere.[103,197] The product of three wobbling-in-a-cone correlation functions,

$$L_l^{\text{tot}}(t) = L_l^{(1)}(t)L_l^{(2)}(t)L_l^{(3)}(t), \tag{37}$$

gave the best fit to the experimental data. With three statistically uncorrelated processes, the rotational correlation functions factorize, which allows each cone, labeled as $L_l^n(t)$ to be independent of the others. Each cone and timescale can be associated with a different mode of structural relaxation in the ionic liquid. We found three independent cones sufficiently described the shape of the data.

The fit is bootstrapped to provide a measure of uncertainty in the RISD fit.[106] The best fit values calculated from each repetition of the bootstrapping process ($n_{\text{boot}} = 100$) are averaged, and a 2σ value is taken as twice the standard deviation of the resulting values. Histograms depicting the spread of values for each parameter are included in the supporting information.

2D-anisotropy plots are calculated as described in equation 34. The intensity of the parallel ($I_{\parallel}$) and perpendicular ($I_{\perp}$) 2D spectra are taken as the intensity of the spectra at every frequency pair.

6.4 Results and Discussion

We build a model that brings the frequency dependence of reorientation back into the 2D-anisotropy plots. We explore a range of parameters that illustrate the behaviors that can be expected when the SSD is faster than RISD and RISD is faster than SSD. This offers an understanding of why the anisotropy plots have structured features that have been observed before.[195]

With this model in hand we report 2D-IR and 2D-anisotropy plots for CO_2 in an ion gel, replicate these plots using the model, and discuss the implications of this frequency dependence.

6.4.1 A Gaussian Model of Reorientation

Building a model to reproduce the coupled effects of reorientation on 2D-anisotropy plots requires parameterizing the model using reorientational correlation functions. In doing so, we imbed the model with the reorientational information found in 2D-IR spectra. Additionally, we will evaluate this model using the current understanding of behavior inside a pair of limits.

A Gaussian joint probability density is used as a model lineshape. In the limit of inhomogenous broadening, a spectrum is approximately equal to the joint probability of finding a vibrator at ω_3 at t, given that it was at ω_1 at $t = 0$.[198] Many lineshape models generally assume Gaussian statistics, which explain 2D-IR spectra well. CO_2 in polymer and ionic liquid systems produce nearly Gaussian shaped peaks, so it is a reasonable approximation for this system, where it would not be for water (O-D, O-H) or amides (C=O).

The approximate two-dimensional joint probability density, $G_p(x, y)$, is a product of Gaussians in the diagonal and anti-diagonal directions,

$$G_p(x, y) = \frac{1}{2\pi\sqrt{\sigma_D^2}\sqrt{\sigma_A^2}} \times e^{-D^2/2\sigma_D^2} \times e^{-A^2/2\sigma_A^2}. \tag{38}$$

The diagonal and anti-diagonal distribution are calculated using

$$x = \omega_1 - \omega_0, y = \omega_3 - \omega_0 \tag{39}$$

$$D^2 = \frac{(x+y)^2}{2} \tag{40}$$

$$A^2 = \frac{(x-y)^2}{2} \tag{41}$$

$$\sigma_D^2 = \sigma^2(1 + C_p(t)^2) \tag{42}$$

$$\sigma_A^2 = \sigma^2(1 - C_p(t)^2), \tag{43}$$

where ω_0 is the center frequency of the peak, and x is a coordinate indicating the displacement in the x and y directions from the center frequency. D^2 and A^2 are a transformation of ω_1 and ω_3 to diagonal and anti-diagonal axes. σ is standard deviation of the frequency distribution (the full width at half max of the distribution divided by 2.355). σ_A and σ_D indicate the time dependent frequency distributions in the diagonal and anti-diagonal directions, scaled by $C_p(t)$, the PW-FFCF.

$C_p(t)$, the frequency fluctuation correlation function for the p polarization induces polarization- and time-dependence in the joint probability density. The PW-FFCF is calculated according to equation 35, where $F(t)$ is approximated as a constant value. The $R_p(t)$, polarization-weighted correlation functions are:

$$\begin{aligned} R_\parallel &= \frac{1}{175}\frac{28 + 215L_2^{\text{tot}}(t) + 72L_4^{\text{tot}}(t)}{1 + 0.8L_2^{\text{tot}}(t)}; \\ R_\perp &= \frac{1}{175}\frac{-14 + 155L_2^{\text{tot}}(t) - 36L_4^{\text{tot}}(t)}{1 - 0.4L_2^{\text{tot}}(t)}. \end{aligned} \tag{44}$$

$L_l^{\text{tot}}(t)$ are the total l-th order wobbling-in-a-cone correlation functions (equation 37).

The polarization-weighted Gaussian probability densities and the orientational amplitudes,

$$O_{\parallel} = \frac{1}{9}(1 + \frac{4}{5}L_2^{\text{tot}}(t));$$
$$O_{\perp} = \frac{1}{9}(1 - \frac{2}{5}L_2^{\text{tot}}(t)), \text{ [11]} \tag{45}$$

are both parameterized by the same orientational correlation functions. The goal of this is to generate a frequency distribution that reflects the discrepancies caused by orientational change in 2D-IR spectroscopy. The total signal,

$$S_p(\omega_1, t_2, \omega_3) = O_p(t_2)R_p(\omega_1, t_2, \omega_3)e^{-t_2/T_1} \tag{46}$$

is the product of the orientational amplitude, $O_p(t_2)$, the polarization-weighted correlation functions $R_p(\omega_1, t_2, \omega_3)$ and a vibrational energy relaxation exponential decay, characterized by time, T_1. Overlaying spectra for the experiment and Gaussian simulation emphasizes how RISD changes the shape of the spectra in the parallel and perpendicular conditions (figure 6.1). For CO_2 in the 50 vol% ion gel system, there are generally no meaningful differences in lineshape or correlation between the negative and positive absorption peaks (supporting information). The overlay is generated by plotting the main negative peak (centered at $\omega_3 = \omega_1 = \omega_0$) of the parallel spectra (blue), and then the perpendicular spectra (yellow) on the same axes. For clarity, only the most intense six contours are retained for the visualization.

The peak is centered at 2341 cm^{-1} in all eight plots (figure 6.1). The first plot in panel (a) shows the 0.2 ps spectra for the experimental data. Here, we can see that the blue peak (parallel) is more stretched along the diagonal than its yellow (perpendicular) counterpart. This trend continues, and is replicated in the simulated data in panel (b). The blue (parallel) peak is consistently larger along the diagonal, and the yellow (perpendicular) peak is broader in the anti-diagonal direction. This is a result of the faster spectral diffusion caused by RISD.

The 2D-anisotropy plots are calculated as described above (equation 34), and plotted on ω_1 and ω_3 axes, as a series of contour plots. This serves as a map of the anisotropy value for each frequency pair, across all of the t_2 population times in the data set. To evaluate the

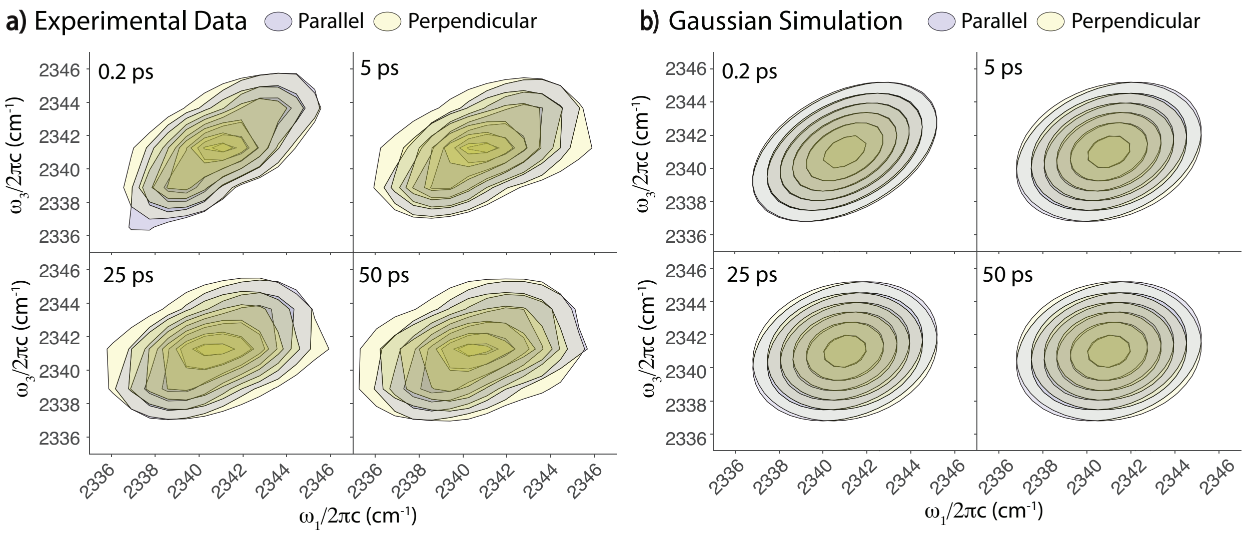

Figure 6.1: The frequency dependence of the anisotropy values tracks with the intensity variation of the parallel and perpendicular polarization conditions. a) In the experimental data, the yellow perpendicular spectra are consistently wider along the anti-diagonal direction, and become slightly larger in the diagonal direction as t_2 increases. b) The Gaussian simulation also shows this effect.

ability of the model to generate the 2D-anisotropy plots that we are interested in describing, we first tested a pair of the extremes.

When SSD is faster than RISD, the shape change associated with RISD is not measurable in the experiment. SSD ($F(t)$, equation 35) in this model is approximated by a constant. When SSD is much faster than RISD ($F(t) = 0$, $tau_r = 1$ ps, $\theta = 175°$), the 2D-anisotropy plots do not display a frequency dependence (figure 6.2a). The intensity of anisotropy is preserved as a result of the polarization-specific amplitudes, but the shape of spectra in both polarization conditions changes at the same rate.

When RISD is similar to or faster than SSD ($F(t) = 1$, $tau_r = 1$ ps, $\theta = 175°$), we see a saddle shape in the 2D-anistropy plot (figure 6.2b). Looking at the 1.0ps spectrum, when $t_2 = \tau_r$, from the center of the peak, $\omega_1 = \omega_3 = 2341\text{cm}^{-1}$, the anisotropy begins at 0.135 and increases along the diagonal to 0.173 at $\omega_1 = \omega_3 = 2343\text{cm}^{-1}$. In the anti-diagonal

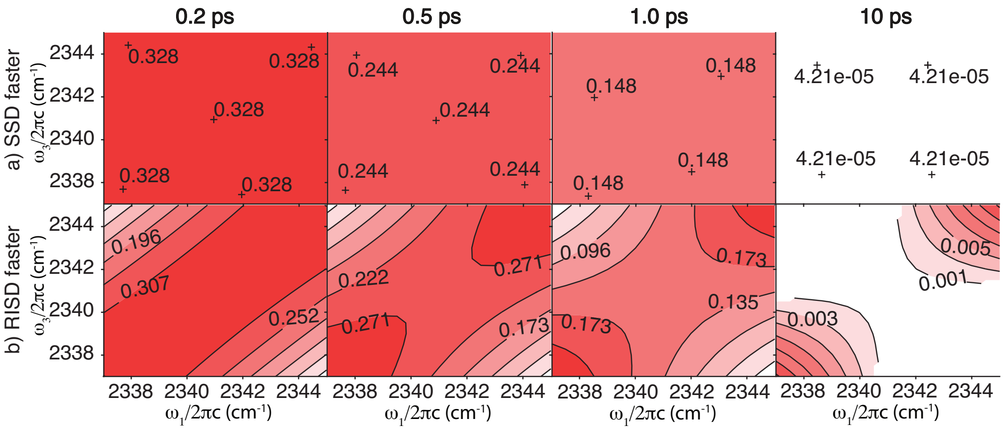

Figure 6.2: Time- and polarization-dependent Gaussian joint probability densities are calculated using a single cone model, with $\theta = 175°$ and $\tau_r = 1$ ps. a) With the SSD component set to a value much faster than τ_r, in this case, 0, we see that the anisotropy decays as a function of polarization amplitudes, but shows no frequency dependence. b) with SSD set to 1 (effectively constant), we see the saddle shape appear. When the waiting time is equal to the reorientation time (τ_r), the 2D-anisotropy increases out from center along the diagonal, and decreases out from center along the anti-diagonal. Beyond this, the anisotropy decays to zero along the anti-diagonal, and some intensity persists along the diagonal edges of the peak.

direction, the anisotropy decreases out from center. This occurs because RISD causes the spectral diffusion for perpendicular spectra to occur faster than the parallel (figure 6.1). In this regime, the perpendicular spectra have already begun to round out, which increases intensity long the anti-diagonal direction, and decreases along the diagonal. The anisotropy is inversely related to the intensity of the perpendicular spectra.

Frequency-resolved 2D-anisotropy provides information that is lost in the frequency-integrated anisotropy from pump-probe measurements. Integrating the spectra over the ω_1-axis generates the equivalent of a pump-probe measurement (figure 6.3a). The intensity of the band begins smaller for the perpendicular (yellow dashes) compared to the parallel spectra (blue line). Anisotropy was calculated using the intensity at three points (gray vertical lines) and the results were nearly identical.

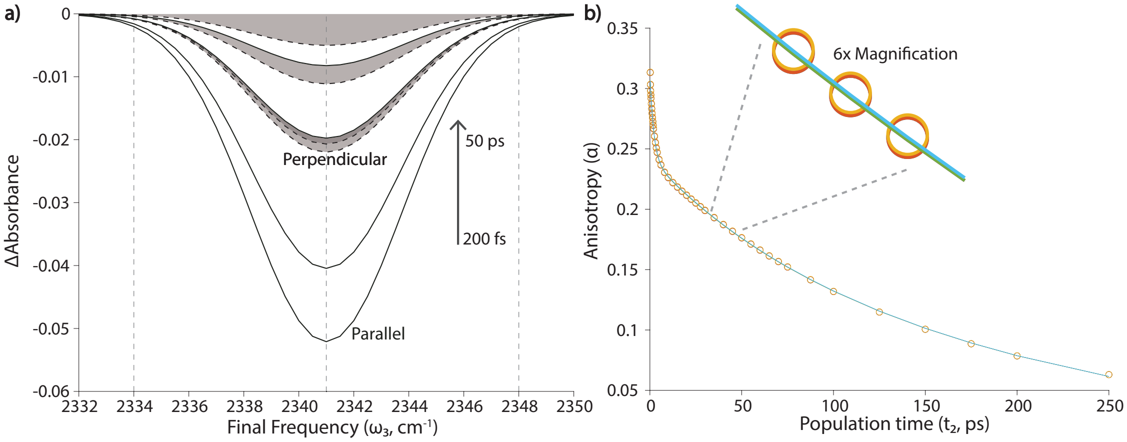

Figure 6.3: Integrating the Gaussian model across the ω_1-axis produces pump-probe-like spectra. a) The intensity of the parallel spectra (blue, solid) are larger than the perpendicular (yellow, dashed). Both decay as a function of time. Anisotropy is measured at three frequencies (vertical gray lines). b) Both the values (circles) and a triexponential fit (line) for the anisotropy are essentially indistinguishable between the three frequencies. Each fit result falls near the center of the 95% confidence interval of the other fits.

The anisotropy decay calculated from the pump-probe-like signal shows no frequency dependence (figure 6.3b). The anisotropy at the center of the band (2341 cm^{-1}) and the anisotropy on the wings overlap (figure 6.3b, inset). The wings of the spectra include both anti-diagonal (low anisotropy) and diagonal (high anisotropy) components. Integrating over the ω_1-axis causes the high- and low-anisotropy regions to cancel.

6.4.2 2D-IR and 2D-Anisotropy of CO$_2$ in Ion Gels

Now that we have explored the joint probability density model, and examined the behavior of 2D-anisotropy plots calculated using it, we are ready to examine the experimental 2D-IR spectra and 2D-anisotropy plots. Once we've fit the data to the wobbling-in-a-cone model, we use the fitting results to generate the probability distribution, and compare the resulting 2D-anisotropy plots between experiment and model.

CO_2 in the ion gel experiences slow spectral diffusion, evidenced by residual correlation even at long times (figure 6.4). At the earliest correlation time (t_2 = 0.2 ps), the peak shows a smaller inhomogenous (anti-diagonal) linewidth in the parallel spectrum compared to the perpendicular. The perpendicular peak appears to have a have a smaller homogeneous (diagonal) linewidth. This persists even as t_2 increases, until around 75 ps, at which point the spectra appear more similar in shape.

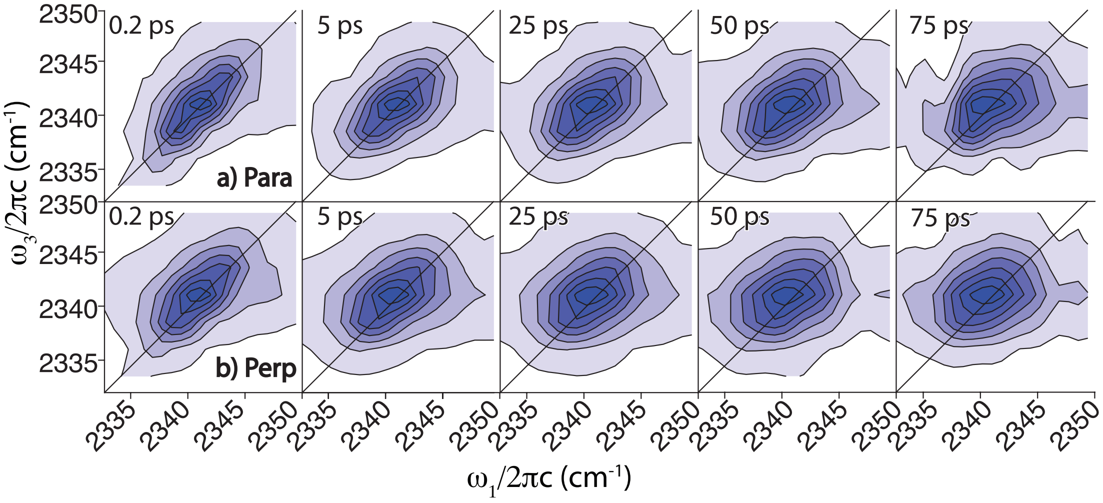

Figure 6.4: 2D-IR spectra of CO_2 are measured in both parallel and perpendicular polarization conditions. The parallel data begins with a smaller anti-diagonal linewidth compared to its perpendicular counterpart. Both experiments show spectral diffusion.

CLS is measured for both parallel and perpendicular spectra, and plotted as a function of increasing waiting time, t_2. The slope of a CLS is never exactly 1 as a result of motional narrowing, or motions too fast to be measured using 2D-IR. Spectral diffusion is faster for the perpendicular polarization condition relative to the parallel, which strongly indicates RISD.

The CLS values are fit to the wobbling-in-a-cone model with a second-order Stark shift approximation (equations 35,44).[103] The best-fit parameters for the three-cone model show three distinct timescales of relaxation (table 6.1).

Three time constants are extracted from the wobbling-in-a-cone model, each separated by an order of magnitude (table 6.1). The time constant for the first cone represents CO_2

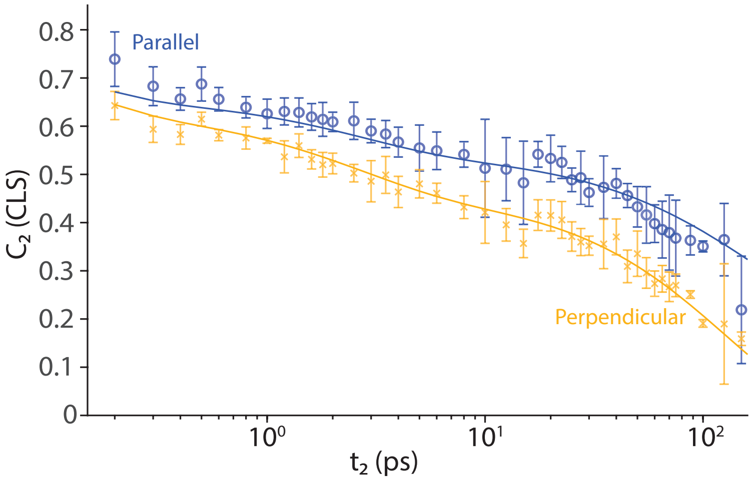

Figure 6.5: Center line slope decays for CO_2 in the ion gel fit to a wobbling-in-a-cone model with three cones. CLS from experimental spectra are represented by points, and the PW-FFCF are the lines. Error bars reflect uncertainty in the CLS measurement. Best fit values are recorded in table 6.1.

rattling in a fixed solvation shell. The second and third cones represent motions as the solvation shell reorganizes around CO_2.

Cone angles extracted from wobbling-in-a-cone models can be related to the size of the cavity the chromophore is contained in.[199] The cone half-angle for the inertial cone is 23.4°, which is statistically indistinguishable from the second cone, which has a cone half-angle of

Table 6.1: Wobbling-in-a-Cone Fit, 3 Cones, Experimental Data

Parameter	Value $\pm 2\sigma$
a ($F(t)$)	0.85 ± 0.05
τ_{r1} (ps)	0.34 ± 0.35
θ_1 (deg)	23.7 ± 3.0
τ_{r2} (ps)	9.3 ± 4.1
θ_2 (deg)	23.1 ± 2.6
τ_{r3} (ps)	105 ± 34
θ_3 (deg)	63 ± 24

23.1°. This indicates that the amount of rotational space accessible to the CO_2 molecule does not vary distinctly from the first cone to the second. The third cone has a much larger half angle of 63° and represents a more complete reorganization of the environment around CO_2, which reduces the degree to which the angular diffusion is restricted.

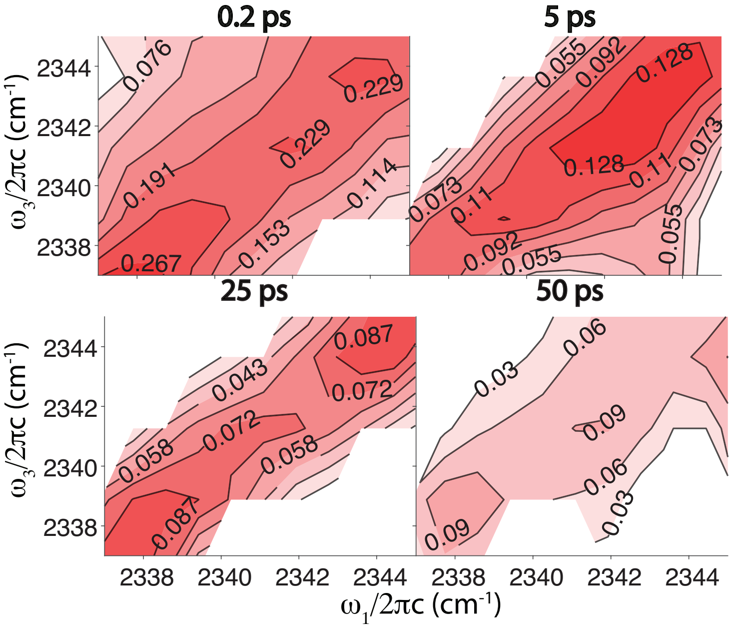

Figure 6.6: The anisotropy is frequency dependent. The anisotropy is highest along the diagonal and increases slightly in this direction while decreasing in the anti-diagonal direction. The anisotropy values also decrease over time, and approach zero by 50 ps.

Our extracted orientational correlation times agree with the results of measuring anisotropy of CO_2 in the IL-filled pore of a SILM. There, the three timescales were 0.6 ± 0.1, 8.2 ± 1.1, and 90 ± 2. The three timescales were rationalized as an inertial cone and two restricted angular diffusion cones.[86] Additionally, biexponential fits of CLS decays for three other 50 %bv [emim][Tf_2N] ion gels result in total correlation times ranging from 111-138 ps.[200] Likely the third timescale corresponds to a larger change in the structure around CO_2 than the first, which causes the longer timescale.

In addition to fitting the PW-FFCF, we calculate 2D-anisotropy plots of the experimental spectra (figure 6.6). These plots show a frequency dependence of the anisotropy. At the first time point, 0.2 ps, the initial anisotropy is 0.229 at the peak center. Along the diagonal

($\omega_1 = \omega_3$), the anisotropy seems to be increasing outward from the center frequency towards a maximum of 0.267. Moving in the anti-diagonal direction, the anisotropy decreases to a minimum of 0.076. The quantitative values (denoted as labeled contours) show the highest anisotropy along the diagonal, and in the first time point. The anisotropy then decreases over time as the sample relaxes towards an isotropic distribution.

Experimental evidence of frequency dependence in 2D-anisotropy plots has been noted in other systems.[134,195] Our Gaussian model suggests that this frequency dependence of anisotropy is the result of two factors. First, the SSD must be slower than the RISD components of spectral diffusion. Second, the RISD must sufficiently change the shape of the perpendicular spectra such that the the perpendicular signal intensity increases in the anti-diagonal direction and decreases along the diagonal. In order to investigate this, we generate the above Gaussian joint probability density using the PW-FFCFs extracted from the experimental spectrum (table 6.1, figure 6.7).

In addition to the wobbling-in-a-cone parameters, the Gaussian model is given inputs of a center frequency of 2341 cm^{-1}, σ of 2.75 cm^{-1}, the same list of t_2 waiting times used in experiment, and ω_1 and ω_3 ranges that corresponded with the ranges from experiment.

The resulting spectra follow approximately the same pattern as was seen in the experimental data. The peak width along the anti-diagonal is consistently larger for the perpendicular spectrum. Spectral diffusion causes the spectra to start stretched along the diagonal and then grow rounder over time. RISD results in the correlation of the perpendicular polarization condition decaying more rapidly than the parallel, as was measured in the experiment.

Calculating 2D-anisotropy plots for the Gaussian model results in the expected saddle shape (figure 6.8). Once again at short t_2 times, there is the expected highest anisotropy along the diagonal, and then a pattern of anisotropy values increasing outwards along the diagonal and decreasing in the anti-diagonal direction. The anisotropy values are larger than what was measured in the experiment, but follow the correct saddle-shape.

At early waiting times, the 2D-anisotropy is generally constant at the center of the CO_2 peak, but as the waiting time increases, the saddle shape appears. This analysis shows that the point in the 2D spectrum chosen to calculate the anisotropy will affect the measurement (figure 6.9). It also indicates that when measuring reorientational dynamics with pump-probe spectroscopy, information is lost as a result of averaging over ω_1.

Rotational correlation times, calculated as the decay of anisotropy, are often reported by fitting for a decay function generated by measuring anisotropy at a single point along the 2D-IR spectrum to a sum of exponential decay functions. These measurements average over the ω_1 axis, which eliminates the frequency-dependence information from the measurement.

The timescales that result from fitting anisotropy decay are sensitive to the frequency pair at which the anisotropy was measured. At the center of the peak, the correlation time is around 100 ps. Outward from center along the diagonal the anisotropy decay fits to a rotational correlation time of 220 ps. Towards the anti-diagonal edges, moving towards the regime of higher parallel signal intensity, we see that the anisotropy decays nearly an order of magnitude faster (∼20 ps). This, once more, is the result of RISD and the induced shape change in the perpendicular peak.

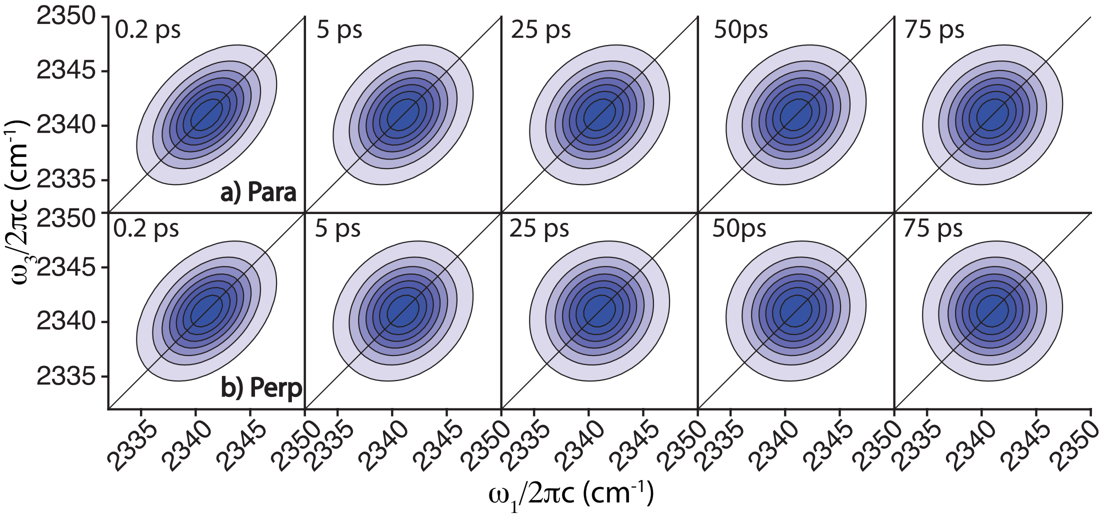

Figure 6.7: Simulated spectra exhibit the same RISD-induced behavior measured in the experimental data. The spectra are 2-dimensional Gaussian peaks with the same center frequency as CO_2 in the 50 %bv ion gel, and a σ value of 2.75.

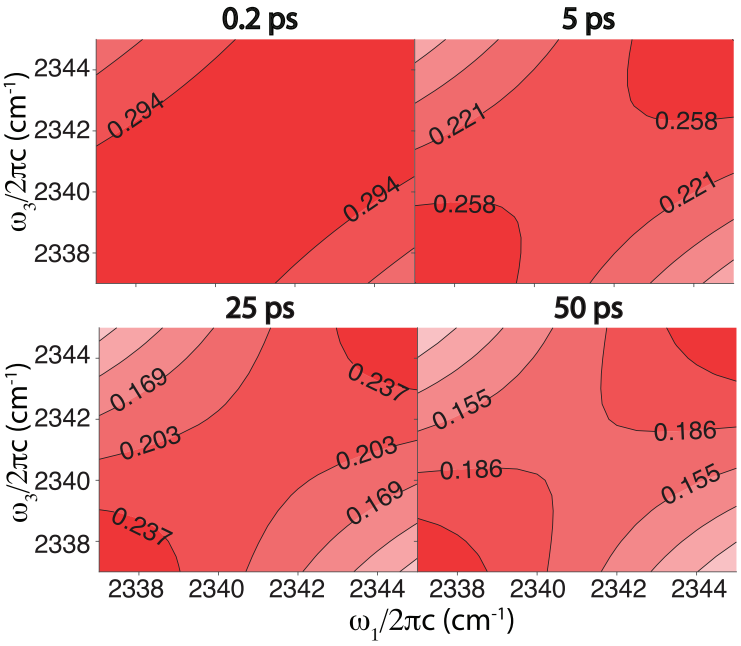

Figure 6.8: The simulated 2D-anisotropy is similar to the experimental 2D-anisotropy. It, too, has a frequency dependence, and it shows an increase in anisotropy out from center along the diagonal and a decrease along the anti-diagonal. The data is plotted with the same contour spacing as the experimental data (figure 6.6).

6.5 Conclusion

The frequency dependence of 2D-anisotropy, and the RISD-induced shape changes that cause it were identified and carefully characterized. We used polarization-weighted 2D-IR experiments to show that reorientation induced spectral diffusion causes the frequency dependence. A Gaussian model generated via time propagation of the a wobbling-in-a-cone model resulted in spectra that show the same effect seen in experimental data: an increase in anisotropy values out from center along the diagonal and a decrease in anisotropy values along the anti-diagonal.

This model, in the two extremes, replicates expected 2D-anisotropy plots (figure 6.2). When SSD is faster than RISD, the anisotropy loses frequency dependence, as the shape

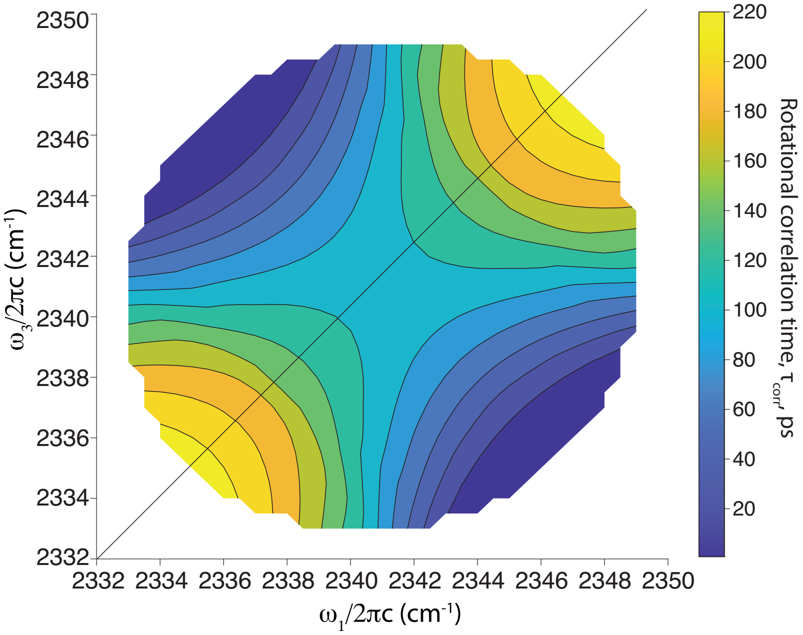

Figure 6.9: The total rotational correlation time (τ_{corr}) is calculated from a triexponential fit of the anisotropy decay. This value also shows frequency dependence. The center of the peak gives a rotational correlation time around 100 ps. Measuring this value along the diagonal gives the slowest correlation times (∼220 ps) whereas measuring at the anti-diagonal edges of the peak results in faster decay(∼20 ps).

change is predominantly caused by the SSD. When the SSD is suitably slow, the RISD dominates and the saddle shape appears, caused by the faster spectral diffusion of the perpendicular signal.

As shown in figure 6.1, the accelerated spectral diffusion of the perpendicular signal relative to the parallel signal results in the frequency patterning. Even at very early times the perpendicular spectra is broader in the anti-diagonal direction. Because anisotropy values are the normalized difference between perpendicular and parallel signal, this broadening (and consequently, shortening along the diagonal axis) impacts the frequency dependent values of the anisotropy.

There is also a frequency dependence of the resultant rotational correlation timescales (figure 6.9). Along the diagonal, where the overlap of parallel and perpendicular is most consistently, the overall timescale is the slowest. Measuring in areas along the anti-diagonal where perpendicular spectra dominate the anisotropy calculation produces rotational timescales nearly an order of magnitude faster, reinforcing the importance of both choosing and reporting the frequency at which anisotropy is calculated.

Polarization-selective 2D-IR spectroscopy offers information both about the frequency fluctuation dynamics of the system, and the rotational motion of chromophores. This technique has been used to study the reorientation of a variety of systems, including water, ethylammonium nitrate in water, and recently, even to probe the free volume of polymeric media.[134,195,199] As such, it was important to describe this phenomenon in careful detail.

6.6 Acknowledgements

The authors would like to acknowledge Thomas Gasmire, of the University of Pittsburgh Machine Shop for fabrication of sample cells. Additional thanks to the National Science Foundation (CHE-1954848, S. G.-R.), and the Science, Mathematics and Research for Transformation (SMART) Scholarship (C.J.K. 2016-present).

7.0 Intramolecular Vibrational Relaxation in Structurally Isomeric Polymers

The text in this chapter is adapted from a manuscript in preparation. The authors contribution to this work includes contributions to FTIR and 2D-IR experimental design, all data analysis and writing the text of the manuscript.

7.1 Chapter Summary

Ultrafast two-dimensional infrared (2D-IR) spectroscopy revealed slow, nearly identical dynamics but different intramolecular kinetics between structurally isomeric poly(vinyl acetate) (PVAc) and poly(methyl acrylate) (PMA). These polymers, despite their structural similarity, show different bulk CO_2 interaction behavior: PVAc is highly soluble in supercritical CO_2 but the same is not true of PMA. Linear and 2D-IR spectroscopy of CO_2 in these materials were measured. Linear IR spectra show similar center frequencies, but an increased FWHM in the PMA sample. Center line slope fitting of 2D-IR spectra revealed similar dynamic timescales, but response function fitting extracted slower intramolecular kinetics and a longer-lived hot ground state in PMA compared to PVAc. We hypothesize that the bulk-CO_2-interaction differences between the isomers to most likely result from geometric and steric effects interactions of their variable side chains with CO_2.

7.2 Introduction

Rising carbon dioxide (CO_2) levels are an ongoing environmental concern. One method for reducing the impact of the greenhouse effect is post-combustion carbon capture. Many materials have been investigated for this task; amines[8,9], ionic liquids(ILs)[3,37–40], metal-organic frameworks (MOFs)[75–80], polymers,[57,66,67] and various composite materials.[5,65,73,92,93] Polymer-based separations methods have the advantage of lower capital and processing costs, simpler operation, smaller footprints and better energy efficiency, but have an ongoing disadvantage caused by the trade-off between permeability and selectivity.[69,81,84]

The permeability and selectivity of a membrane are coupled characteristic quantities. The permeability, or how easily a given molecule is able to flow through the membrane, is related to the selectivity by the equation:

$$\alpha_{A/B} = \frac{P_A}{P_B}, \tag{47}$$

where $\alpha_{A/B}$ is the selectivity for gas A over gas B, and P_A and P_B are the permeability of gas A and B respectively.[68] An approach to investigating the nature of CO_2 permeability and selectivity is to examine polymers on a molecular level. CO_2 vibrations occur on femto- to picosecond timescales, and angstrom length scales. Ultrafast two-dimensional infrared (2D-IR) spectroscopy has the temporal and spatial resolution to probe these motions, which report on their surroundings.[11,17,28] Investigations of this type offer insight into the relationship between CO_2 and its local environment.

Poly (vinyl acetate) (PVAc) and poly (methyl acrylate) (PMA) are structurally isomeric oxygenated-hydrocarbon polymers. Structurally, they differ by the location of the ether moiety on the pendant groups; it is terminal in PMA, and directly connected to the backbone for PVAc. To emphasize how similar these polymers are on a macroscopic level, despite the small entropy of mixing that is common to polymers, they are miscible at all compositions.[201]

For all their structural and chemical similarity, PVAc and PMA differ remarkably in their interactions with CO_2. PVAc is recognized as one of the most CO_2-soluble non-fluorous oxygenated-hydrocarbon polymer.[202,203] In supercritical CO_2, PVAc is soluble at 298K even up to very high molecular weights, unlike PMA, which requires nearly five times the pressure to dissolve a molecule with an order of magnitude fewer repeat units.[204] This discrepancy was explained as an increased CO_2-philicity of the acetate group compared to the acrylate group, and a higher degree of geometric freedom for the carbonyl group of PVAc. The ether moiety allows the pendant group to rotate more freely, making the carbonyl more accessible to CO_2 in PVAc compared to PMA.[205,206]

Two-dimensional infrared (2D-IR) spectroscopy has previously been used to investigate molecular-scale interactions between CO_2 and a variety of carbon capture candidate materials.[17,47,48,207–209] 2D-IR experiments are a powerful analytical tool, capable of revealing frequency fluctuation dynamics, rotational dynamics,and intramolecular vibrational relaxation (IVR) of a chromophore.[11,146,171] There is a precedent for using IR spectroscopy to probe the relationship between CO_2 and polymeric media.[87,172,187] CO_2's ν_3 antisymmetric stretch is a strong IR chromophore ($\epsilon = \sim 1000\ \mathrm{M^{-1}cm^{-1}}$) that absorbs in a spectrally clear region in many systems ($\sim 2340\ \mathrm{cm^{-1}}$).

2D-IR spectroscopy probes the coupled dynamics of CO_2 and it's environment. Spectra are displayed as contour plots, where each axis displays the spread of frequencies reported by the chromophore at that time. These two measurements (initial, and final) are separated by a variable time, t_2, during which time the system is not perturbed. At small t_2 times, the initial and final states of the system are very similar, resulting in a peak with high frequency correlation. As t_2 increases, the peak tends to lose this correlation, and this randomization causes a change in shape, from stretched along the diagonal to rounded. This process is called spectral diffusion. To extract frequency-fluctuation correlation functions (FFCF), the center line slope (CLS) method is used to analyze this change in the shape of the 2D-IR spectra.[98]

Spectroscopy of the antisymmetric stretch of CO_2 is complicated by the presence of a thermally populated shoulder peak. This peak is the result of some portion of the CO_2 obtaining a single quantum of bend energy (ν_2) at room temperature, usually with an intensity of around 7% of the main band.[17] This leads to a complicated pattern of both diagonal and cross-peaks, which result from between-manifolds exchange. These IVR processes are related to the variation in the surroundings by the same concepts as frequency fluctuation, and as such add to the information content of the spectra.

In order to extract quantitative information about the intramolecular exchange of population during the waiting time, t_2, Kelsheimer and Garrett-Roe developed a model of kinetic flow between the various vibrational states of CO_2 (figure7.1).[187] The vibrational energy states of the system are most completely described by $|\nu_1\nu_2^l\nu_3\rangle$, where the symmetric stretch quantum number is ν_1; the bend quantum number is ν_2; the vibrational angular momentum

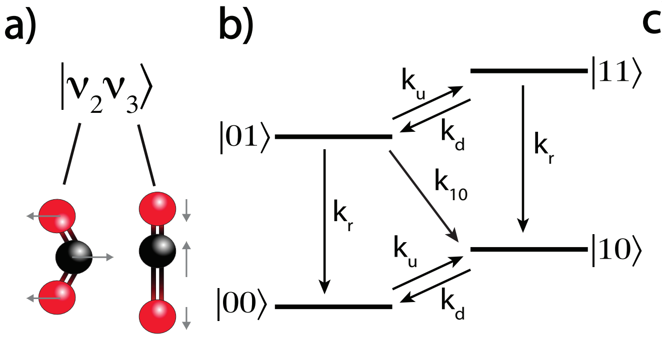

c)

$$\begin{array}{c|cccc} & |00\rangle & |01\rangle & |10\rangle & |11\rangle \\ \hline |00\rangle & -k_u & k_r & k_d & 0 \\ |01\rangle & 0 & -k_r - k_u - k_{10} & 0 & k_d \\ |10\rangle & k_u & k_{10} & -k_d & k_r \\ |11\rangle & 0 & k_u & 0 & -k_r - k_d \end{array}$$

Figure 7.1: CO_2 has a number of IVR pathways. a) In the region of interest, the two relevant vibrational modes are the bending mode, ν_2 and the antisymmetric stretch, ν_3. b) There are four kinetic terms that label kinetic pathways in CO_2, including equilibration terms, k_u and k_d, the switch term, k_{10}, and the direct relaxation rate, k_r. c) To fully describe the kinetic exchange within CO_2, a kinetic matrix is utilized to track the flow of energy between states. Diagonalizing this matrix produces the time-dependent kinetic functions that can be applied to response functions.

is l; and the antisymmetric stretch is ν_3. The symmetric stretch and the vibrational angular momentum play no direct role in this discussion, so we suppress their labels, for example, $|\nu_1\nu_2^l\nu_3\rangle \equiv |\nu_2\nu_3\rangle$ and the vibrational ground state is $|0\,0^0\,0\rangle \equiv |0\,0\rangle$ (figure 7.1a).

At the beginning of t_2, the pumped CO_2 molecules are in one of four states: $|0\,0\rangle$, $|1\,0\rangle$, $|0\,1\rangle$, or $|1\,1\rangle$. During t_2, the energy can transition spontaneously through several pathways (figure 7.1b). Population can transition between the manifolds by either gaining or losing a quantum of bend. The rate of exchange through these pathways are called k_u and k_d, and are treated as equivalent, as the energy gap between the excited states is approximately the same as the energy gap between the ground states. Additionally, energy can transition from the excited states ($|0\,1\rangle$, $|1\,1\rangle$) directly back down to the ground states ($|0\,0\rangle$, $|1\,0\rangle$, respectively). The rate of this process is called k_r.

The rate of transition between the excited antisymmetric stretch state ($|0\,1\rangle$) to the one-quantum-of-bend (1qb) ground state ($|1\,0\rangle$) is called k_{10}. This pathway was identified when its rate appeared to be accelerated in polymeric media. In a poly(ethylene glycol) diacrylate gel, the increased rate of this switching process relative to the equilibration terms lead to the formation of a hot ground state: the accumulation of population in a state that is not the total ground state.[187] This feature is also seen in the spectra of CO_2 in PVAc and PMA.

To track these kinetic processes, these rate constants were organized into a matrix that relates the initial and final vibrational states (figure 7.1c). Diagonalizing this matrix, and applying the generated equations to the appropriate response functions allows for the calculation of spectra that include these transitions. These calculated spectra can then be fit to the experimental spectra, which allows for the best-fit values to be obtained.

2D-IR spectroscopy provides molecular-scale insight into the interactions of a chromophore with its environment. By measuring 2D-IR of CO_2 in PVAc and PMA, we probe differences in the vibrational frequency dynamics and intramolecular kinetics of the chromophore and it's environment. Our goal is to investigate the molecular-scale differences between the structural isomers, with the hope of explaining the variation in their bulk interaction with supercritical CO_2.

In this work, we measure 2D-IR spectra of CO_2 dissolved in films (< 100 µm) of high molecular weight (> 40 kDa) PMA and PVAc. We extract frequency fluctuation dynamics and intramolecular kinetics observed between the antisymmetric stretch and its thermally excited shoulder.[17,46,187] While frequency dynamics occur on the order of around 1 ns, intramolecular kinetics occur on much faster timescales. An investigation of both the slow frequency dynamics and accelerated intramolecular kinetics suggests differences in the immediate molecular environment of CO_2 between the polymers, despite the structural similarities.

7.3 Methods

7.3.1 Materials

A solution of 40 wt% poly(methyl acrylate) (PMA) in toluene, and poly(vinyl acetate) (PVAc) beads were obtained from Sigma Aldrich (figure 7.2a,b). Bone dry CO_2 (99.8 % purity) was obtained from Matheson TRIGAS.

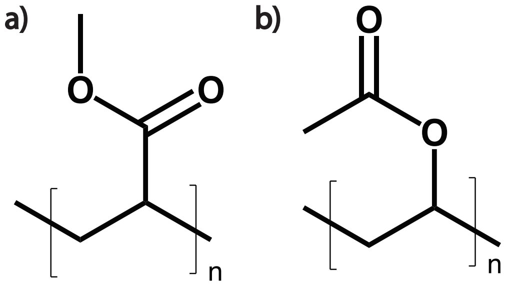

Figure 7.2: PMA and PVAc are structural isomers. A) Poly(methyl acrylate) (PMA, M_n = 40 kDa, n ∼ 500) B) Poly(vinyl acetate) (PVAc, M_n = 100 kDa, n ∼ 1250).

7.3.2 Sample Preparation

To prepare a sample of PVAc for experiment, the polymer beads from the manufacturer were heated to 60°C, pressed between two glass plates, then cut down to size. The optimal polymer sample size for this study was found to be ∼1.5 mg for a 100 µm film. For PMA, the polymer arrived dissolved in toluene. The mixture was vacuum-dried and then ∼1.5 mg of the dried sample was heated at 195°C for seven minutes to remove any remaining toluene. The final heating for PMA occurred during sample preparation for experiment.

The general process of making the polymer films is the same for both PVAc and PMA. First, ∼1.5 mg of polymer is placed in the center of a CaF_2 window on a heating mantle. This window is drilled to allow CO_2 flow into the sample cell. The mantle is heated to 195°C for PVAc and 165°C for PMA in order to melt the polymers and generate an optically clear film. A second CaF_2 window, separated from the first by a 100 µm polytetrafluroethylene

(PTFE) spacer, is used to press the film to the desired depth. The sample is then removed from the heating mantle and left to cool to room temperature.

Once the sample is cool, it is sealed into a gas-flow brass sample cell and placed into a N_2 purged Fourier transform infrared spectrometer (FTIR) for measurement. To infuse CO_2, gas lines are attached to the cell, allowing a small pressure (< 10 kPa, per tank regulator) of CO_2 to flow into the airtight cell, and exhaust via exit tubing to atmosphere. This CO_2 absorption is measured at intervals by FTIR spectroscopy.

7.3.3 Spectroscopy

FTIR spectra are taken on a N_2-purged Thermo Fischer Nicolet FTIR spectrometer, taking 4-8 scans with 0.5 cm^{-1} resolution. 2D-IR spectra are collected utilizing a Ti:Sapphire chirped pulse amplifier laser system ($\lambda = 805$ nm, 5 kHz repetition rate, 120 fs pulse duration) (Coherent Vitesse/Coherent Legend Elite). The mid-IR pulses are generated using a home-built optical parametric amplifier (OPA), designed to suppress noise.[104] After the OPA, the spectral bandwidth is around ~200 cm^{-1}. The pulses are tuned to 4.3 µm , with energy entering the 2D-IR spectrometer of ~2.2 µJ.

The 2D spectrometer employs a pump-probe geometry.[150] A Mach-Zender interferometer controls the first delay time, and a translation stage controls the second. The signal field is emitted along the path of the probe pulse. The signal, ω_3, is diffracted across a 150 l/mm grating onto a liquid N_2-cooled 2×32 channel mercury cadmium telluride detector. Signals are gated, integrated, digitized, and transmitted to the lab computer using the Femtosecond Pulse Acquisition System (Infrared Systems Development Corp.).

7.3.4 Differential Scanning Calorimetry

Thermograms were recorded on a Perkin Elmer DSC 4000. PMA and PVAc measurements were collected under a nitrogen purge of 20.0 mL/min. A 9.2 mg sample of PVAc was heated from -30°C to 200°C at 5.00°C/min. A 13.10 mg sample of PMA was heated from -40°C to 170°C at a rate of 3.00°C/min.

7.3.5 Analysis and Spectral Simulation

All analysis is performed using MATLAB software. Peak shape change is quantified using the center line slope method.[98] The error bars are calculated via propagation of error through peak maxima determination and the resulting curve is fit to a single exponential model:

$$C(t_2) = Ae^{-t_2/\tau} \tag{48}$$

where A is the initial correlation, and τ is the structural reorganization timescale.

Spectra are simulated using the global fit methodology explained by Kelsheimer and Garrett-Roe.[187]. Nonlinear least squares regression is used to minimize differences between experimental and simulated spectra based on adjustment of free parameters. Error bars are the 95% confidence intervals determined using a bootstrapping process ($n_{\text{boot}} = 100$).[106]

7.4 Data and Results

7.4.1 DSC

Analysis of differential scanning calorimetry (DSC) measurements produces glass transition temperatures (T_{g}) that agree with literature values. Many polymer properties are often linked to T_{g} values. DSC of polymers processed with the same heating and cooling procedures as the spectroscopy samples gave T_{g} of 42°C for PVAc and 17°C for PMA. Prior measurements of similar molecular weight PVAc and PMA produced glass transition temperature values that agree well with the measured values.[203,210]

Dynamics in polymer systems are often reported as a function of T/T_{g}. The ratio for both samples is similar and close to 1, with $T/T_{\text{g}} = 0.93$ for PVAc and $T/T_{\text{g}} = 1.01$ for PMA. As both are close to 1, dynamics here are reported without normalizing for the glass transition temperature.

DSC was performed to ensure that the heating and cooling process required to generate thin, low-scattering films did not severely degrade or decompose the polymer. Both polymers had cited degradation temperatures of well above those used in sample prepara-

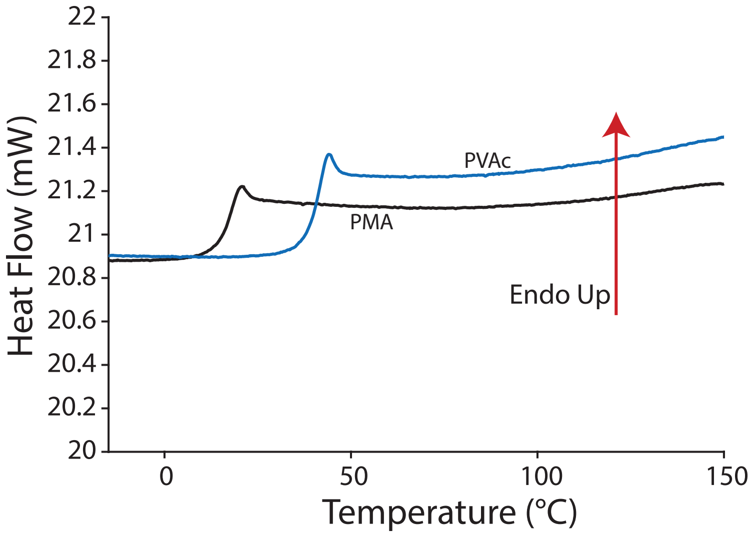

Figure 7.3: DSC was performed on PVAc and PMA samples treated identically to the spectroscopy samples. The DSC of these samples agreed with what was expected in the literature, showing glass transition curves at 42°C for PVAc and 17°C for PMA.

tion. Nuclear Magnetic Resonance measurements also verified sample integrity and ruled out decomposition.

7.4.2 Linear IR Spectroscopy

The antisymmetric stretch mode (ast) of CO_2 dissolved in both PMA and PVAc absorbs near 2340 cm^{-1} (ω_{ast}) Also present is the 1qb shoulder peak, shifted around 12 cm^{-1} lower (ω_{1qb}). The center frequency of the peaks differs by only half a wavenumber, with the PMA center frequency falling at 2339.3 cm^{-1} and the PVAc at 2339.8 cm^{-1}, measured via Voigt fitting. These center frequencies are relatively low for CO_2, which has a center frequency of 2349 cm^{-1} in the gas phase.[143] This agrees with prior work, which reported lower center frequencies for polymeric samples.[187]

The full width at half maximum (FWHM) is $\sim$2 cm^{-1} broader in PMA compared to PVAc, 6.7 and 4.8 cm^{-1} respectively. This is likely due to the state of the polymer at room temperature. PVAc is glassy (below T_g), and PMA is rubbery (above T_g). The rubbery

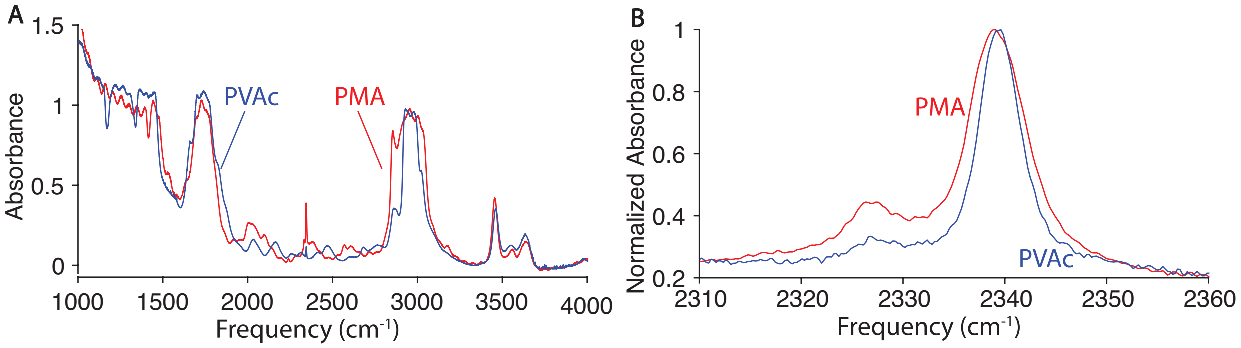

Figure 7.4: The antisymmetric stretch (ν_3) mode of CO_2 in both samples falls around 2340 cm^{-1}. a) Full range spectra of PMA and PVAc films shows no competing peaks in the region of the spectra around the nu_3 band. The concentration of CO_2 differs between the two samples. b) Normalized CO_2 absorption peaks, and the one-bend-quantum shoulder peak.

polymer likely offer CO_2 a broader range of possible frequency states compared to the glassy polymer. There appears to be more population in the shoulder band in PMA compared to PVAc.

7.4.3 2D-IR Spectroscopy

Experimental 2D-IR spectra of CO_2 in PMA and PVAc produces the characteristic pattern of peaks in eight spectral regions (figure 7.5, first row). At early t_2 waiting times (0.2 ps), there are four peaks: two blue (negative) and two red (positive). The main bands, centered at ~ 2339 cm^{-1} on the ω_3 axis correspond to the pure antisymmetric stretching modes ($\nu_2 = 0$). The smaller peaks, shifted about ~12 cm^{-1} lower correspond to the shoulder band: an antisymmetric stretching excitation, but with a quantum of bend present ($\nu_2 = 1$).[17] At longer t_2 times, population exchanges between the manifolds during t_2 (figure 7.1) and cross-peaks appear.

Transitions across the manifolds from the total ground state ($|0\,0\rangle$) to the 1qb ground state ($|1\,0\rangle$) during the t_2 waiting time generates two pairs of cross-peaks, one red and one

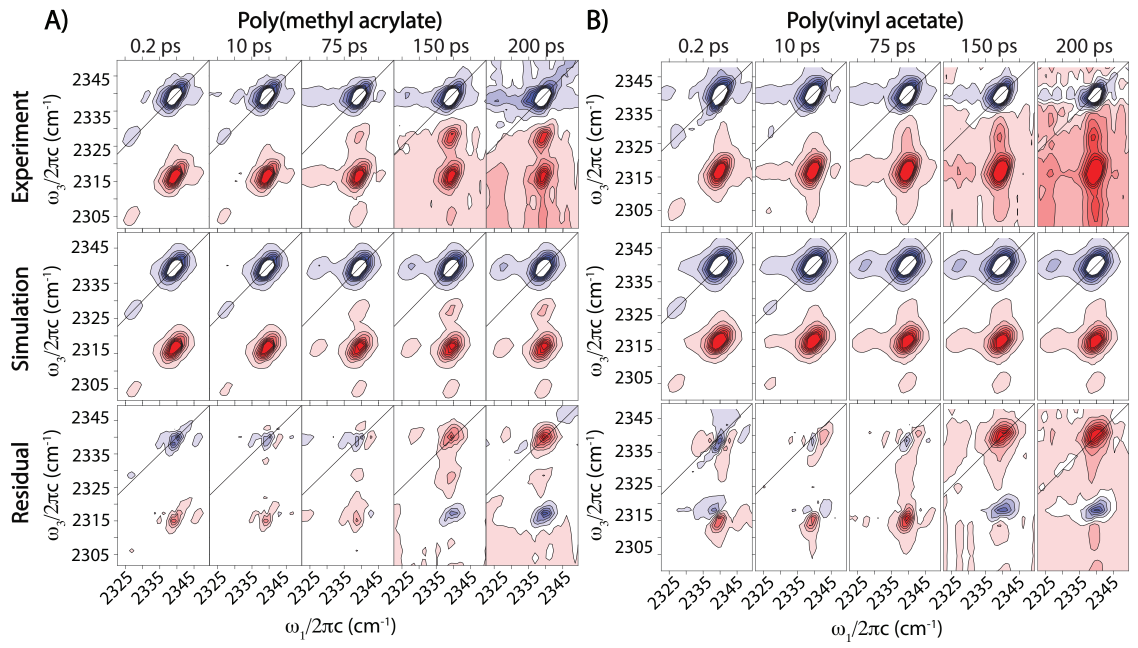

Figure 7.5: 2D-IR spectra of CO_2 was measured and simulated in both PMA and PVAc. Spectra contain the peaks in the eight predicted spectral regions, including cross-peaks that result from IVR processes. The spectra appear stretched along the diagonal throughout the experiment, indicating slow spectral diffusion. These observations are reproduced in simulated spectra. Residuals, which are plotted with the same intensity axis as the experiment and simulation, appear to result from lineshape variation and low signal-to-noise ratios in longer t_2 samples.

blue. In these spectra, both red cross-peaks are visible, but only the blue cross-peak in the upper-left most region of the spectra is visible. For CO_2, the crossover pathway, k_{10}, generates a red peak at the same location as one of the blue cross-peaks (figure 7.1).

The appearance of the red peak at $\omega_1 = \omega_{ast}$, $\omega_3 = \omega_{1qb}$ depends on relative intensities of the crossover rate, k_{10}, and the upward equlibration rate, k_u.[187] In some solvents, such as ionic liquids, the rates can be similar, which leads to a net zero intensity in this region. Polymeric media generally show slow equilibration between the ast and 1qb states.[187] This slow exchange allows for an increased intensity of the positive, hot ground state pathway at this position.

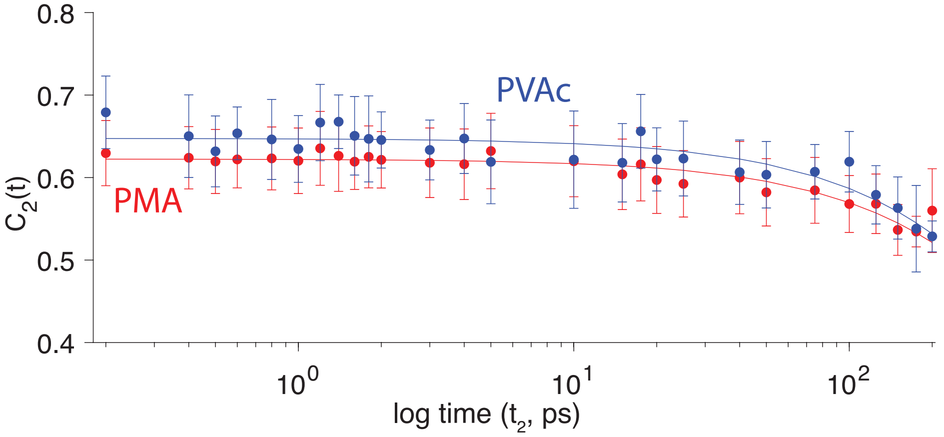

Figure 7.6: CLS fitting revealed dynamics on a nanosecond time scale. The data is displayed with a logarithmic x-axis for easier visualization.

Spectral diffusion is slow in both samples. When fast, spectral diffusion results in a rounding of the peak over time, as the final frequencies randomize and lose memory of their initial values. For both PVAc and PMA, at all t_2 values, the main bands appear narrow and stretched along the diagonal, indicating a high degree of correlation between the initial and final frequency distributions even at long t_2 times.

Spectral diffusion is quantified using CLS, which reports decay on the order of ∼1000 ps. Plotted on a logarithmic time axis, frequency fluctuation correlation functions (FFCF) change minimally until after 100 ps (figure 7.6). Over the course of the 200 ps, we only measure a loss of around ∼ 10 % correlation. The high correlation at the end of the experiment indicates that frequency fluctuation captured is only the beginning of the spectral diffusion process.

Fitting the CLS to a single exponential decay (equation 48) extracts consistently higher initial correlation value in the PVAc sample. This higher correlation persists until correlation values begin to decrease beyond 100 ps (figure 7.6, table 7.1). The correlation times, τ are not significantly different from each other, indicating that the timescale of reorganization for CO_2 and its surroundings is nearly identical between the polymers.

Slow dynamics were expected in such high-molecular-weight polymers, though we did

Table 7.1: CLS Fits

Sample	A	τ (ps)
PMA	0.648±0.008	1020±140
PVAc	0.630±0.004	1070±120

predict slightly faster spectral diffusion in PMA, the rubbery polymer. The dynamics, however, did not show the predicted variation. The only variation between them was in overall correlation amplitude, which was slightly increased in the PVAc sample. The higher amplitude is likely explained by the same effect that causes the smaller FWHM measured in the FTIR spectrum: the glassy polymer offers fewer frequency states to sample. Both polymers, however, are atactic; their side chains are randomly oriented and therefore they do not form uniform crystal domains, as confirmed by a lack of crystallization peak in the DSC (figure 7.3). This, combined with generally slow diffusion of polymer chains relative to the small-molecule chromophore indicates a lack of structural relaxation and therefore a lack of significant frequency-space fluctuations, even in PMA.

Extracting quantitative values for the intramolecular kinetics required response-function based global fitting. The spectra are simulated by setting the lineshape function time constant, τ to a very long time ($\sim$ 1 ns) as extracted from CLS analysis. This was left as a free parameter; however the fit was not sensitive to its value. The dephasing time (T_2) and frequency distribution (Δ) were free parameters, along with the kinetic rate constants (figure 7.1b,c).

Table 7.2: Global Fit Parameters

Sample	Kinetic Coefficients				Lineshape Parameters	
	k_u ns^{-1}	k_d ns^{-1}	k_{10} ns^{-1}	k_r ns^{-1}	Δ (cm^{-1})	T_2
PMA	2.2 ± 0.3	26 ± 3	9 ± 2	6 ± 2	1.55±0.03	6.5±0.2
PVAc	4 ± 1	47 ± 9	12 ± 3	3 ± 3	1.56±0.05	4.4±0.1

The resulting simulated spectra reproduced the experimental spectra well (figure 7.5, second row).The simulated spectra for both experiments begin with the two expected pairs of CO_2 peaks, and form cross-peaks as a result of kinetic exchange between states (figure 7.1). Both sets of simulated spectra also reproduce the growth of the red, hot ground state peak. Residuals result mostly from lineshape discrepancies and low signal-to-noise ratios at long t_2 times (figure 7.5, third row).

The kinetic best fit values show distinct differences between the coefficients for each sample. Population exchange between the ast and 1qb manifolds, governed by k_u and k_d, occurs twice as fast in PVAc relative to PMA. In PMA, the k_r rate is faster, however, this pathway in conjunction with k_d delivers population to the total ground state, so the increased k_d value for PVAc likely accounts for the slower k_r. Notably, all kinetic processes occur an order of magnitude faster than spectral diffusion.

The crossover term, k_{10}, is approximately 1.5 times faster in PVAc than in PMA. Prior work, however, has determined that examining the raw value of the kinetic coefficient for this process does not adequately predict the intensity of the peak at $\omega_1 = \omega_{ast}$, $\omega_3 = \omega_{1qb}$ in CO_2 spectra.[187] The appearance of this peak depends on the competition between the k_u, which forms the blue cross-peak, and k_{10}, which forms the red hot ground state peak.

The red hot ground state peak becomes more prevalent as a result of slow population exchange (k_u/k_d) and fast transitions between ast and 1qb manifolds (k_{10}) (figure 7.7). PMA shows a higher long-term intensity of the hot ground state peak, while PVAc shows an earlier appearance, likely due to its faster k_{10} rate. Additionally, even at very early times, there is already some positive intensity in this region for PVAc, though it is difficult to determine if this is genuine signal, or background absorption (figure 7.7d).

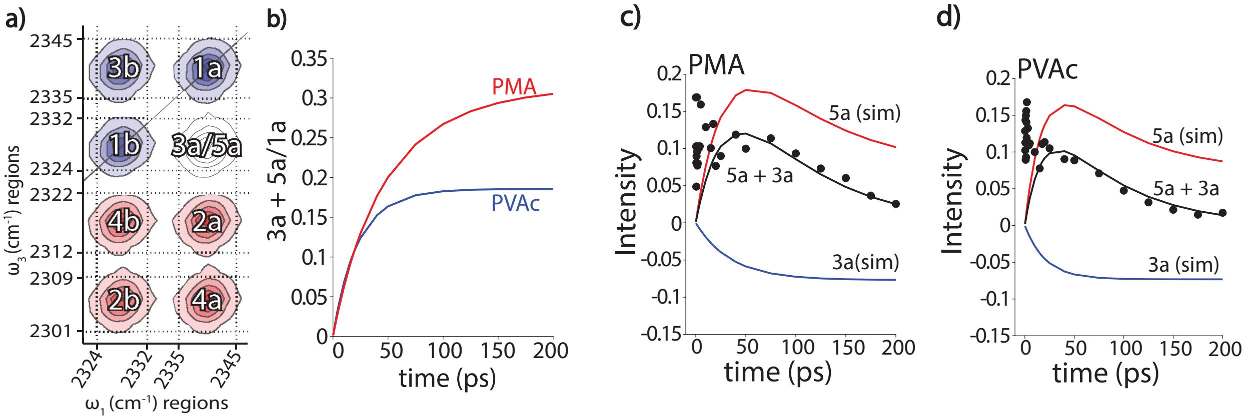

Figure 7.7: The CO_2 hot ground state persists longer and at a higher intensity in PMA compared to PVAc. a) The eight spectral regions of CO_2 contain nine independent peaks. Peaks 1a,b and 2a,b are for the main ast and 1qb bands. Peaks 3a,b and 4a,b are cross-peaks caused by population exchange between the ast and 1qb states. Peak 5a is the hot ground state caused by the relaxation of energy from the excited ast state to the ground 1qb state.[187] b) Intensity differences between the hot ground state peaks in PVAc and PMA are most obvious after normalization with the intensity of the main band peak (1a). c,d) Kinetic predictions for peak intensity in the 3a/5a region agree with the shape of experimental data.

Overlaying intensities of the peaks in each of the spectral regions for simulation and experiment is one method of confirming that the simulated data (lines) reports reasonable values for the experiment (points). For both samples, the time-dependent decay of main bands (b) and the shoulder bands (c), both agree well with the experiment (figure 7.8). In both samples, as a result of low signal-to-noise and some background absorption, the intensities of simulated cross-peaks do not agree exactly with the experiment. The shape of the curves for the simulated data track with the shape of the experimental data.

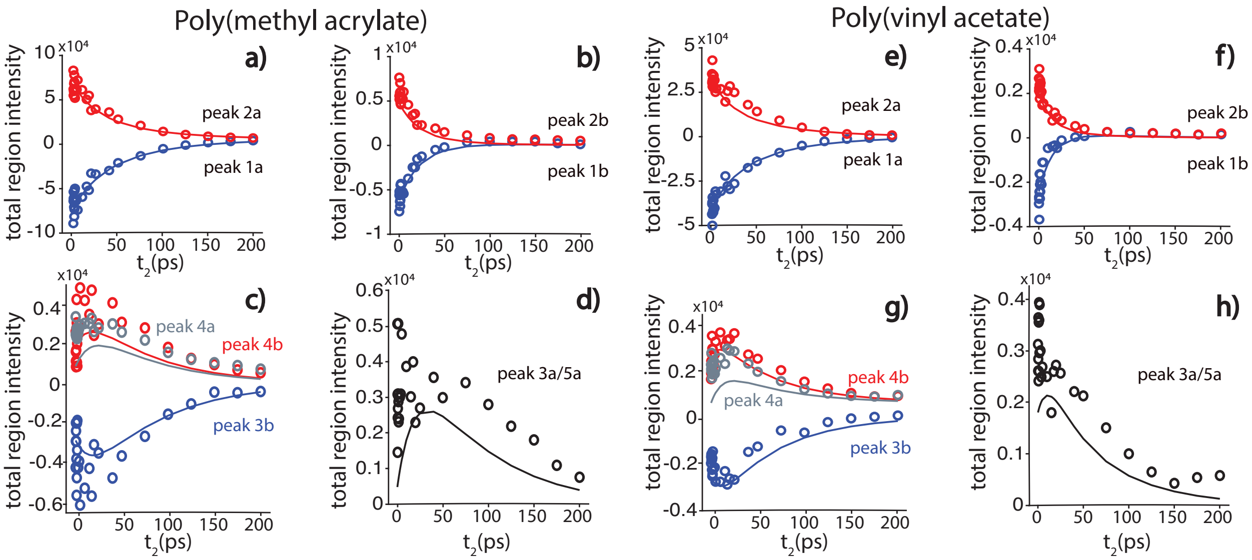

Figure 7.8: Summation intensities for each of the eight spectral regions of CO_2 in PMA and PVAc. a,b and e,f) Main spectral bands, peaks 1a, 2a, and shoulder bands, peaks 1b and 2b both show good agreement between simulation and experiment. c,g) Agreement for the cross-peaks is obscured slightly by noise, but follows appropriate trends. d) For PMA, the expected hot ground state competition behavior is seen in the peak 3a/5a region. h) The hot ground state region in PVAc appears populated even at very early times.

7.5 Discussion

The structural similarity and functional differences between PVAc and PMA have been reported for many years.[201,210] This work has identified that the frequency fluctuation dynamics are similarly slow (~ 1 ns) for CO_2 in the two polymers. The intramolecular kinetics, however, differ between the two considerably. PVAc experiences a faster exchange between the ast and 1qb manifolds and a much earlier hot ground state peak intensity. PMA exchanges more slowly, and the hot ground state peak persists longer as a result.

2D-IR reports coupled dynamics of both the chromophore and its environment. As such, properties of the bulk system must be considered. PMA, the shorter of the two polymers, is composed of ~ 500 repeat units, making the contribution of the end groups to the overall structure very small ($< 0.5\%$). This places both polymers well into the high-molecular-weight regime. This reduces the probability that end-group effects or molecular-weight dependent effects are causing the variation observed.

Because both PMA and PVAc are atactic polymers, they do not form crystalline structures. No crystallization was seen in our DSC (figure 7.3) or reported in the literature. It is possible that the packing or density of the amorphous phase could be playing a role. Neutron or X-Ray scattering data would be able to better determine this effect. Given the very small length-scales that contribute to frequency fluctuation, for a small molecule, like CO_2, effects of phase density are unlikely to play a major role.

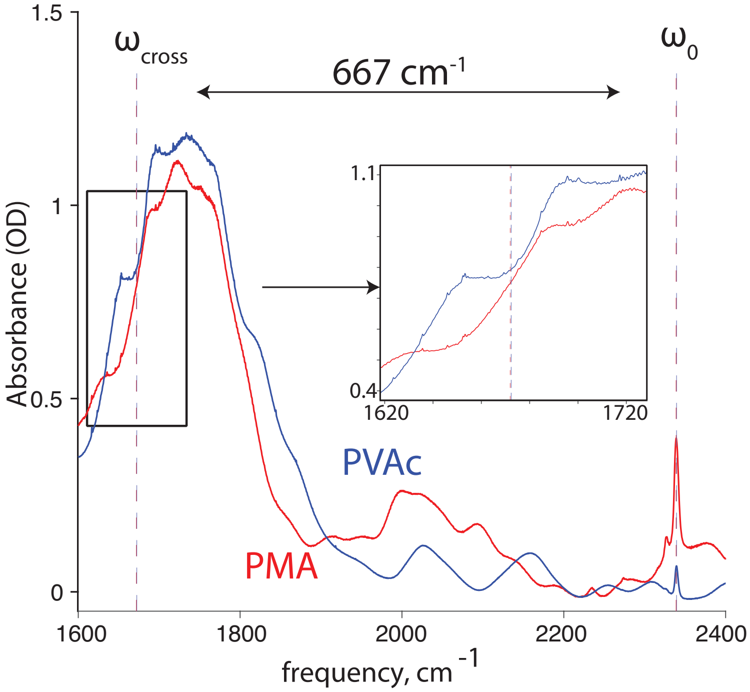

Figure 7.9: The kinetic pathway regulated by k_{10} is a spontaneous transition that moves down the energy landscape of CO_2. The gap frequency (ω_{cross}) is then the difference between the center frequency of the main antisymmetric stretch band and the bending frequency (667 cm^{-1}) . This frequency in PVAc and PMA is on the low frequency edge of the bands corresponding to carbonyl vibrational bands. There are only minimal differences in the band structure between samples.

In previous work, we correlated the difference in the crossover rate (k_{10}) with the background absorbance in FTIR spectra at a frequency equivalent to the energy lost by the k_{10} pathway, as a proxy of vibrational density of states.[187] Similar analysis for these samples (figure 7.9) does not produce a similar result. In the previous system, three separate materials were analyzed, including an ionic liquid, a cross-linked polymer gel, and a composite material. In this sample set, there were larger variations in center frequency, which would change the frequency of crossover ($|0\,1\rangle \rightarrow |1\,0\rangle$,), but in this system there is only a very small difference in center frequency. Thus, the density of states explanation fails to explain the observed result.

PVAc- and PMA-like monomers each have three distinct binding configurations with the central carbon of CO_2: (1) the ether oxygen, (2) the carbonyl oxygen with the oxygen tilted towards the methyl and (3) the carbonyl oxygen with the oxygen oriented towards the ether oxygen.[211] Ultimately, for the monomers, there were not distinct differences in binding energies reported for these monomer structures at 0 K with a single CO_2 molecule. The binding configuration of a dimer-like sub-unit of PVAc was also modeled.[202]. This dimer was compared to a dimer of poly(lactic acid) which contains an ester moiety along the backbone. Tapriyal *et al.*[202] concluded that a major contributor to the CO_2 solubility of PVAc was the conformational flexibility and large number of rotational isomers that were possible for the PVAc-like side chain.

IVR rate differences and the interaction differences between CO_2 and the isomeric polymers most likely result from the orientation of the polymer pendant groups and the size of the cavities that CO_2 occupies. Similar calculations to the Tapriyal *et al.* results do not exist for PMA. The similarity in monomer energies does not provide strong evidence that a difference would be meaningful between the dimers. Modeling entire polymers is a computationally expensive and time consuming process but may be the necessary next step in this investigation.

7.6 Conclusion

The CO_2 solubility discrepancy between structural isomers poly(methyl acrylate) and poly(vinyl acetate) has puzzled the scientific community for many years. Using 2D-IR spectroscopy we probed the molecular environment of CO_2 in each of these polymers, and extracted both frequency-fluctuation dynamics and intramolecular kinetics.

As measured by FTIR, the center frequencies of CO_2 in each system differed by only half a wavenumber. The most notable difference is the FWHM, which is nearly two wavenumbers larger in PMA compared to PVAc.

CLS analysis of 2D-IR spectra indicated that there is very little difference between the rates of frequency fluctuation for CO_2 in each environment despite the difference in glass transition temperatures and molecular weights. The frequency fluctuation correlation function revealed structural reorganization dynamics on the order of 1 ns. The experiment, which measured out to 200 ps is then only capturing the beginning of this process.

The intramolecular kinetic exchange between the antisymmetric stretch and the hot band shoulder is captured by the experiment. This is the most significant difference between the two systems: the exchange between manifolds is nearly two times faster for PVAc, and the hot ground state both forms and decays sooner. Slower cross-manifold exchange in PMA leads to a longer-lasting hot ground state.

There are multiple possible physical explanations with varying likelihoods. Bulk scale properties, such as glass transition and molecular weight are unlikely influences on these molecular-domain measurements. A smaller scale ordering or density variation may be present, but at such low CO_2 concentrations and on such small relevant length scales, it would be unlikely to see phase density play a role. There is no clear indication of a density of states explanation.

The most likely explanation for the difference is the packing of the side chains around the CO_2 molecules and the resulting size of these cavities. To access this level of detail, a larger scale modeling process would likely be needed, given that no large energy differences are measured in monomer or dimer modeling experiments.

7.7 Acknowledgements

The authors would like to acknowledge Thomas Gasmire, of the University of Pittsburgh Machine Shop for fabrication of sample cells. We would also like to thank Dr. Jennifer Laaser for many useful conversations and Victoria Kong for NMR assistance. Thanks to the National Science Foundation (CHE-1954848, S. G.-R.), and the Science, Mathematics and Research for Transformation (SMART) Scholarship (C.J.K. 2016-present).

8.0 Conclusion

The overarching goal of the work described in this thesis is to utilize 2D-IR spectroscopy to understand the microscopic environment of carbon dioxide (CO_2) in polymers and composite materials. Previous investigations focused on CO_2 or other chromophores and their interactions with liquid-phase media. This work pushed those ideas beyond liquid and into the realm of both rubbery and glassy solids, which are of interest for their potential carbon capture and storage (CCS) applications. The results are a building block upon which further investigation of the microscopic environments of CO_2 in solids and composite materials can be built.

Our experiments continually emphasized the importance of understanding the interaction between CO_2 and the polymer-IL interface of a composite system. There are three main categories of conclusions: a re-evaluation of CO_2's intramolecular vibrational kinetics, the influence of complex environments on CO_2 frequency fluctuation dynamics, and the potential relationship between these molecular-scale investigations and bulk-scale properties.

8.1 Vibrational Energy Relaxation in CO_2

Measuring 2D-IR in polymeric media produced an unexpected result: a hot ground state.[187] This reproducible spectral feature lead to a re-evaluation of CO_2's vibrational energy levels and the connections between them. The results generated reflect the complexity of vibrational energy relaxation (VER) in CO_2, as well as the role the matrix plays in activating (or suppressing) these kinetic pathways.

Generating this kinetic model produces a new method of spectral analysis. Despite this slow overall solvent reorganization seen in PVAc and PMA, the cross-peak formation, and therefore the VER, happened on experimentally relevant timescales (chapter 7). Using the kinetic model, we were able to extract the difference in VER rates despite no significant difference in spectral diffusion. As the polymers were otherwise identical, this experiment provides a tentative link between variation in bulk properties (in this case, cloud point pressure) and VER.

The k_{10} pathway that generates the hot ground state (figure 4.3d) is present in all CO_2 systems. In ionic liquids, the rate of this transition is similar to the rate of upward exchange, k_u, which leads to a net zero peak in the overlap region. From the appearance of spectra measured in PEGDA (figure 4.3), PVAc, PMA (figure 7.5), and low vol% IL ion gels (figures A.14-A.19), either slow spectral diffusion dynamics or some specific interaction with a polymeric backbone activates this pathway. This leads to higher intensity in the pathway that generates the hot ground state compared to the pathway that generates the blue cross-peak (figure 4.8).

Investigating how the matrix influences kinetic rates is an important next step in understanding the relationship between CO_2's VER and any bulk properties of its matrix. Two-color 2D-IR experiments, which pump CO_2 and probe solvent modes (or vice versa), could help identify which solvent modes accept the energy that is lost during the crossover transition, as suggested by the density of states theory (figure 4.7). Should these modes not be IR-active, it may be necessary to move to a technique such as IR-pump, Raman-probe.

Characterization of the materials by differential scanning calorimetry or neutron scattering may offer important structural information about the samples. Molecular modeling is a powerful companion to 2D-IR spectroscopy, and while modeling of polymers is currently a computationally difficult process, this would be another route of understanding the shape of the cavity around CO_2 and tracking both charge and energy transfer between CO_2 and solvent modes.

8.2 Spectral Diffusion and Frequency Dynamics in Composite Materials

Composite materials of ionic liquids and polymers have a number of composition-dependent features that we probed with CO_2. In chapter 6, as a result of slow overall solvent reorganization timescales, there was an increased effect of rotation induced spectral diffusion. In addition, chapter 5 shows that the vol% had a non-monotonic effect on the CO_2 dynamics measured. We proposed models that best explain the interactions that were measured in these materials.

While the primary purpose of chapter 6 was to show that the frequency dependence of anisotropy was an effect of RISD, the use of an ion gel as a case study introduced the notion that rotational effects may play a far larger role in 2D-IR spectroscopy in these kinds of materials than expected. Further investigation of these reorientational motions may lead to further applications of 2D-IR spectroscopy in investigating and understanding the morphology and arrangement of polymers around a chromophore, as has been recently demonstrated for determination of free volume in polymers.[199]

The core-shell-matrix model developed in chapter 5 explores the environments CO_2 experiences within mixed-matrix materials. To further validate the core-shell-matrix model derived, experiments on low vol% ion gels would be useful to support the critical volume hypothesis. Additionally, these sorts of studies in other blended materials may help to describe the uniformity and morphology of the local environment in the resulting composites.

The thermodynamics and effects on bulk properties have been widely studied for binary mixtures of ionic liquids,[51,212–216] and the behavior of blended polymers has also been examined.[96,217–221] For both polymers and ionic liquid mixtures, many properties (entropy of mixing, excess molar volume, viscosity, local friction) are dependent on exactly which IL is used.[222,223] The molecular-scale dynamics reported in chapter 5 clearly deviate from what would have been predicted by ideal mixing, and while the core-shell-matrix model adequately explains this behavior, further investigating the thermodynamics of these complex mixtures may shed light on their origin.

8.3 The Microscopic Environment of CO_2 and Macroscopic Properties

Measuring 2D-IR spectra of CO_2 in ionic liquids was well established by the start of this work; however, initial attempts to measure CO_2 in ion gels failed for exactly the reason that these membranes are useful: fast diffusion. Measured via FTIR, CO_2 was diffusing out of the membrane faster than the length of time needed to collect a full set of 2D-IR data.

This led to the development of the gas flow cells and better experimental practices for both solid samples and gas chromophores, but also an initial hypothesis: the spectral diffusion dynamics of CO_2 were going to be fast because the bulk diffusion was fast.

The results, as seen in this work, are in fact the opposite: compared to organic solvents or even some low-viscosity ionic liquids, the rate of spectral diffusion is often as much as two orders of magnitude slower in polymer and composite media. Evidence has shown that the timescales of spectral diffusion can be related to bulk properties, such as viscosity.[17,28,51] A broader inquiry into other bulk properties, particularly permeability or selectivity, and their association with microscopic quantities (dynamics or kinetics) may uncover the microscopic interactions that govern the bulk processes.

Another important concept, both to 2D-IR spectroscopy and to carbon capture and storage applications, is the impact of the presence of water. In the experiments described in chapters 4, 6 and 7, the water content between samples was approximately constant. In chapter 5, the water content was very different between some samples, but there was no significant correlation in the data measured (figure 5.6). Adding water to ionic liquids typically increases the rate of diffusion for the ionic liquids and shifts the dynamics towards more water-like behavior.[224–228] A closer look at water impacts is an important next step, since water's impact on membrane gas separations is complicated, though in some cases it can have a general positive effect on CO_2 separation.[229–231]

As discussed in the introduction, there are seemingly endless combinations of polymers and ionic liquids to investigate, as well as other carbon capture materials such as MOFs, or polymerized ionic liquids that would be interesting comparisons, or answer intriguing questions. For poly(ionic liquids), 2D-IR spectra of a series of variably polymerized gels could help understand if the previously identified energy transfer between CO_2 and the anion persists in these materials. Measurement of CO_2 interactions with MOFs by 2DIR is enabled by the gas flow cell methodology developed for polymers, and could provide intriguing insight. Despite decades of research on CO_2, there are still many unanswered questions and this work lays a foundation for how to approach them.

Appendix

A.1 Intramolecular Vibrational Relaxation of CO_2 in Ion Gels

A.1.1 Overview

The spectral simulation methods are described, along with providing the full set of non-rephasing Feynman diagrams, corresponding to the rephasing diagrams found in the main text (Figure 4.4). Complete data sets for all three experimental samples; 100P-0I, 50P-50I, and 0P-100I, are provided (Figures A.2-A.10). The peak amplitude versus time plots are provided for the 50P-50I and 0P-100I samples (Figures A.11,A.12). These correspond to figure 4.6 in the main text, which is for the 100P-0I sample.

A.1.2 Spectra Simulation Details and Fit Parameters

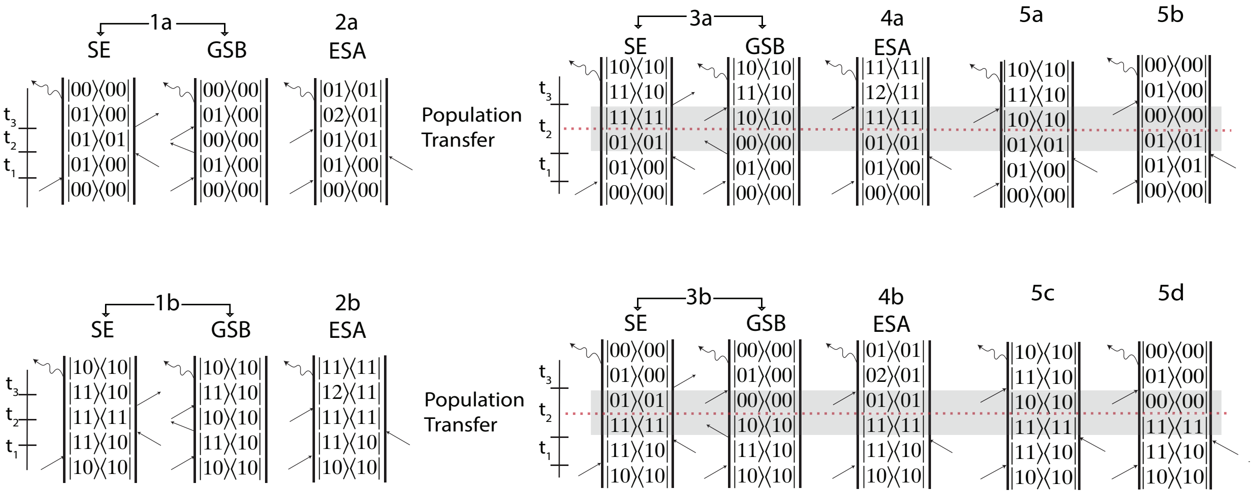

Figure A.1: Non-rephasing Feynman diagrams. All rephasing diagrams are shown in Figure 4.4 in the main text.

The 2D-IR spectra were calculated based on diagrammatic perturbation theory in the typical approximations of Gaussian statistics. There are 16 rephasing (main text, Figure

4.4) and 16 non-rephasing (Figure A.1) double-sided Feynman diagrams. We factorize the orientational and frequency fluctuation terms. The cumulant expansion allows us to represent the frequency fluctuations in terms of the two-time frequency correlation functions. In these approximation, the total response is

$$S(t_1, t_2, t_3) = Y_p(t_1, t_2, t_3) \left(\sum_{j=1}^{32} P_j(t_2) R_j(t_1, t_2, t_3) \right) \tag{49}$$

where Y_p is the orientational response for polarization condition p, P_j models population equilibration, and R_j is frequency response from Feynman diagram j.

Frequency fluctuations lead to the typical third-order response functions

$$\begin{aligned} R_r(t_1, t_2, t_3) &= (-1)^m \mu_B^2 \mu_A^2 \exp(-i\omega_A t_1 + i\omega_B t_3) + \phi) \exp(-g(t_1) + g(t_2) - g(t_3) \\ &\quad - g(t_1 + t_2) - g(t_2 + t_3) + g(t_1 + t_2 + t_3)) \qquad \text{(rephasing)} \qquad (50) \\ R_{nr}(t_1, t_2, t_3) &= (-1)^m \mu_B^2 \mu_A^2 \exp(-i\omega_A t_1 - i\omega_B t_3) - \phi) \exp(-g(t_1) - g(t_2) - g(t_3) \\ &\quad + g(t_1 + t_2) + g(t_2 + t_3) - g(t_1 + t_2 + t_3)) \qquad \text{(non-rephasing)} \qquad (51) \end{aligned}$$

where ω_A is the frequency of oscillation during t_1, ω_B is the frequency of oscillation during t_3, m is the number of arrows on the right of the diagram, μ_A is the transition dipole from the first two interactions, μ_B is the transition dipole from the second two interactions, ϕ accounts for residual phase error in the measurement, and g is the lineshape function. The term ω_A can be either $\omega_{00\to01}$ and $\omega_{10\to11}$; and ω_B can be $\omega_{00\to01}$, $\omega_{10\to11}$, $\omega_{00\to01} - \Delta_{\text{anh}}$, or $\omega_{10\to11} - \Delta_{\text{anh}}$, where Δ_{anh} is the anharmonicity.

Population relaxation is modeled with chemical kinetics during t_2. Each Feynman diagram acquires an amplitude coefficient representing the probability of that pathway. These amplitude coefficients are calculated from diagonalizing the kinetic matrix (main text, Equation).

Note that the prefactors in the population terms, P_j, establish the initial populations in accordance with the Boltzmann distribution, and the kinetics maintain detailed balance.

We use a Kubo lineshape with a fast (homogeneous) mode and an intermediate (spectral diffusion) mode

$$g(t) = \frac{t}{T_2} + \Delta^2 \tau^2 \left(e^{-t/\tau} - 1 + \frac{t}{\tau} \right). \tag{52}$$

Orientational dynamics are accounted for with the usual orientation factors depending on the laser polarization.

The parallel polarization ($\langle ZZZZ\rangle$) gives rise to a term

$$Y_{ZZZZ}(t_1,t_2,t_3)=\frac{1}{9}\exp\left(-\frac{t_1}{3\tau_o}\right)\left(1+\frac{4}{5}\exp\left(-\frac{t_2}{\tau_o}\right)\right)\exp\left(-\frac{t_3}{3\tau_o}\right), \tag{53}$$

where τ_o is the orientational relaxation time. Similarly, the perpendicular (crossed) polarization ($\langle ZZXX\rangle$) gives rise to

$$Y_{ZZXX}(t_1,t_2,t_3)=\frac{1}{9}\exp\left(-\frac{t_1}{3\tau_o}\right)\left(1-\frac{2}{5}\exp\left(-\frac{t_2}{\tau_o}\right)\right)\exp\left(-\frac{t_3}{3\tau_o}\right). \tag{54}$$

In this work, only parallel polarization, $\langle ZZZZ\rangle$ was measured.

The signal is calculated in the rotating frame; the time domain has 64 steps separated by dt = 0.2 ps. The initial point in the time-domain is divided by 2 to reduce baseline artifacts due to the single-sided signal. The Fast Fourier Transform is performed with zero-padding to 128 points.

The constrained nonlinear least-squares fitting was performed in MATLAB using the active-set algorithm as implemented in `fmincon`. The reported fit values were robust to the precise values of the constraints (not reported). The error function that was minimized was the sum of the square deviation of the experimental spectra and the simulation including both polarization conditions.

The resulting best fit parameters are summarized in table A.1.

Table A.1: Best Fit Parameters of the Spectral Simulation

parameter	description	100P-0I	50P-50I	0P-100I
	fixed parameters			
ω_{10}	center frequency	2337.1 cm^{-1}	2339.6 cm^{-1}	2342.9 cm^{-1}
Δ_{sb}	stretch/shoulder freq. shift	11.8 cm^{-1}	10.9 cm^{-1}	12.2 cm^{-1}
Δ_{anh}	anharmonic shift	23.5 cm^{-1}	23.5 cm^{-1}	23.5 cm^{-1}
μ_{12}	1-2 dipole ratio	1.82	1.78	1.82
ϕ	phase error	0°	$-0.31°$	$-1.1°$
T	temperature	301.9 K	297 K	295 K
τ_{o}	reorientation time	34 ps	59 ps	37.5 ps
	free parameters			
lineshape function				
T_2	pure dephasing	4.51 ps	4.34 ps	3.13 ps
Δ	inhomogeneous width	1.84 cm^{-1}	2.30 cm^{-1}	1.62 cm^{-1}
τ	spectral diffusion time	81.5 ps	37.9 ps	15.8 ps
kinetic transition rates				
k_u	thermal equilibrium up rate	0.0012 ps^{-1}	0.018 ps^{-1}	0.010 ps^{-1}
k_{10}	crossover rate	0.0061 ps^{-1}	0.0128 ps^{-1}	0.022 ps^{-1}
k_r	direct relaxation rate	0.0145 ps^{-1}	0.006 ps^{-1}	$\sim$0 ps^{-1}

A.1.3 Complete Representative Data Sets

Spectra for the 100P-0I, 50P-50I, and 0P-100I samples have all been measured in triplicate. All spectra of CO_2 in this sample set include peaks in at least 7 of the eight regions (main text, Figure 4.3). The hot ground state in region V is prominent in all three replicates of the 100P-0I sample, and either not present, or indistinguishable from noise and peak overlap in the other samples. The cross-peaks in regions V-VII are present in all experiments except where obscured by the hot ground state. Center frequency is consistent between samples of the same composition.

Provided below are representative sets of all t_2 time point spectra for a single experimental run. Data was taken over 27 (0P-100I) or 28 (100P-0I, 50P-50I) t_2 times. The simulation and residual spectra calculated from these experimental spectra are also included. The data and residuals are all cropped in the Z-direction to show the bottom 50% of the peak intensity, in order to see smaller-amplitude features that would be otherwise obscured by the intensity of the main bands. The residuals are scaled for the same intensity axes as the experiment and simulation plots.

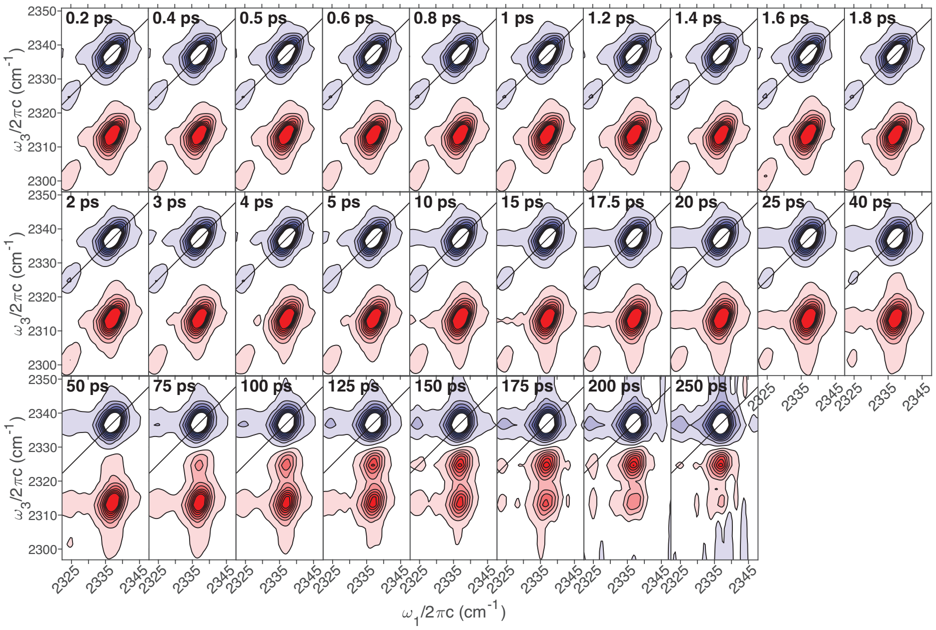

Figure A.2: All 28 experimental spectra for the 100P-0I, cl-PEGDA sample.

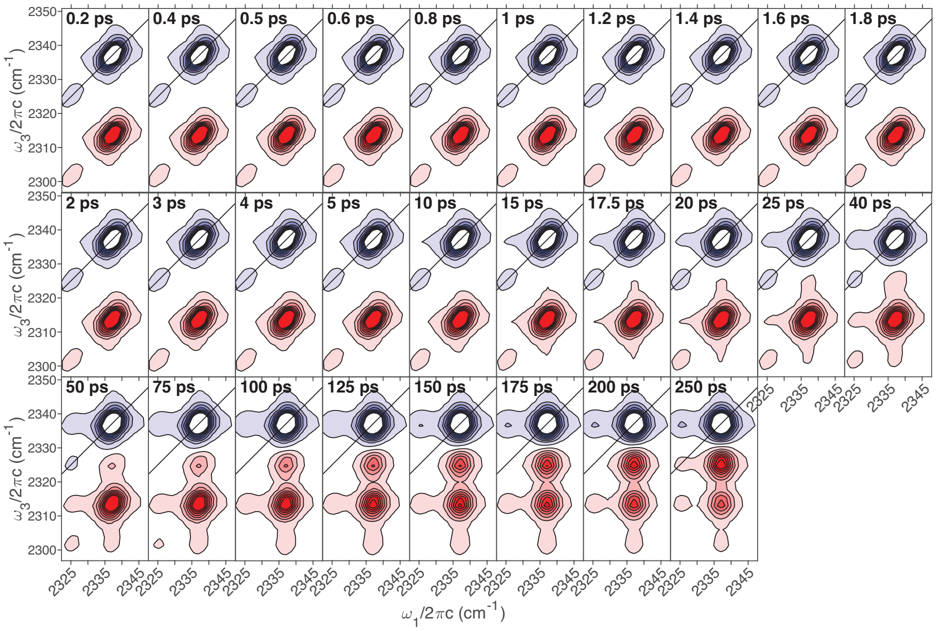

Figure A.3: All 28 simulated spectra for the 100P-0I, cl-PEGDA sample.

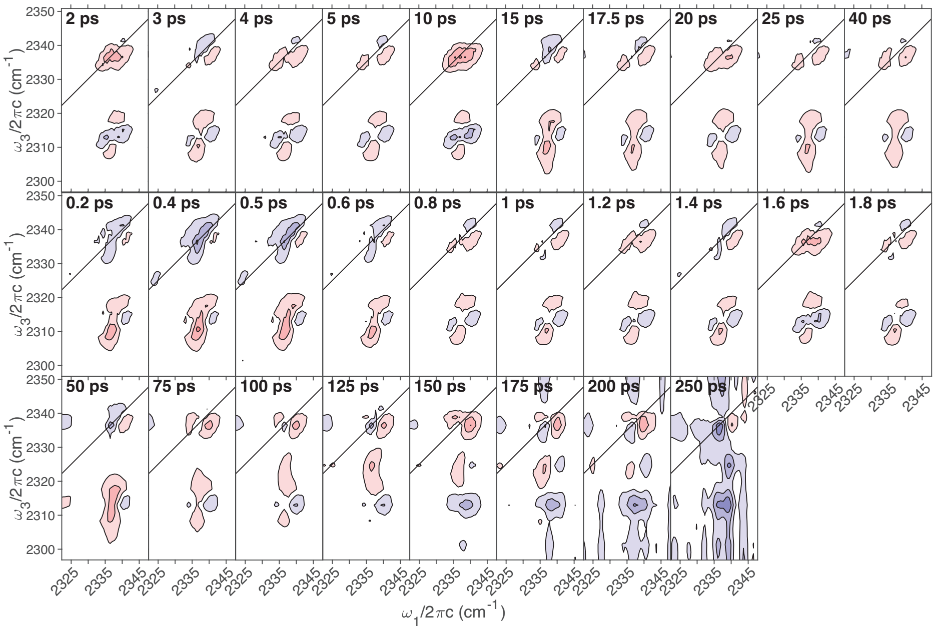

Figure A.4: Scaled residuals (simulation - data) for the 100P-0I, cl-PEGDA sample.

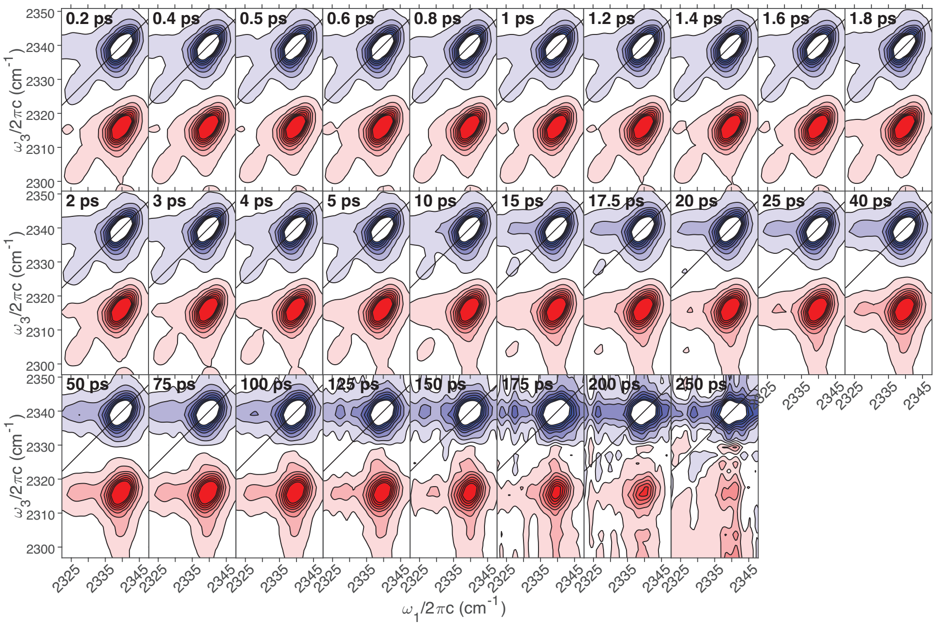

Figure A.5: All 28 experimental spectra for the 50P-50I, 50 % by volume ion gel sample.

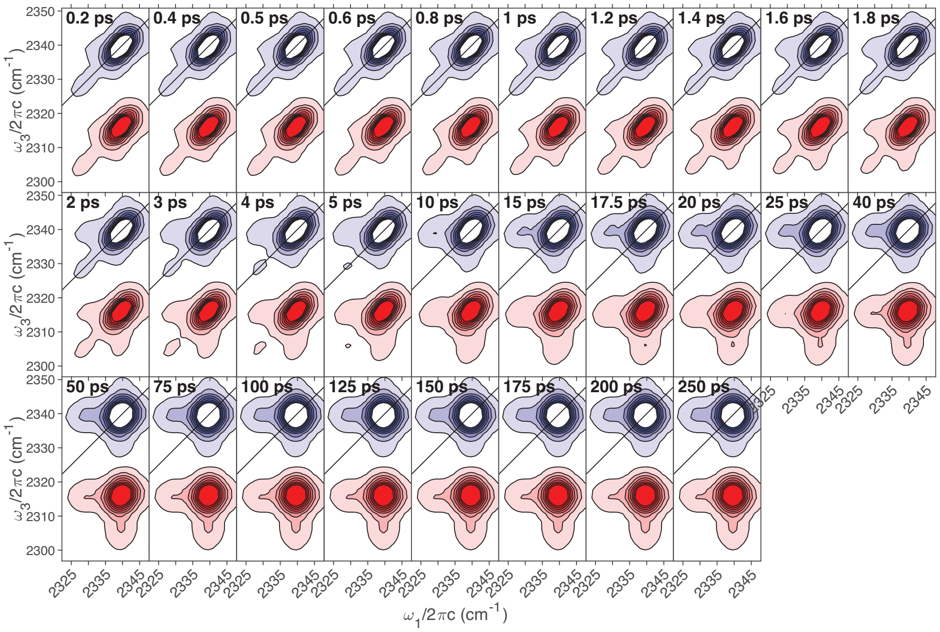

Figure A.6: All 28 simulated spectra for the 50P-50I, 50 % by volume ion gel sample.

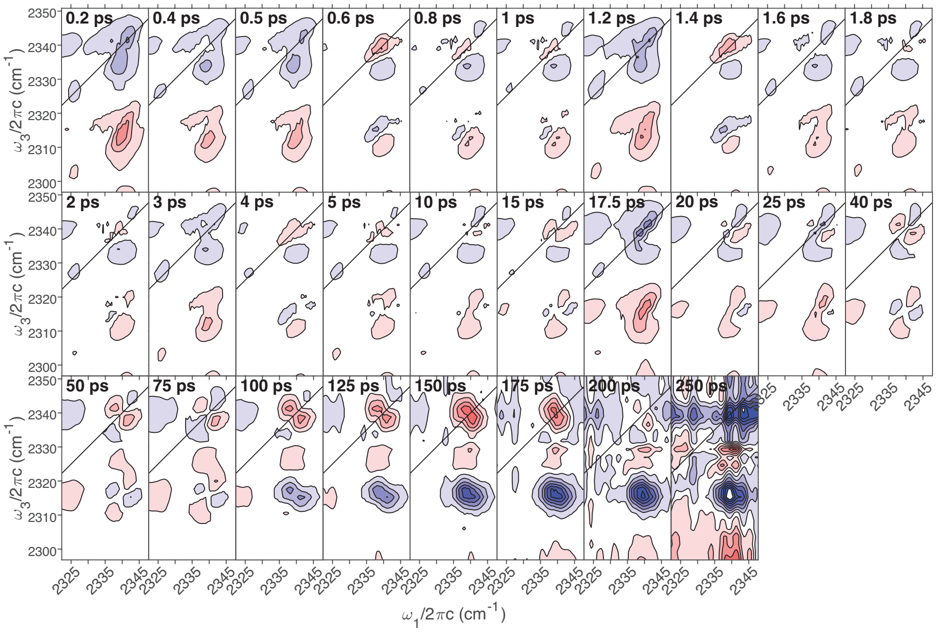

Figure A.7: Scaled residuals (simulation - data) for the 50P-50I, 50 % by volume ion gel sample.

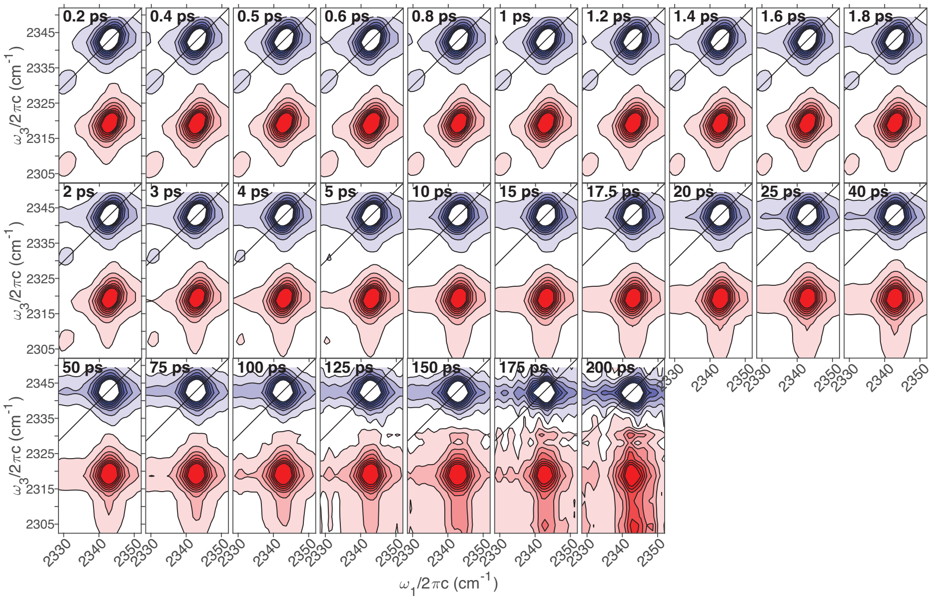

Figure A.8: All 27 experimental spectra for the 0P-100I, pure ionic liquid sample.

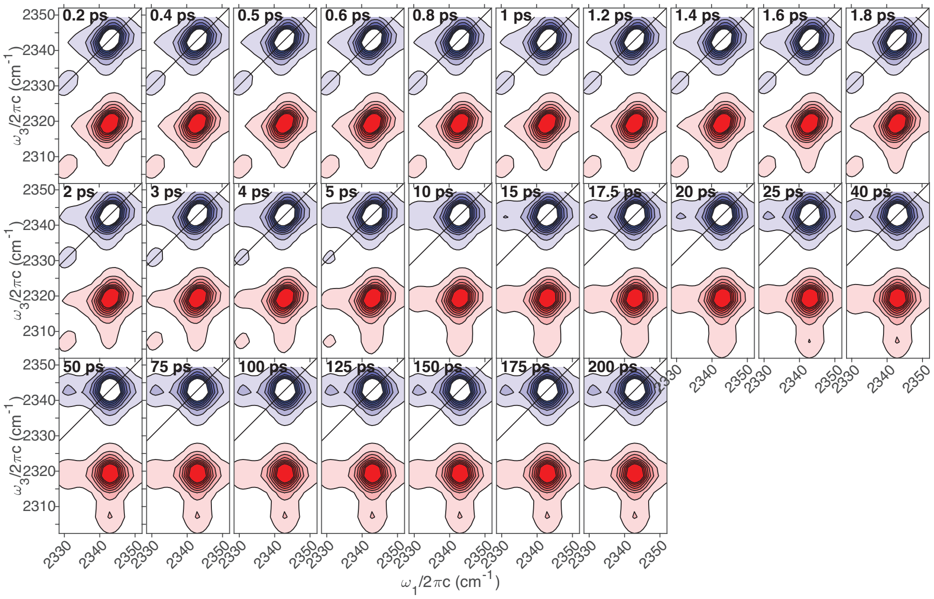

Figure A.9: All 27 simulated spectra for the 0P-100I, pure ionic liquid sample.

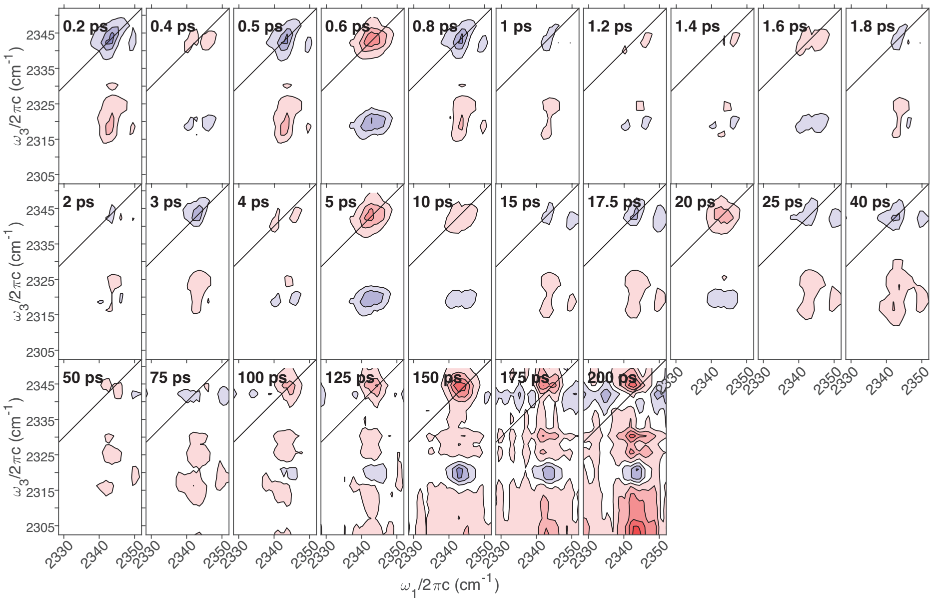

Figure A.10: Scaled residuals (simulation - data) for the 0P-100I, pure ionic liquid.

A.1.4 Peak Intensity Plots

The peak intensity in the boxed regions were summed over all time points for both the experimental and simulated spectra. This comparison provided direct evidence that the modeling was reasonably capturing the amplitude variation in the experimental spectra.

Deviations in the peak 3a/5a plot (e) for Figure A.12 are addressed in the main text, and are the result of peak overlap effects and noise.

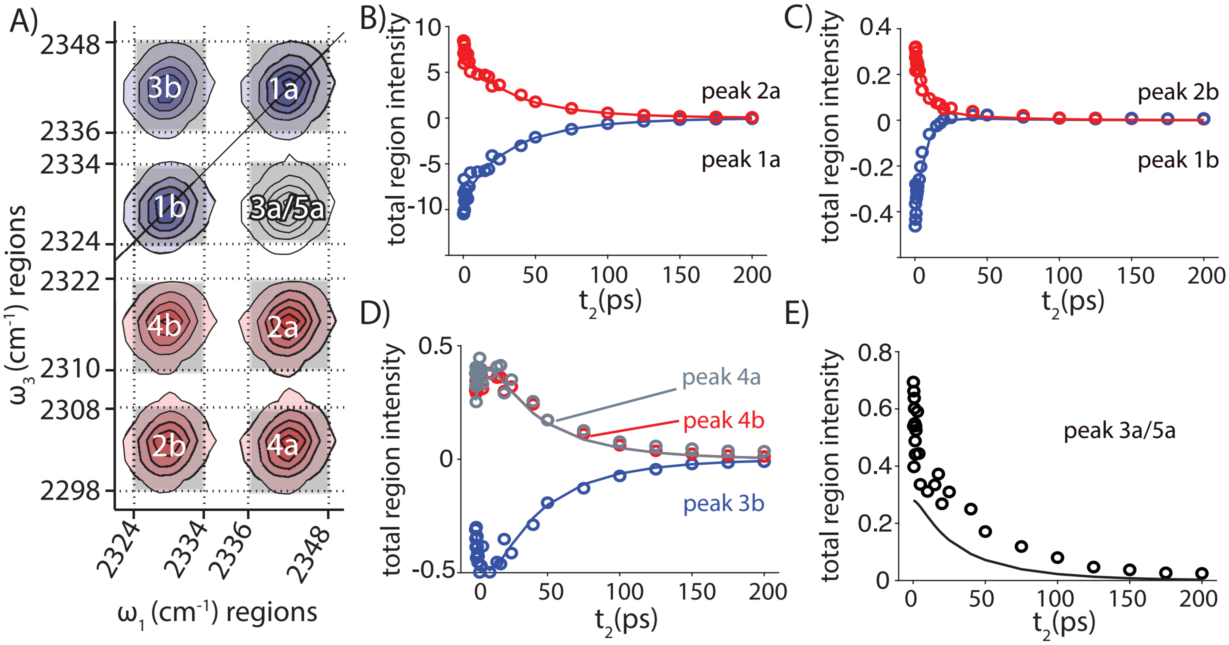

Figure A.11: Summation of peak intensities for the 0P-100I sample.

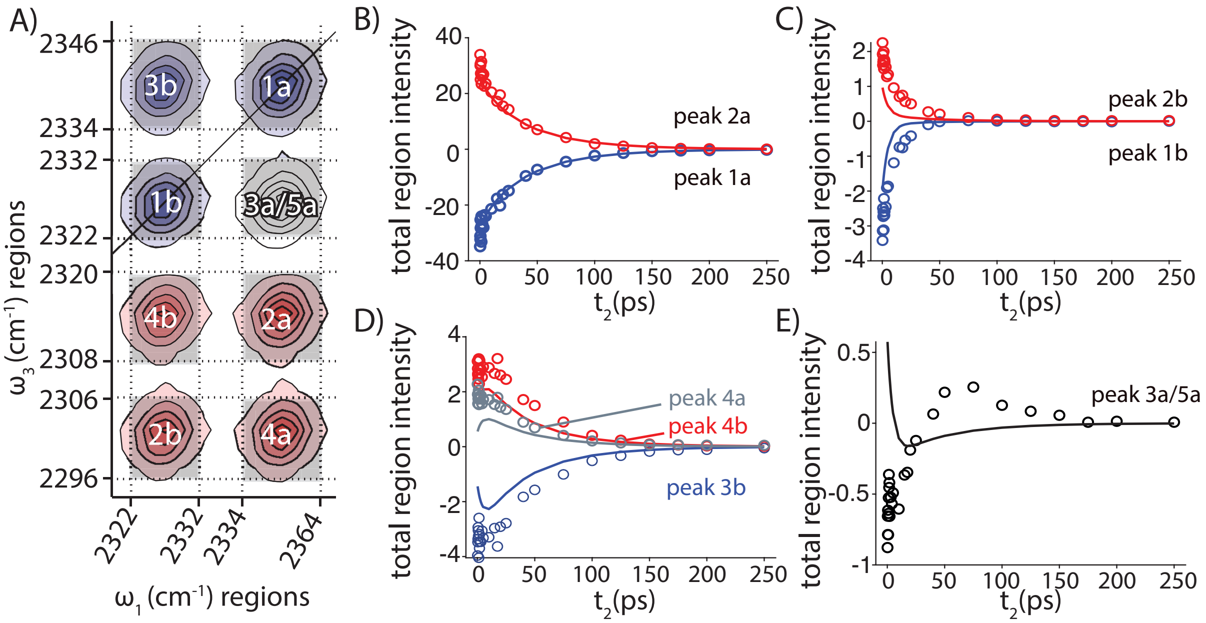

Figure A.12: Summation of peak intensity for the 50P-50I sample.

A.2 Environment Distribution in Ion Gels: A Core-Shell-Matrix Hypothesis

Full sets of FT-IR data are provided, showing the full range and agreement between samples (figure A.13). A selection of carbon dioxide (CO_2) 2D-IR spectra from each of the thirteen experiments is below (figure A.14-A.19). There are discrepancies between samples that come from variations in laser alignment, sample preparation, purging, etc. As shown in figure 5.5 in the main text, center line slope analysis showed good agreement between samples.

A.2.1 All FT-IR Spectra

Fourier-transform infrared (FTIR) spectra are taken of all experimental samples prior to running an ultrafast two-dimensional infrared (2D-IR) experiment to ensure appropriate CO_2 concentration.

Spectra are fit to a double Voigt model in order to extract the peak centers of both the

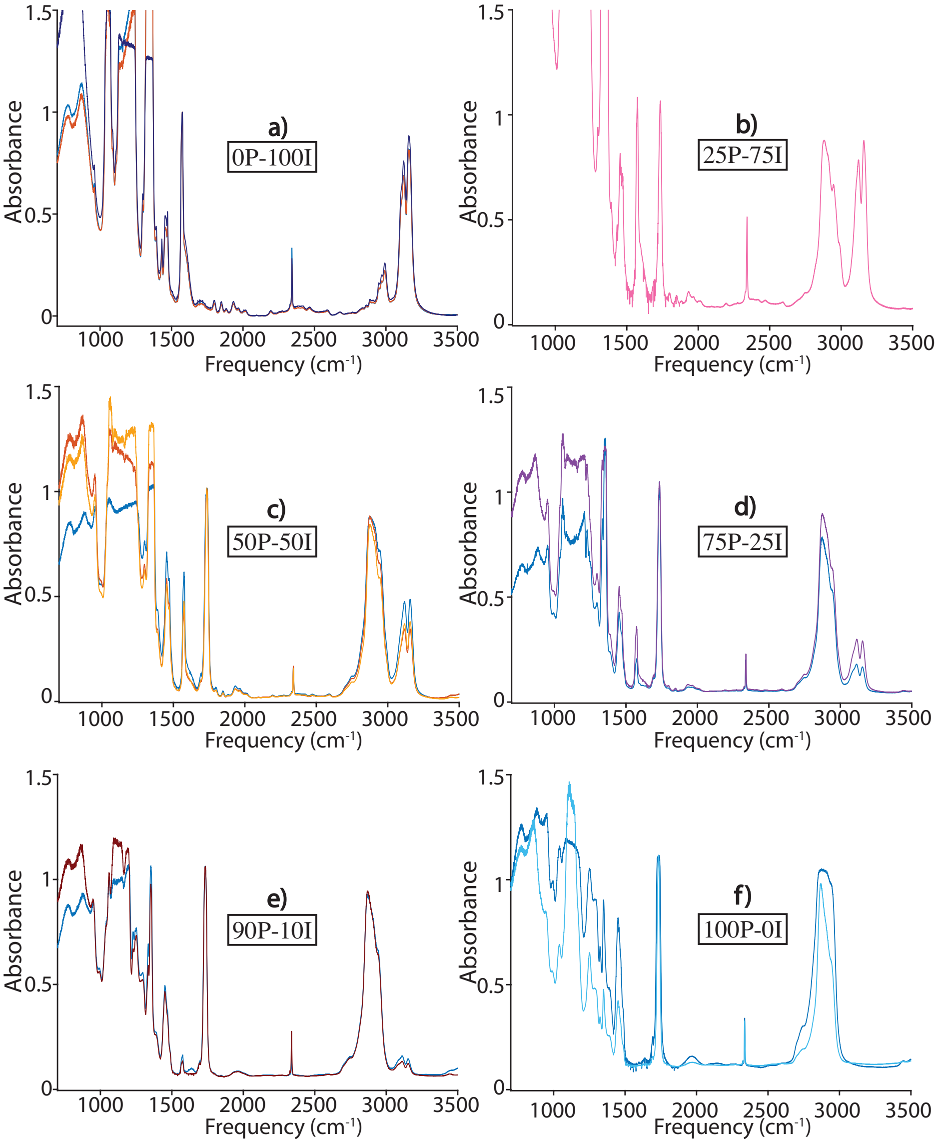

Figure A.13: Baselined, atmospherically corrected, normalized spectra for of CO_2 in all 13 samples, as measured shortly before 2D-IR spectra were taken. There is good agreement between samples.

main antisymmetric stretching peak and the shoulder. Also calculated are the difference between the two center positions, the intensity ratio between the shoulder and the main band, and the full width half max.

Table A.2: Double Voigt Fit Results

Sample	ω_0 (cm^{-1})	ω_{sb} (cm^{-1})	Δ_{sb} (cm^{-1})	I_{sb}/I_0	FWHM (cm^{-1})
Feb '18 0P-100I	2342.46	2330.14	12.3	0.10	5.3
Sep '18 0P-100I	2342.45	2330.37	12.1	0.10	5.1
May '19 0P-100I	2342.50	2330.08	12.4	0.09	5.6
Dec '19 25P-75I	2341.29	2328.69	12.6	0.10	6.8
Sep '18 50P-50I	2339.95	2327.18	12.7	0.07	6.8
May '19 50P-50I	2339.59	2326.73	12.9	0.06	6.0
Dec '19 50P-50I	2340.02	2327.19	12.8	0.06	6.5
Oct '18 75P-25I	2338.55	2325.76	12.8	0.06	5.8
Dec '19 75P-25I	2339.23	2326.41	12.8	0.06	6.0
Sep '18 90P-10I	2337.84	2325.22	12.6	0.06	5.5
Mar '20 90P-10I	2337.62	2324.96	12.7	0.06	5.3
Nov '18 100P-0I	2337.00	2324.47	12.5	0.06	4.6
May '19 100P-0I	2337.00	2324.36	12.6	0.06	4.6

A.2.2 All 2D-IR Spectra

2D-IR spectroscopy of CO_2 was measured over a range of dates from February 2018 until March of 2020. Samples are composed of X% by volume poly(ethylene glycol)diacrylate (PEGDA), and (100-X)% 1-ethyl-3-methylimidazolium bis(trifluoromethylsulfonyl)imide ([emim][Tf_2N]).

Where possible, duplicate experiments were performed to ensure validity of analysis, but due to time constraints, the 25P-75I was only measured once, though the data measured was high-quality, with good signal-to-noise and a full range of 27 waiting times (t_2) collected. All data are plotted on the same axes for ease of comparison.

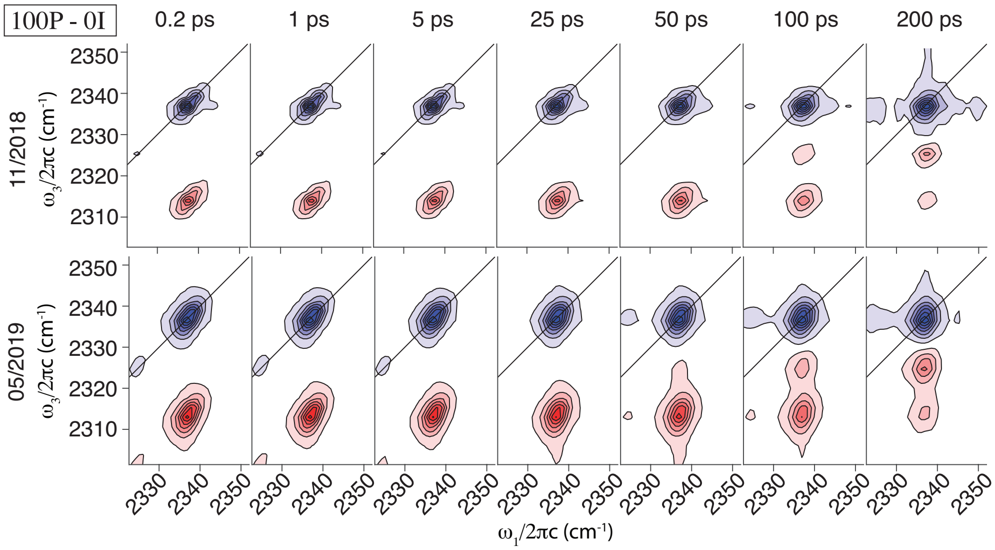

Figure A.14: Duplicate measurements of CO_2 in a cross-linked PEGDA gel. Notably, these samples have the smallest overall peaks, with a linear IR full width at half maximum of only 4.6 cm^{-1}.

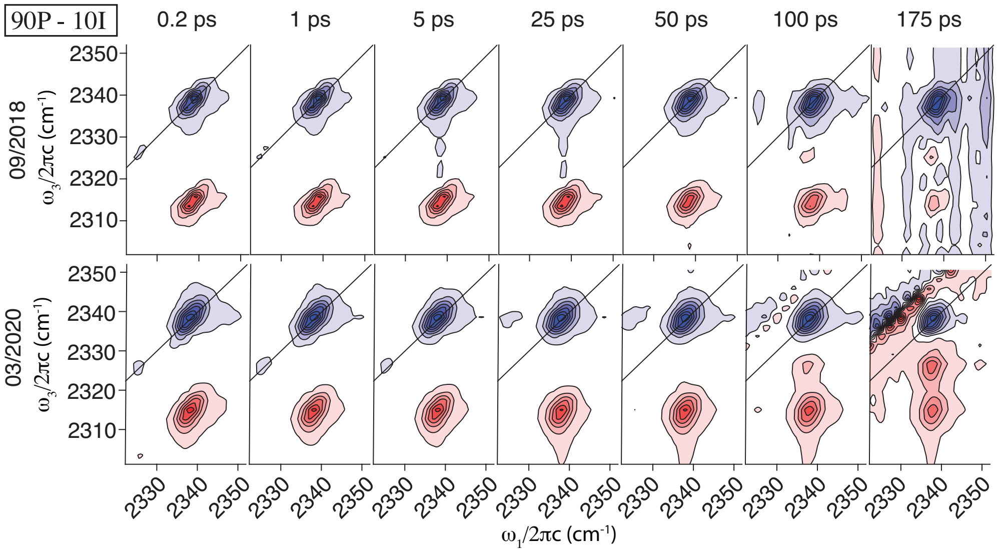

Figure A.15: Duplicate measurements of CO_2 in a 90% by volume PEGDA, 10% by volume [emim][Tf_2N] gel. In the 03/20 sample, some scattering is observed just off the diagonal.

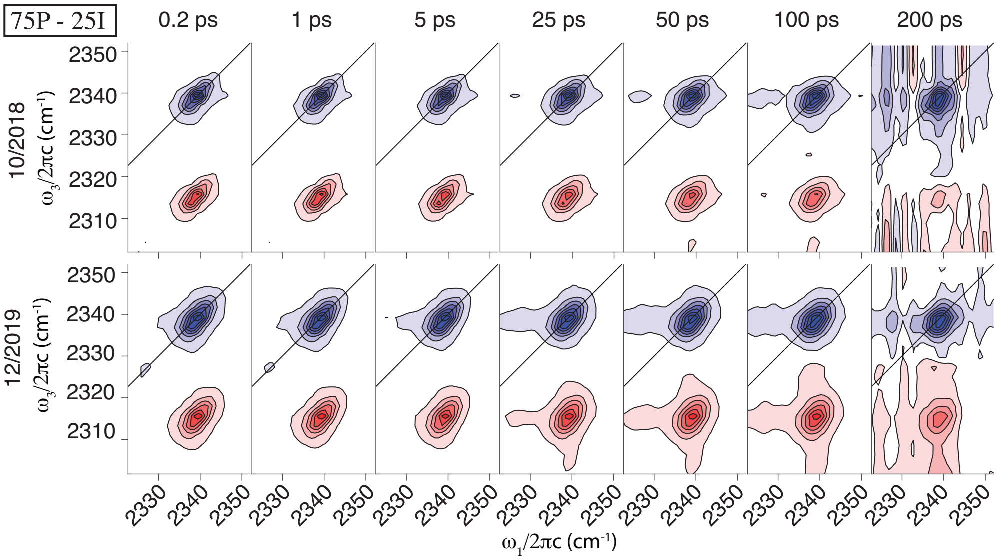

Figure A.16: Duplicate measurements of CO_2 in a 75% by volume PEGDA, 25% by volume [emim][Tf_2N] gel. Both samples show good signal-to-noise.

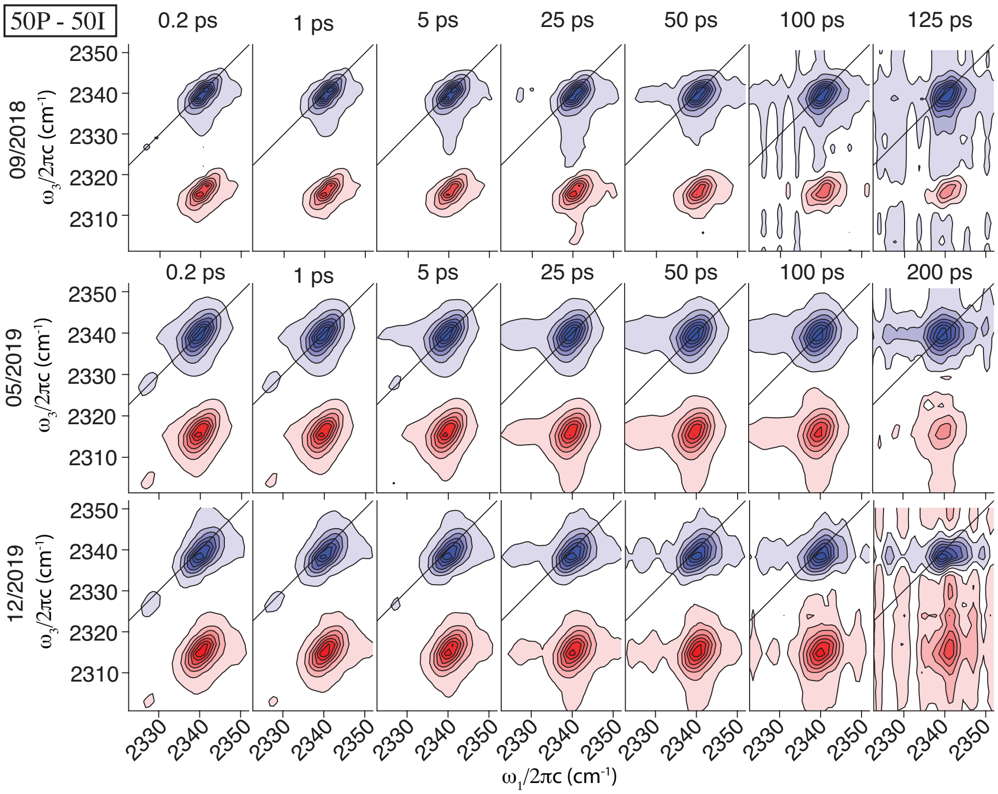

Figure A.17: Triplicate measurements of CO_2 in a 50% by volume PEGDA, 50% by volume [emim][Tf_2N] gel.

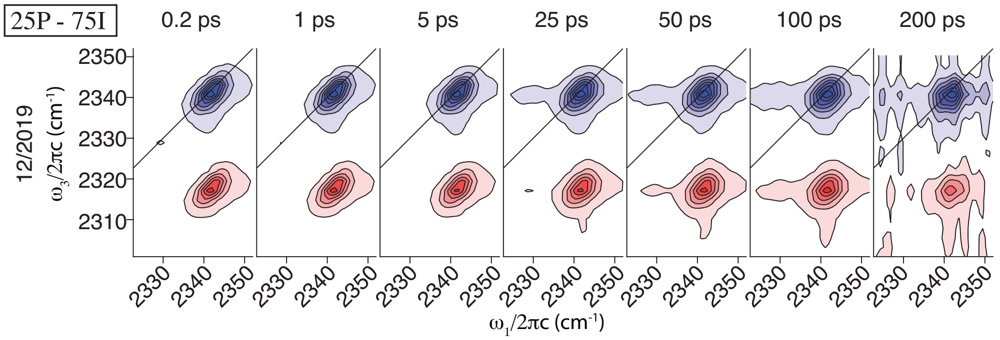

Figure A.18: A single experiment was recorded of CO_2 in a 25% by volume PEGDA, 75% by volume [emim][Tf_2N] gel.

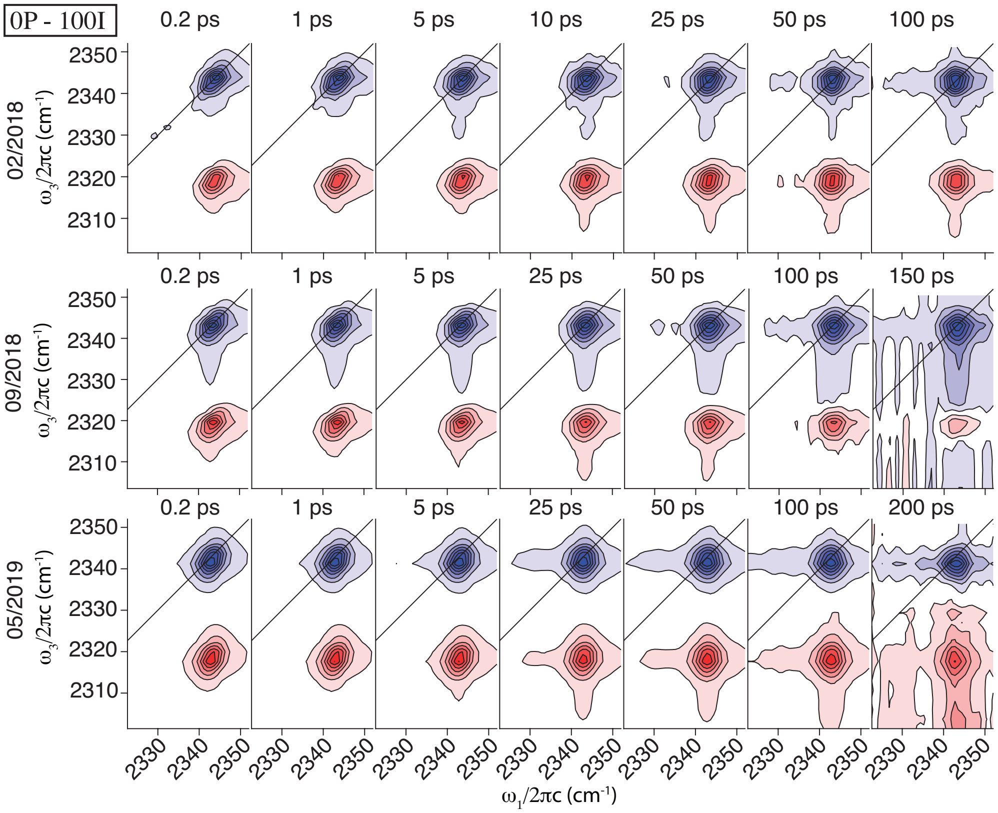

Figure A.19: Triplicate measurements of CO_2 in sample of [emim][Tf_2N]. The relatively fast spectral diffusion of CO_2 in this ionic liquid results in lower signal at earlier time points, and therefore, experiments are often terminated earlier.

A.3 Modeling the Frequency-dependent Two-dimensional Anisotropy

The complete data set for both parallel and perpendicular measurements of CO_2 in a 50% by volume poly(ethylene glycol)diacrylate, 50% by volume 1-ethyl-3-methylimidazolium bis(trifluoromethylsulfonyl)imide ([emim][Tf_2N]) gel. 42 t_2 times are displayed from 0.2 ps to 175 ps, beyond which the signal-to-noise rendes the data unreliable.

A.3.1 Full 2D-IR Spectra Data Sets

Spectra are measured by automation of the t_2-selecting translation stage and the polarization-selecting wave plate. Waiting times (t_2) are randomized, and then upon selection, the parallel measurement is recorded followed by the perpendicular. The number of scans are scaled to ensure adequate signal size for analysis.

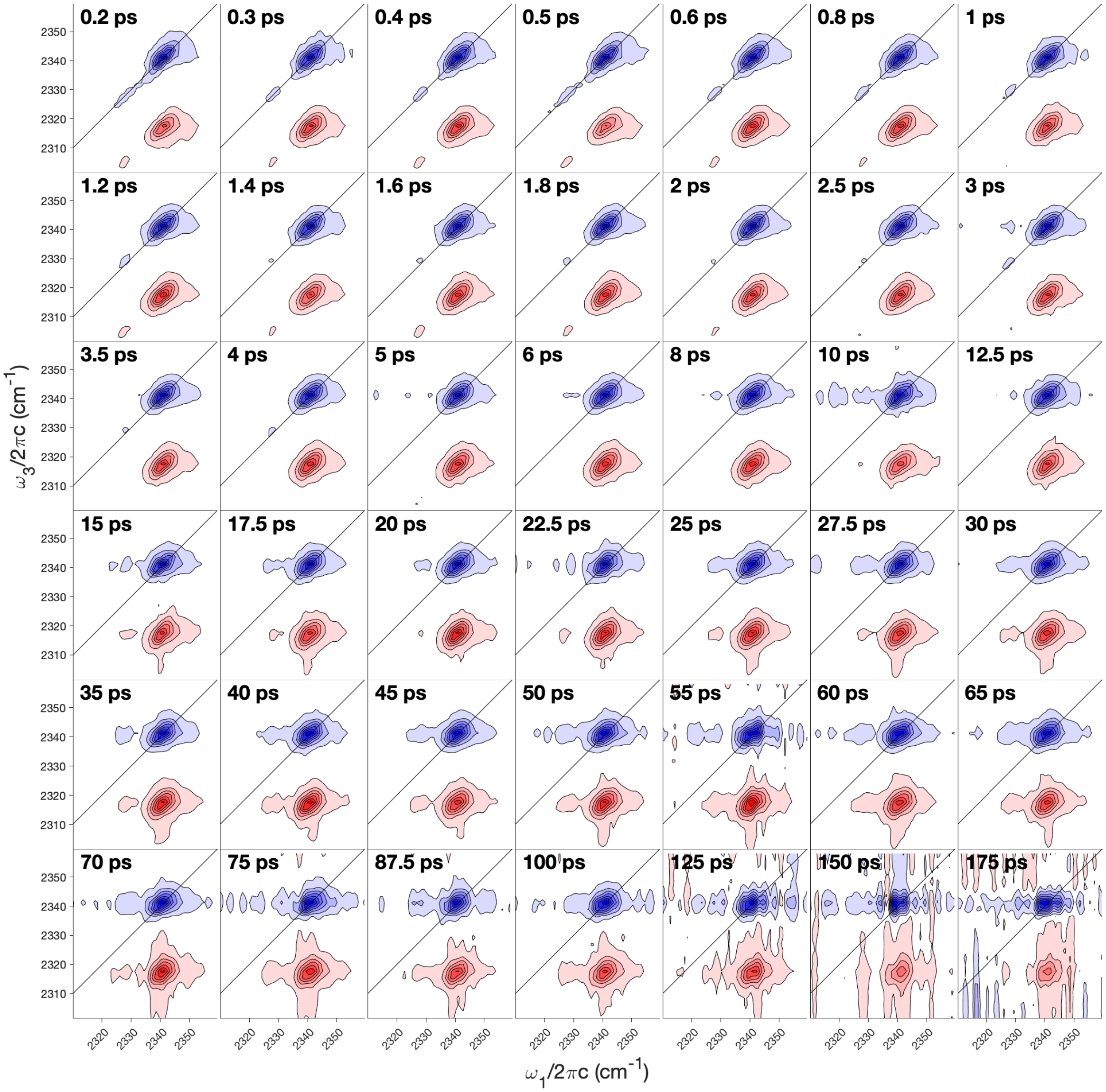

Figure A.20: All 42 t_2 times for CO_2 in the ion gel measured with parallel polarization.

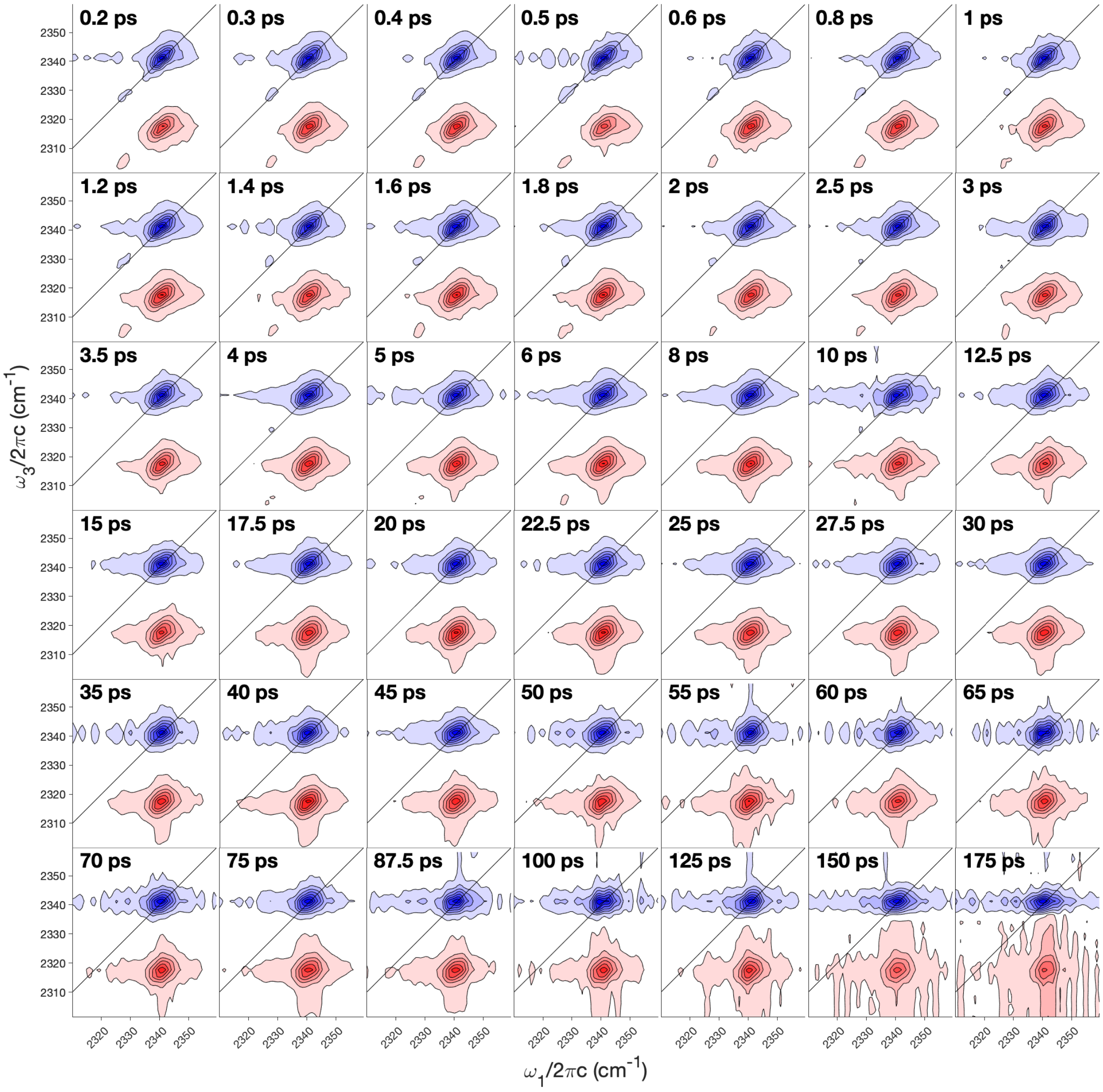

Figure A.21: All 42 t_2 times for CO_2 in the ion gel measured with perpendicular polarization.

A.3.2 Bootstrapping Results

Fitting the wobbling-in-a-cone model to the experimentally extracted FFCFs for the ion gel was performed using bootstrapping, which over n repetitions, randomly selects and removes various data points to test the robustness of the fit, with replacement. The resulting spread of the data for each fitting parameter (table 6.1) is depicted below as a histogram. Most show a reasonable and grouped distribution, but the θ_3 results show a bimodal distribution, both of which are more than twice the angle of the other two cones.

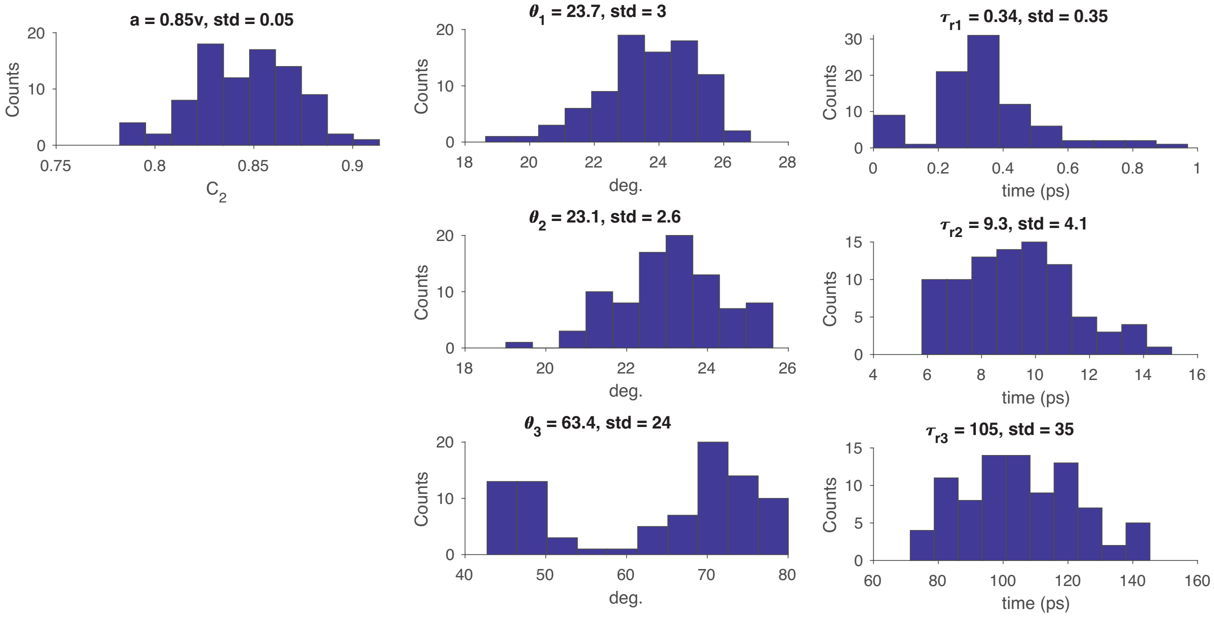

Figure A.22: Histograms from bootstrapping.

Bibliography

[1] Bui, M. *et al.* Carbon Capture and Storage (CCS): The Way Forward. *Energy Environ. Sci.* **2018**, *11*, 1062–1176.

[2] Mumford, K. A.; Wu, Y.; Smith, K. H.; Stevens, G. W. Review of Solvent Based Carbon-Dioxide Capture Technologies. *Front. Chem. Sci. Eng.* **2015**, *9*, 125–141.

[3] Karadas, F.; Atilhan, M.; Aparicio, S. Review on the Use of Ionic Liquids (ILs) as Alternative Fluids for CO2 Capture and Natural Gas Sweetening. *Energy Fuels* **2010**, *24*, 5817–5828.

[4] Jacobson, M. Z. Review of Solutions to Global Warming, Air Pollution, and Energy Security. *Energy Environ. Sci.* **2009**, *2*, 148–173.

[5] Wong, K. K.; Jawad, Z. A. A Review and Future Prospect of Polymer Blend Mixed Matrix Membrane for CO2 Separation. *J. Polym. Res.* **2019**, *26*.

[6] D'Alessandro, D. M.; Smit, B.; Long, J. R. Carbon Dioxide Capture: Prospects for New Materials. *Angew. Chemie - Int. Ed.* **2010**, *49*, 6058–6082.

[7] Pires, J.; Martins, F.; Alvim-Ferraz, M.; Simões, M. Recent Developments on Carbon Capture and Storage: An Overview. *Chem. Eng. Res. Des.* **2011**, *89*, 1446–1460.

[8] Dutcher, B.; Fan, M.; Russell, A. G. Amine-Based CO 2 Capture Technology Development from the Beginning of 2013—A Review. *ACS Appl. Mater. Interfaces* **2015**, *7*, 2137–2148.

[9] Mangalapally, H. P.; Hasse, H. Pilot Plant Study of Post-Combustion Carbon Dioxide Capture byReactive Absorption: Methodology, Comparison of Different Structured Packings, and Comprehensive Results for Monoethanolamine. *Chem. Eng. Res. Des.* **2011**, *89*, 1216–1228.

[10] Rao, A. B. Details of A Technical , Economic and Environmental Assessment of Amine-based CO 2 Capture Technology for Power Plant Greenhouse Gas Control. Appendix to Annual Technical Progress Report. Reporting period October 2000 - October 2001. **2002**, 40.

[11] Hamm, P.; Zanni, M. T. *Concepts and Methods of 2D Infrared Spectroscopy*; Cambridge University Press: New York, NY, 2011.

[12] Fayer, M. D. Ultrafast Infrared Vibrational Spectroscopy. **2013**, *2*, 487.

[13] Asbury, J. B.; Steinel, T.; Fayer, M. D. Using Ultrafast Infrared Multidimensional Correlation Spectroscopy to Aid in Vibrational Spectral Peak Assignments. *Chem. Phys. Lett.* **2003**, *381*, 139–146.

[14] Pakoulev, A.; Wang, Z. H.; Dlott, D. D. Vibrational Relaxation and Spectral Evolution Following Ultrafast OH Stretch Excitation of Water. *Chem. Phys. Lett.* **2003**, *371*, 594–600.

[15] Rey, R.; Møller, K. B.; Hynes, J. T. Hydrogen Bond Dynamics in Water and Ultrafast Infrared Spectroscopy. *J. Phys. Chem. A* **2002**, *106*, 11993–11996.

[16] Brinzer, T.; Garrett-Roe, S. Temperature and Chain Length Dependence of Ultrafast Vibrational Dynamics of Thiocyanate in Alkylimidazolium Ionic Liquids : A Random Walk On a Rugged Energy Landscape. *J. Chem. Phys.* **2017**, *147*, 194501.

[17] Brinzer, T.; Berquist, E. J.; Ren, Z.; Dutta, S.; Johnson, C. A.; Krisher, C. S.; Lambrecht, D. S.; Garrett-Roe, S. Ultrafast Vibrational Spectroscopy (2D-IR) of CO2 in Ionic Liquids: Carbon Capture from Carbon Dioxide's Point of View. *J. Chem. Phys.* **2015**, *142*, 212425.

[18] Garrett-Roe, S.; Hamm, P. What Can We Learn From Three-Dimensional Infrared Spectroscopy? *Acc. Chem. Res.* **2009**, *42*, 1412–1422.

[19] Garrett-Roe, S.; Perakis, F.; Rao, F.; Hamm, P. Three-Dimensional Infrared Spectroscopy of Isotope-Substituted Liquid Water Reveals Heterogeneous Dynamics. *J. Phys. Chem. B* **2011**, *115*, 6976–6984.

[20] Ren, Z.; Brinzer, T.; Dutta, S.; Garrett-Roe, S. Thiocyanate as a Local Probe of Ultrafast Structure and Dynamics in Imidazolium-Based Ionic Liquids: Water Induced Heterogeneity and Cation Induced Ion-Pairing. *J. Phys. Chem. B* **2015**, *119*, 4699–4712.

[21] Shattuck, J. T.; Schneck, J. R.; Chieffo, L. R.; Erramilli, S.; Ziegler, L. D. Dispersed Three-Pulse Infrared Photon Echoes of Nitrous Oxide in Water and Octanol. *J. Phys. Chem. B* **2013**, *117*, 15774–15785.

[22] Thielges, M. C.; Fayer, M. D. Protein Dynamics Studied with Ultrafast Two-Dimensional Infrared Vibrational Echo Spectroscopy. *Acc. Chem. Res.* **2012**, *45*, 1866–1874.

[23] Hamm, P.; Lim, M.; DeGrado, W. F.; Hochstrasser, R. M. The Two-Dimensional IR Nonlinear Spectroscopy of a Cyclic Penta-Peptide in Relation to its Three-Dimensional Structure. *Proc. Natl. Acad. Sci. U. S. A.* **1999**, *96*, 2036–2041.

[24] Ghosh, A.; Tucker, M. J.; Hochstrasser, R. M. Identification of Arginine Residues in Peptides by 2D-IR Echo Spectroscopy. *J. Phys. Chem. A* **2011**, *115*, 9731–9738.

[25] Ge, N.-H.; Zanni, M. T.; Hochstrasser, R. M. Effects of Vibrational Frequency Correlations on Two-Dimensional Infrared Spectra. *J. Phys. Chem. A* **2002**, *106*, 962–972.

[26] Ghosh, A.; Ostrander, J. S.; Zanni, M. T. Watching Proteins Wiggle: Mapping Structures with Two-Dimensional Infrared Spectroscopy. *Chem. Rev.* **2017**, *117*, 10726–10759.

[27] Reppert, M.; Tokmakoff, A. Computational Amide I 2D IR Spectroscopy as a Probe of Protein Structure and Dynamics. *Annu. Rev. Phys. Chem* **2016**, *67*, 359–86.

[28] Ren, Z.; Ivanova, A. S.; Couchot-Vore, D.; Garrett-Roe, S. Ultrafast Structure and Dynamics in Ionic Liquids: 2D-IR Spectroscopy Probes the Molecular Origin of Viscosity. *J. Phys. Chem. Lett.* **2014**, *5*, 1541–1546.

[29] Bonança, M. V. Relaxation in Finite and Isolated Classical Systems: An Extension of Onsager's Regression Hypothesis. *Phys. Rev. E - Stat. Nonlinear, Soft Matter Phys.* **2012**, *85*, 4–7.

[30] Onsager, L. Reciprocal Relations in Irreversible Processes. I. *Phys. Rev.* **1931**, *37*, 405–426.

[31] Mishonov, T. M.; Dimitrova, I. M.; Varonov, A. M. Callen–Welton Fluctuation Dissipation Theorem and Nyquist Theorem as a Consequence of Detailed Balance Principle Applied to an Oscillator. *Phys. A Stat. Mech. its Appl.* **2019**, *530*, 121577.

[32] Mehboudi, M.; Sanpera, A.; Parrondo, J. M. R. Fluctuation-Dissipation Theorem for Non-Equilibrium Quantum Systems. *Quantum* **2018**, *2*, 66.

[33] Berquist, E. J.; Daly, C. A., Jr.; Brinzer, T.; Bullard, K. K.; Campbell, Z. M.; Corcelli, S. A.; Garrett-Roe, S.; Lambrecht, D. S. Modeling Carbon Dioxide Vibrational Frequencies in Ionic Liquids: I. Ab Initio Calculations. *J. Phys. Chem. B* **2017**, *121*, 208–220.

[34] Daly, C. A., Jr. *et al.* Modeling Carbon Dioxide Vibrational Frequencies in Ionic Liquids: II. Spectroscopic Map. *J. Phys. Chem. B* **2016**, *120*, 12633–12642.

[35] Brinzer, T.; Daly, C. A.; Allison, C.; Garrett-Roe, S.; Corcelli, S. A.; Daly, C. A., Jr.; Allison, C.; Garrett-Roe, S.; Corcelli, S. A.; Daly, C. A.; Allison, C.; Garrett-Roe, S.; Corcelli, S. A. Modeling Carbon Dioxide Vibrational Frequencies in Ionic Liquids: III. Dynamics and Spectroscopy. *J. Phys. Chem. B* **2018**, *122*, 8931–8942.

[36] Daly, C. A., Jr.; Allison, C.; Corcelli, S. A. Modeling Carbon Dioxide Vibrational Frequencies in Ionic Liquids: IV. Temperature Dependence. *J. Phys. Chem. B* **2019**, *123*, 3797–3803.

[37] Ramdin, M.; de Loos, T. W.; Vlugt, T. J. H. State-of-the-Art of CO_2 Capture with Ionic Liquids. *Ind. Eng. Chem. Res.* **2012**, *51*, 8149–8177.

[38] Liu, H.; Huang, J.; Pendleton, P. *Recent Adv. Post-Combustion CO2 Capture Chem.*; ACS Symposium Series 1097; American Chemical Society, 2012; Vol. 1097; pp 153–175.

[39] Torralba-Calleja, E.; Skinner, J.; Gutiérrez-Tauste, D. CO2 Capture in Ionic Liquids: A Review of Solubilities and Experimental Methods. *J. Chem.* **2013**, *2013*.

[40] Krishnan, A.; Gopinath, K. P.; Vo, D. V. N.; Malolan, R.; Nagarajan, V. M.; Arun, J. Ionic Liquids, Deep Eutectic Solvents and Liquid Polymers as Green Solvents in Carbon Capture Technologies: A Review. *Environ. Chem. Lett.* **2020**, *18*, 2031–2054.

[41] Lei, Z.; Chen, B.; Koo, Y. M.; Macfarlane, D. R. Introduction: Ionic Liquids. *Chem. Rev.* **2017**, *117*, 6633–6635.

[42] Cadena, C.; Anthony, J. L.; Shah, J. K.; Morrow, T. I.; Brennecke, J. F.; Maginn, E. J. Why is CO2 So Soluble in Imidazolium-Based Ionic Liquids? *J. Am. Chem. Soc.* **2004**, *126*, 5300–5308.

[43] Baltus, R. E.; Counce, R. M.; Culbertson, B. H.; Luo, H.; DePaoli, D. W.; Dai, S.; Duckworth, D. C. Examination of the Potential of Ionic Liquids For Gas Separations. *Sep. Sci. Technol.* **2005**, *40*, 525–541.

[44] Bara, J. E.; Carlisle, T. K.; Gabriel, C. J.; Finotello, A.; Gin, D. L.; Noble, R. D.; Camper, D.; Finotello, A.; Gin, D. L.; Noble, R. D. Guide to CO2 Separations in Imidazolium-based Room-Temperature Ionic Liquids. *Ind. Eng. Chem. Res.* **2009**, *48*, 2739–2751.

[45] Wang, B.; Qin, L.; Mu, T.; Xue, Z.; Gao, G. Are Ionic Liquids Chemically Stable? *Chem. Rev.* **2017**, *117*, 7113–7131.

[46] Giammanco, C. H.; Kramer, P. L.; Yamada, S. A.; Nishida, J.; Tamimi, A.; Fayer, M. D. Carbon dioxide in an Ionic Liquid: Structural and Rotational Dynamics. *J. Chem. Phys.* **2016**, *144*, 104506.

[47] Giammanco, C. H.; Yamada, S. A.; Kramer, P. L.; Tamimi, A.; Fayer, M. D. Structural and Rotational Dynamics of Carbon Dioxide in 1-Alkyl-3-methylimidazolium Bis(trifluoromethylsulfonyl)imide Ionic Liquids: The Effect of Chain Length. *J. Phys. Chem. B* **2016**, *120*, 6698–6711.

[48] Daly, C. A., Jr.; Brinzer, T.; Allison, C.; Garrett-Roe, S.; Corcelli, S. A. Enthalpic Driving Force for the Selective Absorption of CO 2 by an Ionic Liquid. *J. Phys. Chem. Lett.* **2018**, *9*, 1393–1397.

[49] Buckingham, A.; Disch, R. The Quadrupole Moment of the Carbon Dioxide Molecule. *Proc. R. Soc. London. Ser. A Math. Phys. Sci.* **1963**, *273*, 275–289.

[50] Kramer, P. L.; Nishida, J.; Fayer, M. D. Separation of Experimental 2D IR Frequency-Frequency Correlation Functions Into Structural and Reorientation-Induced Contributions. *J. Chem. Phys.* **2015**, *143*, 124505.

[51] Ivanova, A. S.; Brinzer, T.; Roth, E. A.; Kusuma, V. A.; Watkins, J. D.; Zhou, X.; Luebke, D.; Hopkinson, D.; Washburn, N. R.; Garrett-Roe, S.; Nulwala, H. B. Eutectic

Ionic Liquid Mixtures and Their Effect on CO_2 Solubility and Conductivity. *RSC Adv.* **2015**, *5*, 51407–51412.

[52] Tomé, L. C.; Florindo, C.; Freire, C. S. R.; Rebelo, L. P. N.; Marrucho, I. M. Playing With Ionic Liquid Mixtures to Design Engineered CO2 Separation Membranes. *Phys. Chem. Chem. Phys.* **2014**, *16*, 17172–17182.

[53] Kroon, M. C.; Karakatsani, E. K.; Economou, I. G.; Witkamp, G.-J.; Peters, C. J. Modeling of the Carbon Dioxide Solubility in Imidazolium-Based Ionic Liquids with the tPC-PSAFT Equation of State. *J. Phys. Chem. B* **2006**, *110*, 9262–9269.

[54] Gonfa, G.; Bustam, M. A.; Man, Z.; Mutalib, M. I. A. Unique Structure and Solute – Solvent Interaction in Imidazolium Based Ionic Liquids : A Review. *Asian Trans. Eng.* **2011**, *01*, 24–34.

[55] Aki, S. N. V. K.; Mellein, B. R.; Saurer, E. M.; Brennecke, J. F. High-Pressure Phase Behavior of Carbon Dioxide with Imidazolium-Based Ionic Liquids. *J. Phys. Chem. B* **2004**, *108*, 20355–20365.

[56] Gurkan, B.; Goodrich, B. F.; Mindrup, E. M.; Ficke, L. E.; Massel, M.; Seo, S.; Senftle, T. P.; Wu, H.; Glaser, M. F.; Shah, J. K.; Maginn, E. J.; Brennecke, J. F.; Scheider, W. F. Molecular Design of High Capacity, Low Viscosity Chemically Tunable Ionic Liquids for CO2 Capture. *J. Phys. Chem. Lett.* **2010**, *1*, 3494–3499.

[57] Wu, Y.; Guo, Z.; Wu, H.; Zhu, K.; Yang, L.; Ren, Y.; Liu, Y.; Wu, X.; Zhao, R.; Khan, N. A.; Ahmad, N. M.; Younas, M.; Jiang, Z. Plasticization- and Aging-Resistant Membranes with Venation-like Architecture for Efficient Carbon Capture. *J. Memb. Sci.* **2020**, *609*, 118215.

[58] Fam, W.; Mansouri, J.; Li, H.; Chen, V. Improving CO2 Separation Performance of Thin Film Composite Hollow Fiber with Pebax®1657/Ionic Liquid Gel Membranes. *J. Memb. Sci.* **2017**, *537*, 54–68.

[59] Fang, W.; Luo, Z.; Jiang, J. CO2 Capture in Poly(ionic liquid) Membranes: Atomistic Insight Into the Role of Anions. *Phys. Chem. Chem. Phys.* **2013**, *15*, 651–658.

[60] Kusuma, V. A.; Macala, M. K.; Liu, J.; Marti, A. M.; Hirsch, R. J.; Hill, L. J.; Hopkinson, D. Ionic liquid Compatibility in Polyethylene Oxide/Siloxane Ion Gel Membranes. *J. Memb. Sci.* **2018**, *545*, 292–300.

[61] Kusuma, V. A.; Chen, C.; Baker, J. S.; Macala, M. K.; Hopkinson, D. The Effect of Poly(Ethylene oxide) Cross-Linking Structure on the Mechanical Properties and CO2 Separation Performance of an Ion Gel Membrane. *Polymer (Guildf).* **2019**, *180*, 121666.

[62] Koros, W. J.; Fleming, G. K. Membrane-based Gas Separation. *Membr. Technol.* **2001**, *2001*, 16.

[63] Brunetti, A.; Scura, F.; Barbieri, G.; Drioli, E. Membrane Technologies for CO2 Separation. *J. Memb. Sci.* **2010**, *359*, 115–125.

[64] Baker, R. W.; Lokhandwala, K. Natural Gas Processing with Membranes: An Overview. *Ind. Eng. Chem. Res.* **2008**, *47*, 2109–2121.

[65] Han, Y.; Ho, W. S. W. Recent Advances in Polymeric Facilitated Transport Membranes for Carbon Dioxide Separation and Hydrogen Purification. *J. Polym. Sci.* **2020**, 2435–2449.

[66] Choi, H.-S.; Suh, M. P. Highly Selective CO_2 Capture in Flexible 3D Coordination Polymer Networks. *Angew. Chemie - Int. Ed.* **2009**, *48*, 6865–6869.

[67] Dawson, R.; Stöckel, E.; Holst, J. R.; Adams, D. J.; Cooper, A. I. Microporous Organic Polymers for Carbon Dioxide Capture. *Energy Environ. Sci.* **2011**, *4*, 4239.

[68] Freeman, B. D. Basis of Permeability/Selectivity Tradeoff Relations in Polymeric Gas Separation Membranes. *Macromolecules* **1999**, *32*, 375–380.

[69] Robeson, L. M. The Upper Bound Revisited. *J. Memb. Sci.* **2008**, *320*, 390–400.

[70] Lin, H.; Freeman, B. D. Gas Solubility, Diffusivity and Permeability in Poly(ethylene oxide). *J. Memb. Sci.* **2004**, *239*, 105–117.

[71] Lin, H.; Wagner, E. V.; Swinnea, J. S.; Freeman, B. D.; Pas, S. J.; Hill, A. J.; Kalakkunnath, S.; Kalika, D. S. Transport and Structural Characteristics of Crosslinked Poly(ethylene oxide) Rubbers. *J. Memb. Sci.* **2006**, *276*, 145–161.

[72] Scovazzo, P.; Visser, A. E.; Davis, J. H.; Rogers, R. D.; Koval, C. A.; DuBois, D. L.; Noble, R. D. In *Ion. Liq. Ind. Appl. Green Chem.*; Rogers, R. D., Seddon, K. R., Eds.; American Chemical Society, 2002; pp 69–87.

[73] Tome, L. C.; Gouveia, A. S. L.; Freire, C. S. R.; Mecerreyes, D.; Marrucho, I. M. Polymeric Ionic Liquid-Based Membranes: Influence of Polycation Variation on Gas Transport and CO2 Selectivity Properties. *J. Memb. Sci.* **2015**, *486*, 40–48.

[74] Bara, J. E.; Camper, D. E.; Gin, D. L.; Noble, R. D. Room-Temperature Ionic Liquids and Composite Materials: Platform Technologies for CO2 Capture. *Acc. Chem. Res.* **2010**, *43*, 152–159.

[75] Choi, S.; Drese, J. H.; Jones, C. W. Adsorbent Materials for Carbon Dioxide Capture from Large Anthropogenic Point Sources. *ChemSusChem* **2009**, *2*, 796–854.

[76] Ding, M.; Flaig, R. W.; Jiang, H. L.; Yaghi, O. M. Carbon Capture and Conversion Using Metal-Organic Frameworks and MOF-based Materials. *Chem. Soc. Rev.* **2019**, *48*, 2783–2828.

[77] Li, J. R.; Ma, Y.; McCarthy, M. C.; Sculley, J.; Yu, J.; Jeong, H. K.; Balbuena, P. B.; Zhou, H. C. Carbon Dioxide Capture-related Gas Adsorption and Separation in Metal-Organic Frameworks. *Coord. Chem. Rev.* **2011**, *255*, 1791–1823.

[78] Wen, H. M.; Liao, C.; Li, L.; Alsalme, A.; Alothman, Z.; Krishna, R.; Wu, H.; Zhou, W.; Hu, J.; Chen, B. A Metal-Organic Framework with Suitable Pore Size and Dual Functionalities for Highly Efficient Post-combustion CO2 Capture. *J. Mater. Chem. A* **2019**, *7*, 3128–3134.

[79] McDonald, T. M.; D'Alessandro, D. M.; Krishna, R.; Long, J. R. Enhanced Carbon Dioxide Capture Upon Incorporation of N,N'- Dimethylethylenediamine in the Metal-Organic Framework CuBTTri. *Chem. Sci.* **2011**, *2*, 2022–2028.

[80] Qazvini, O. T.; Telfer, S. G. A Robust Metal-Organic Framework for Post-combustion Carbon Dioxide Capture. *J. Mater. Chem. A* **2020**, *8*, 12028–12034.

[81] Yan, X.; Anguille, S.; Bendahan, M.; Moulin, P. Ionic Liquids Combined with Membrane Separation Processes: A Review. *Sep. Purif. Technol.* **2019**, *222*, 230–253.

[82] Hanioka, S.; Maruyama, T.; Sotani, T.; Teramoto, M.; Matsuyama, H.; Nakashima, K.; Hanaki, M.; Kubota, F.; Goto, M. CO2 Separation Facilitated by Task-specific Ionic Liquids Using a Supported Liquid Membrane. *J. Memb. Sci.* **2008**, *314*, 1–4.

[83] Halder, K.; Khan, M. M.; Grünauer, J.; Shishatskiy, S.; Abetz, C.; Filiz, V.; Abetz, V. Blend Membranes of Ionic Liquid and Polymers of Intrinsic Microporosity with Improved Gas Separation Characteristics. *J. Memb. Sci.* **2017**, *539*, 368–382.

[84] Dai, Z.; Noble, R. D.; Gin, D. L.; Zhang, X.; Deng, L. Combination of Ionic Liquids With Membrane Technology: A New Approach for CO2 Separation. *J. Memb. Sci.* **2016**, *497*, 1–20.

[85] Duan, Y. C.; Wu, Y. H.; Yu, S. K.; Li, D. M. Separation of CO2 with Supported Ionic Liquid Membrane. *Prog. Chem.* **2012**, *24*, 1405–1412.

[86] Shin, J. Y.; Yamada, S. A.; Fayer, M. D. Carbon Dioxide in a Supported Ionic Liquid Membrane: Structural and Rotational Dynamics Measured with 2D IR and Pump–Probe Experiments. *J. Am. Chem. Soc.* **2017**, 11222–11232.

[87] Shin, J. Y.; Yamada, S. A.; Fayer, M. D. Dynamics of a Room Temperature Ionic Liquid in Supported Ionic Liquid Membranes vs the Bulk Liquid: 2D IR and Polarized IR Pump–Probe Experiments. *J. Am. Chem. Soc.* **2017**, *139*, 311–323.

[88] Shin, J. Y.; Yamada, S. A.; Fayer, M. D. Influence of Water on Carbon Dioxide and Room Temperature Ionic Liquid Dynamics: Supported Ionic Liquid Membrane vs the Bulk Liquid. *J. Phys. Chem. B* **2018**, *122*, 2389–2395.

[89] Piletic, I. R.; Tan, H.-S.; Fayer, M. D. Dynamics of Nanoscopic Water: Vibrational Echo and Infrared Pump-Probe Studies of Reverse Micelles †. *J. Phys. Chem. B* **2005**, *109*, 21273–21284.

[90] Moilanen, D. E.; Levinger, N. E.; Spry, D. B.; Fayer, M. D. Confinement or the Nature of the Interface? Dynamics of Nanoscopic Water. *J. Am. Chem. Soc.* **2007**, *129*, 14311–14318.

[91] Tan, B.; Cooper, A. I. Functional Oligo(vinyl acetate) CO 2 -philes for Solubilization and Emulsification. *J. Am. Chem. Soc.* **2005**, *127*, 8938–8939.

[92] Cowan, M. G.; Gin, D. L.; Noble, R. D. Poly(ionic liquid)/Ionic Liquid Ion-Gels with High "Free" Ionic Liquid Content: Platform Membrane Materials for CO2/Light Gas Separations. *Acc. Chem. Res.* **2016**, *49*, 724–732.

[93] Nikolaeva, D.; Azcune, I.; Sheridan, E.; Sandru, M.; Genua, A.; Tanczyk, M.; Jaschik, M.; Warmuzinski, K.; Jansen, J. C.; Vankelecom, I. F. J. Poly(vinylbenzyl chloride)-based Poly(ionic liquids) as Membranes for CO2 Capture From Flue Gas. *J. Mater. Chem. A* **2017**, *5*, 19808–19818.

[94] Yuan, J.; Mecerreyes, D.; Antonietti, M. Poly(ionic liquid)s: An Update. *Prog. Polym. Sci.* **2013**, *38*, 1009–1036.

[95] Smith, C. J. I.; Wagle, D. V.; O'Neill, H. M.; Evans, B. R.; Baker, S. N.; Baker, G. A.; O'Neill, H. M.; Evans, B. R.; Baker, S. N.; Baker, G. A. Bacterial Cellulose Ionogels as Chemosensory Supports. *ACS Appl. Mater. Interfaces* **2017**, *9*, 38042–38051.

[96] Lin, H.; Freeman, B. D.; Kalakkunnath, S.; Kalika, D. S. Effect of Copolymer Composition, Temperature, and Carbon Dioxide Fugacity on Pure- and Mixed-gas Permeability in Poly(ethylene glycol)-based Materials: Free Volume Interpretation. *J. Memb. Sci.* **2007**, *291*, 131–139.

[97] Kwak, K.; Park, S.; Finkelstein, I. J.; Fayer, M. D. Frequency-Frequency Correlation Functions and Apodization in Two-Dimensional Infrared Vibrational Echo Spectroscopy: a New Approach. *J. Chem. Phys.* **2007**, *127*, 124503.

[98] Fenn, E. E.; Fayer, M. D. Extracting 2D IR Frequency-Frequency Correlation Functions from Two Component Systems. *J. Chem. Phys.* **2011**, *135*, 074502.

[99] Hoffman, D. J.; Fayer, M. D. CLS Next Gen: Accurate Frequency–Frequency Correlation Functions from Center Line Slope Analysis of 2D Correlation Spectra Using Artificial Neural Networks. *J. Phys. Chem. A* **2020**, *124*, 5979–5992.

[100] Lazonder, K.; Pshenichnikov, M. S.; Wiersma, D. A. Easy Interpretation of Optical Two-Dimensional Correlation Spectra. *Opt. Lett.* **2006**, *31*, 3354–3356.

[101] Roberts, S. T.; Loparo, J. J.; Tokmakoff, A. Characterization of Spectral Diffusion from Two-Dimensional Line Shapes. *J. Chem. Phys.* **2006**, *125*, 84502.

[102] Feynman, R. P.; Leighton, R. B.; Sands, M. *The Feynman Lectures of Physics. Volume I: Mainly Mechanics, Radiation, and Heat*; Addison-Wesley Pub. Co.: Reading, Mass., 1963.

[103] Kramer, P. L.; Giammanco, C. H.; Fayer, M. D. Dynamics of Water, Methanol, and Ethanol in a Room Temperature Ionic Liquid. *J. Chem. Phys.* **2015**, *142*.

[104] Hamm, P.; Kaindl, R. A.; Stenger, J. Noise Suppression in Femtosecond Mid-Infrared Light Sources. *Opt. Lett.* **2000**, *25*, 1798–1800.

[105] Ren, Z. Ultrafast Structure and Dynamics of Ionic Liquids Revealed by Two-Dimensional Infrared Spectroscopy. Ph.D. thesis, University of Pittsburgh, 2018.

[106] Press, W. H.; Teukolsky, S. A.; Vetterlin, W. T.; Flannery, B. P. *Numerical Recipes in C*, 2nd ed.; Cambridge University Press: New York, 1992.

[107] Bhown, A. S.; Freeman, B. C. Analysis and Status of Post-Combustion Carbon Dioxide Capture Technologies. *Environ. Sci. Technol.* **2011**, *45*, 8624–8632.

[108] Kerlé, D.; Ludwig, R.; Geiger, A.; Paschek, D. Temperature Dependence of the Solubility of Carbon Dioxide in Imidazolium-Based Ionic Liquids. *J. Phys. Chem. B* **2009**, *113*, 12727–12735.

[109] Carvalho, P. J.; Alvarez, V. H.; Schröder, B.; Gil, A. M.; Marrucho, I. M.; Aznar, M.; Santos, L. M. N. B. F.; Coutinho, J. A. P. Specific Solvation Interactions of CO2 on Acetate and Trifluoroacetate Imidazolium Based Ionic Liquids at High Pressures. *J. Phys. Chem. B* **2009**, *113*, 6803–6812.

[110] Rufford, T. E.; Smart, S.; Watson, G. C. Y.; Graham, B. F.; Boxall, J.; da Costa, J. C. D.; May, E. F. The Removal of CO2 and N2 From Natural Gas: A Review of Conventional and Emerging Process Technologies. *J. Pet. Sci. Eng.* **2012**, *94-95*, 123–154.

[111] Ansaloni, L.; Nykaza, J. R.; Ye, Y.; Elabd, Y. A.; Giacinti Baschetti, M. Influence of Water Vapor on the Gas Permeability of Polymerized Ionic Liquids Membranes. *J. Memb. Sci.* **2015**, *487*, 199–208.

[112] Scovazzo, P.; Kieft, J.; Finan, D. A.; Koval, C.; DuBois, D.; Noble, R. Gas Separations Using Non-Hexafluorophosphate [PF6]- Anion Supported Ionic Liquid Membranes. *J. Memb. Sci.* **2004**, *238*, 57–63.

[113] Liang, J.; Xu, K.; Arora, S.; Laaser, J. E.; Fullerton-Shirey, S. K. Ion-Locking in Solid Polymer Electrolytes for Reconfigurable Gateless Lateral Graphene p-n Junctions. *Materials (Basel).* **2020**, *13*.

[114] Arora, S.; Liang, J.; Fullerton-Shirey, S. K.; Laaser, J. E. Triggerable Ion Release in Polymerized Ionic Liquids Containing Thermally Labile Diels-Alder Linkages. *ACS Mater. Lett.* **2020**, 331–335.

[115] Triolo, A.; Russina, O.; Bleif, H.-J.; Di Cola, E. Nanoscale Segregation in Room Temperature Ionic Liquids. *J. Phys. Chem. B* **2007**, *111*, 4641–4644.

[116] Hardacre, C.; Holbrey, J. D.; Mullan, C. L.; Youngs, T. G. A.; Bowron, D. T. Small Angle Neutron Scattering from 1-alkyl-3-methylimidazolium Hexafluorophosphate Ionic Liquids ([$C_n$mim][PF_6], n=4, 6, and 8). *J. Chem. Phys.* **2010**, *133*, 74510.

[117] Russina, O.; Triolo, A.; Gontriani, L.; Caminiti, R. Mesoscopic Structural Heterogeneities in Room-Temperature Ionic Liquids. *J. Phys. Chem. B* **2011**, *3*, 27–33.

[118] Urahata, S. M.; Ribeiro, M. C. C. Structure of Ionic Liquids of 1-alkyl-3-methylimidazolium cations: A Systematic Computer Simulation Study. *J. Chem. Phys.* **2004**, *120*, 1855–1863.

[119] Wang, Y.; Voth, G. A. Unique Spatial Heterogeneity in Ionic Liquids. *J. Am. Chem. Soc.* **2005**, *127*, 12192–12193.

[120] Canongia Lopes, J. N. A.; Pádua, A. A. H. Nanostructural Organization in Ionic Liquids. *J. Phys. Chem. B* **2006**, *110*, 3330–3335.

[121] Araque, J. C.; Hettige, J. J.; Margulis, C. J. Modern Room Temperature Ionic Liquids, a Simple Guide to Understanding Their Structure and How It May Relate to Dynamics. *J. Phys. Chem. B* **2015**, *119*, 12727–12740.

[122] Shimizu, K.; Bernardes, C. E. S.; Canongia Lopes, J. N. Structure and Aggregation in the 1-Alkyl-3-Methylimidazolium Bis(trifluoromethylsulfonyl)imide Ionic Liquid Homologous Series. *J. Phys. Chem. B* **2014**, *118*, 567–576.

[123] Castner, E. W., Jr.; Wishart, J. F. Spotlight on Ionic Liquids. *J. Chem. Phys.* **2010**, *132*, 120901.

[124] Castner, E. W., Jr.; Wishart, J. F.; Shirota, H. Intermolecular Dynamics, Interactions, and Solvation in Ionic Liquids. *Acc. Chem. Res.* **2007**, *40*, 1217–1227.

[125] Jin, H.; Li, X.; Maroncelli, M. Heterogeneous Solute Dynamics in Room Temperature Ionic Liquids. *J. Phys. Chem. B* **2007**, *111*, 13473–13478.

[126] Dutta, S.; Ren, Z.; Brinzer, T.; Garrett-Roe, S. Two-Dimensional Ultrafast Vibrational Spectroscopy of Azides in Ionic Liquids Reveals Solute-specific Solvation. *Phys. Chem. Chem. Phys.* **2015**, *17*, 26575–26579.

[127] Fruchey, K.; Lawler, C. M.; Fayer, M. D. Investigation of Nanostructure in Room Temperature Ionic Liquids using Electronic Excitation Transfer. *J. Phys. Chem. B* **2012**, *116*, 3054–3064.

[128] Fruchey, K.; Fayer, M. D. Dynamics in Organic Ionic Liquids in Distinct Regions Using Charged and Uncharged Orientational Relaxation Probes. *J. Phys. Chem. B* **2010**, *114*, 2840–2845.

[129] Xiao, D.; Rajian, J. R.; Hines, L. G., Jr.; Li, S.; Bartsch, R. A.; Quitevis, E. L. Nanostructural Organization and Anion Effects in the Optical Kerr Effect Spectra of Binary Ionic Liquid Mixtures. *J. Phys. Chem. B* **2008**, *112*, 13316–13325.

[130] Daguenet, C.; Dyson, P. J.; Krossing, I.; Oleinikova, A.; Slattery, J.; Wakai, C.; Weingärtner, H. Dielectric Response of Imidazolium-Based Room-Temperature Ionic Liquids. *J. Phys. Chem. B* **2006**, *110*, 12682–12688.

[131] Yamada, S. A.; Bailey, H. E.; Tamimi, A.; Li, C.; Fayer, M. D. Dynamics in a Room-Temperature Ionic Liquid from the Cation Perspective: 2D IR Vibrational Echo Spectroscopy. *J. Am. Chem. Soc.* **2017**, *139*, 2408–2420.

[132] Sonnleitner, T.; Turton, D. A.; Waselikowski, S.; Hunger, J.; Stoppa, A.; Walther, M.; Wynne, K.; Buchner, R. Dynamics of RTILs : A Comparative Dielectric and OKE study. *J. Mol. Liq.* **2014**, *192*, 19–25.

[133] Turton, D. A.; Hunger, J.; Stoppa, A.; Hefter, G.; Thoman, A.; Walther, M.; Buchner, R.; Wynne, K. Dynamics of Imidazolium Ionic Liquids from a Combined Dielectric Relaxation and Optical Kerr Effect Study: Evidence for Mesoscopic Aggregation. *J. Am. Chem. Soc.* **2009**, *131*, 11140–11146.

[134] Ramasesha, K.; Roberts, S. T.; Nicodemus, R. A.; Mandal, A.; Tokmakoff, A. Ultrafast 2D IR Anisotropy of Water Reveals Reorientation During Hydrogen-Bond Switching. *J. Chem. Phys.* **2011**, *135*, 54509.

[135] Kramer, P. L.; Nishida, J.; Giammanco, C. H.; Tamimi, A.; Fayer, M. D. Observation and Theory of Reorientation-Induced Spectral Diffusion in Polarization-Selective 2D IR Spectroscopy. *J. Chem. Phys.* **2015**, *142*, 184505.

[136] Anaredy, R. S.; Shaw, S. K. Long-Range Ordering of Ionic Liquid Fluid Films. *Langmuir* **2016**, *32*, 5147–5154.

[137] Tracy, K. M.; Guchhait, B.; Tibbetts, C.; Luther, B. M.; Krummel, A. Visualizing Chemical Dynamics in an Ionic Liquid Microdroplet using Ultrafast 2D IR Microscopy. *ChemRxiv* **2019**, 10.26434/CHEMRXIV.9936464.V1.

[138] Thomaz, J. E.; Bailey, H. E.; Fayer, M. D. The Influence of Mesoscopic Confinement on the Dynamics of Imidazolium-Based Room Temperature Ionic Liquids in Polyether Sulfone Membranes. *J. Chem. Phys.* **2017**, *147*.

[139] Oxtoby, D. W. *Adv. Chem. Phys.*; 2007; Vol. 47; pp 487–519.

[140] Oxtoby, D. W. Vibrational Relaxation in Liquids. *Annu. Rev. Phys. Chem.* **1981**, *32*, 77–101.

[141] Hamm, P.; Lim, M.; Hochstrasser, R. M. Vibrational Relaxation and Dephasing of Small Molecules Strongly Interacting with Water. Ultrafast Phenom. XI. BERLIN, 1998; pp 514–516.

[142] Giammanco, C. H.; Kramer, P. L.; Yamada, S. A.; Nishida, J.; Tamimi, A.; Fayer, M. D. Coupling of Carbon Dioxide Stretch and Bend Vibrations Reveals Thermal Population Dynamics in an Ionic Liquid. *J. Phys. Chem. B* **2016**, *120*, 549–556.

[143] Cunliffe-Jones, D. B. Perturbation of Some Vibrational Bands in Solution. *Spectrochim. Acta Part A* **1969**, *25*, 779.

[144] Hamm, P.; Stock, G. Vibrational Conical Intersections as a Mechanism of Ultrafast Vibrational Relaxation. *Phys. Rev. Lett.* **2012**, *109*, 173201.

[145] Stock, G. Classical Simulation of Quantum Energy Flow in Biomolecules. *Phys. Rev. Lett.* **2009**, *102*, 118301.

[146] Ka, B. J.; Geva, E. Vibrational Energy Relaxation of Polyatomic Molecules in Liquid Solution via the Linearized Semiclassical Method. *J. Phys. Chem. A* **2006**, *110*, 9555–9567.

[147] Alemi, M.; Loring, R. F. Vibrational Coherence and Energy Transfer in Two-Dimensional Spectra ith the Optimized Mean-Trajectory Approximation. *J. Chem. Phys.* **2015**, *142*, 212417.

[148] Ramesh, P.; Loring, R. F. Thermal Population Fluctuations in Two-Dimensional Infrared Spectroscopy Captured with Semiclassical Mechanics. *J. Phys. Chem. B* **2018**, *122*, 3647–3654.

[149] Kilic, S.; Michalik, S.; Wang, Y.; Johnson, J. K.; Enick, R. M.; Beckman, E. J. Phase Behavior of Oxygen-Containing Polymers in CO2. *Macromolecules* **2007**, *40*, 1332–1341.

[150] Helbing, J.; Hamm, P. Compact Implementation of Fourier Transform Two-Dimensional IR Spectroscopy Without Phase Ambiguity. *J. Opt. Soc. Am. B* **2011**, *28*, 171.

[151] Kalakkunnath, S.; Kalika, D. S.; Lin, H.; Raharjo, R. D.; Freeman, B. D. Molecular Relaxation in Cross-linked Poly(ethylene glycol) and Poly(propylene glycol) Diacrylate Networks by Dielectric Spectroscopy. *Polymer (Guildf).* **2007**, *48*, 579–589.

[152] Singh, T.; Kumar, A. Static Dielectric Constant of Room Temperature Ionic Liquids: Internal Pressure and Cohesive Energy Density Approach. *J. Phys. Chem. B* **2008**, *112*, 12968–12972.

[153] Pakoulev, A.; Wang, Z. H.; Pang, Y. S.; Dlott, D. D. Vibrational Energy Relaxation Pathways of Water. *Chem. Phys. Lett.* **2003**, *380*, 404–410.

[154] Stenger, J.; Madsen, D.; Hamm, P.; Nibbering, E. T. J.; Elsaesser, T. A Photon Echo Peak Shift Study of Liquid Water. *J. Phys. Chem. A* **2002**, *106*, 2341–2350.

[155] Madsen, D.; Stenger, J.; Dreyer, J.; Hamm, P.; Nibbering, E. T. J.; Elsaesser, T. Femtosecond Mid-Infrared Pump–Probe Study of Wave Packet Motion in a Medium-Strong Intramolecular Hydrogen Bond. *Bull. Chem. Soc. Jpn.* **2002**, *75*, 909–917.

[156] Asbury, J. B.; Steinel, T.; Stromberg, C.; Gaffney, K. J.; Piletic, I. R.; Fayer, M. D. Hydrogen Bond Breaking Probed with Multidimensional Stimulated Vibrational Echo Correlation Spectroscopy. *J. Chem. Phys.* **2003**, *119*, 12981–12997.

[157] Steinel, T.; Asbury, J. B.; Zheng, J.; Fayer, M. D. Watching Hydrogen Bonds Break: A Transient Absorption Study of Water. *J. Phys. Chem. A* **2004**, *108*, 10957–10964.

[158] Liu, L.; Hunger, J.; Bakker, H. J. Energy Relaxation Dynamics of the Hydration Complex of Hydroxide. *J. Phys. Chem. A* **2011**, *115*, 14593–14598.

[159] Liu, L.; Bakker, H. J. Vibrational Excitation Induced Proton Transfer in Hydrated Nafion Membranes. *J. Phys. Chem. B* **2015**, *119*, 2628–2637.

[160] Abascal, J. L. F.; Vega, C. Widom Line and the Liquid-Liquid Critical Point for the TIP4P/2005 Water Model. *J. Chem. Phys.* **2010**, *133*, 234502.

[161] Ashihara, S.; Huse, N.; Espagne, A.; Nibbering, E. T. J.; Elsaesser, T. Ultrafast Structural Dynamics of Water Induced by Dissipation of Vibrational Energy. *J. Phys. Chem. A* **2007**, *111*, 743–746.

[162] Huse, N.; Ashihara, S.; Nibbering, E. T. J.; Elsaesser, T. Ultrafast Vibrational Relaxation of O-H Bending and Librational Excitations in Liquid H2O. *Chem. Phys. Lett.* **2005**, *404*, 389–393.

[163] Fecko, C. J.; Loparo, J. J.; Roberts, S. T.; Tokmakoff, A. Local Hydrogen Bonding Dynamics and Collective Reorganization in Water: Ultrafast Infrared Spectroscopy of HOD/D2O. *J. Chem. Phys.* **2005**, *122*, 54506.

[164] Roberts, S. T.; Ramasesha, K.; Petersen, P. B.; Mandal, A.; Tokmakoff, A. Proton Transfer in Concentrated Aqueous Hydroxide Visualized Using Ultrafast Infrared Spectroscopy. *J. Phys. Chem. A* **2011**, *115*, 3957–3972.

[165] Cringus, D.; Lindner, J.; Milder, M. T.; Pshenichnikov, M. S.; Vöhringer, P.; Wiersma, D. A. Femtosecond Water Dynamics in Reverse-Micellar Nanodroplets. *Chem. Phys. Lett.* **2005**, *408*, 162–168.

[166] Shinokita, K.; Cunha, A. V.; Jansen, T. L.; Pshenichnikov, M. S. Hydrogen Bond Dynamics in Bulk Alcohols. *J. Chem. Phys.* **2015**,

[167] Hunger, J.; Sonnleitner, T.; Liu, L.; Buchner, R.; Bonn, M.; Bakker, H. J. Hydrogen-Bond Dynamics in a Protic Ionic Liquid: Evidence of Large-Angle Jumps. *J. Phys. Chem. Lett.* **2012**, *3*, 3034–3038.

[168] Backus, E. H. G.; Nguyen, P. H.; Botan, V.; Pfister, R.; Moretto, A.; Crisma, M.; Toniolo, C.; Stock, G.; Hamm, P. Energy Transport in Peptide Helices: A Comparison between High- and Low-Energy Excitations. *J. Phys. Chem. B* **2008**, *112*, 9091–9099.

[169] Kurochkin, D. V.; Naraharisetty, S. R. G.; Rubtsov, I. V. A Relaxation-Assisted 2D IR Spectroscopy Method. *Proc. Natl. Acad. Sci.* **2007**, *104*, 14209–14214.

[170] Mackin, R. T.; Leong, T. X.; Rubtsova, N. I.; Burin, A. L.; Rubtsov, I. V. Low-Temperature Vibrational Energy Transport via PEG Chains. *J. Phys. Chem. Lett.* **2020**, 4578–4583.

[171] Botan, V.; Hamm, P. Intramolecular Vibrational Energy Relaxation in Nitrous Acid (HONO). *J. Chem. Phys.* **2008**, *129*, 164506.

[172] Kazarian, S. G.; Vincent, M. F.; Bright, F. V.; Liotta, C. L.; Eckert, C. A. Specific Intermolecular Interaction of Carbon Dioxide with Polymers. *J. Am. Chem. Soc.* **1996**, *118*, 1729–1736.

[173] Brinzer, T.; Berquist, E. J.; Dutta, S.; Johnson, C. A.; Krisher, C. S.; Lambrecht, D. S.; Garrett-Roe, S.; Ren, Z. Erratum: "Ultrafast Vibrational Spectroscopy (2D-IR) of CO2 in Ionic Liquids: Carbon Capture from Carbon Dioxide's Point of View" [J. Chem. Phys. 142, 212425 (2015)]. *J. Chem. Phys.* **2017**, *147*, 049901.

[174] Hamm, P.; Lim, M.; Hochstrasser, R. M. Vibrational Energy Relaxation of the Cyanide Ion in Water. *J. Chem. Phys.* **1997**, *107*, 10523–10531.

[175] Czurlok, D.; Gleim, J.; Lindner, J.; Vöhringer, P. Vibrational Energy Relaxation of Thiocyanate Ions in Liquid-to-Supercritical Light and Heavy Water. A Fermi's Golden Rule Analysis. *J. Phys. Chem. Lett.* **2014**, *5*, 3373–3379.

[176] Kraack, J. P.; Hamm, P. Surface-Sensitive and Surface-Specific Ultrafast Two-Dimensional Vibrational Spectroscopy. *Chem. Rev.* **2017**, *117*, 10623–10664.

[177] Tan, H.-S.; Piletic, I. R.; Fayer, M. D. Orientational Dynamics of Water Confined on a Nanometer Length Scale in Reverse Micelles. *J. Chem. Phys.* **2005**, *122*, 174501.

[178] Ren, Z.; Kelly, J.; Gunathilaka, C. P.; Brinzer, T.; Dutta, S.; Johnson, C. A.; Mitra, S.; Garrett-Roe, S. Ultrafast Dynamics of Ionic Liquids in Colloidal Dispersion. *Phys. Chem. Chem. Phys.* **2017**, *19*, 32526–32535.

[179] Fenn, E. E.; Wong, D. B.; Fayer, M. D. Water Dynamics in Small Reverse Micelles in Two Solvents: Two-Dimensional Infrared Vibrational Echoes with Two-Dimensional Background Subtraction. *J. Chem. Phys.* **2011**, *134*, 1–11.

[180] Piletic, I. R.; Moilanen, D. E.; Spry, D. B.; Levinger, N. E.; Fayer, M. D. Testing the Core/shell Model of Nanoconfined Water in Reverse Micelles using Linear and Nonlinear IR Spectroscopy. *J. Phys. Chem. A* **2006**, *110*, 4985–4999.

[181] Fenn, E. E.; Wong, D. B.; Giammanco, C. H.; Fayer, M. D. Dynamics of Water at the Interface in Reverse Micelles: Measurements of Spectral Diffusion with Two-Dimensional Infrared Vibrational Echoes. *J. Phys. Chem. B* **2011**, *115*, 11658–11670.

[182] Zhang, Z.; Piatkowski, L.; Bakker, H. J.; Bonn, M. Interfacial Water Structure Revealed by Ultrafast Two-Dimensional Surface Vibrational Spectroscopy. *J. Chem. Phys.* **2011**, *135*.

[183] Lin, H.; Freeman, B. D. Gas and Vapor Solubility in Cross-Linked Poly(ethylene Glycol Diacrylate). *Macromolecules* **2005**, *38*, 8394–8407.

[184] Nguyen, T. B. H.; Zondervan, E. Ionic Liquid as a Selective Capture Method of CO2 from Different Sources: Comparison with MEA. *ACS Sustain. Chem. Eng.* **2018**, *6*, 4845–4853.

[185] Kim, S. Nano- and Micro-Engineered Membrane Technology. 2018.

[186] Ren, Z.; Garrett-Roe, S. Reorientation-Induced Spectral Diffusion of Non-Isotropic Orientation Distributions. *J. Chem. Phys.* **2017**, *147*, 144504.

[187] Kelsheimer, C. J.; Garrett-Roe, S. Intramolecular Vibrational Energy Relaxation of CO 2 in Cross-Linked Poly(ethylene glycol) Diacrylate-Based Ion Gels. *J. Phys. Chem. B* **2021**, *125*, 1402–1415.

[188] Dokter, A. M.; Woutersen, S.; Bakker, H. J. Inhomogeneous Dynamics in Confined Water Nanodroplets. *Proc. Natl. Acad. Sci.* **2006**, *103*, 15355–15358.

[189] Dokter, A. M.; Woutersen, S.; Bakker, H. J. Anomalous Slowing Down of the Vibrational Relaxation of Liquid Water upon Nanoscale Confinement. *Phys. Rev. Lett.* **2005**, *94*, 178301.

[190] Tokmakoff, A. Orientational Correlation Functions and Polarization Selectivity for Nonlinear Spectroscopy of Isotropic Media .1. Third Order. *J. Chem. Phys.* **1996**, *105*, 1–12.

[191] Hochstrasser, R. M. Two-Dimensional IR-spectroscopy: Polarization Anisotropy Effects. *Chem. Phys.* **2001**, *266*, 273–284.

[192] Eaves, J. D.; Fecko, C. J.; Stevens, A. L.; Peng, P.; Tokmakoff, A. Polarization-selective Femtosecond Raman Spectroscopy of Low-frequency Motions in Hydrated Protein Films. *Chem. Phys. Lett.* **2003**, *376*, 20–25.

[193] Lin, Y.-S.; Pieniazek, P. A.; Yang, M.; Skinner, J. L. On the Calculation of Rotational Anisotropy Decay, as Measured by Ultrafast Polarization-Resolved Vibrational Pump-Probe Experiments. *J. Chem. Phys.* **2010**, *132*, 174505.

[194] Rivera, C. A.; Souna, A. J.; Bender, J. S.; Manfred, K.; Fourkas, J. T. Reorientation-Induced Spectral Diffusion in Vibrational Sum-Frequency-Generation Spectroscopy. *J. Phys. Chem. B* **2013**, *117*, 15875–15885.

[195] Johnson, C. A.; Parker, A. W.; Donaldson, P. M.; Garrett-Roe, S. An Ultrafast Vibrational Study of Dynamical Heterogeneity in the Protic Ionic Liquid Ethyl-ammonium Nitrate: I. Room Temperature Dynamics. *J. Chem. Phys.* **2021**, *accepted*.

[196] Bredenbeck, J.; Hamm, P. Versatile Small Volume Closed-cycle Flow Cell System for Transient Spectroscopy at High Repetition Rates. *Rev. Sci. Instrum.* **2003**, *74*, 3188–3189.

[197] Lipari, G.; Szabo, A. Effect of Librational Motion on Fluorescence Depolarization and Nuclear Magnetic Resonance Relaxation in Macromolecules and Membranes. *Biophys. J.* **1980**, *30*, 489–506.

[198] Hamm, P. Principles of Nonlinear Optical Spectroscopy : A Practical Approach or : Mukamel for Dummies. *Univ. Zurich* **2005**, *41*, 77.

[199] Fica-Contreras, S. M.; Hoffman, D. J.; Pan, J.; Liang, C.; Fayer, M. D. Free Volume Element Sizes and Dynamics in Polystyrene and Poly(methyl methacrylate) Measured with Ultrafast Infrared Spectroscopy. *J. Am. Chem. Soc.* **2021**, jacs.0c13397.

[200] Kelsheimer, C. J.; Garrett-Roe, S. Environment Distribution in Ion Gels: A Core-Shell-Matrix Hypothesis. *Prep.* **2021**,

[201] Nandi, A. K.; Mandal, B. M.; Bhattacharyya, S. N. Miscibility of Poly(methyl acrylate) and Poly(vinyl acetate): Incompatibility in Solution and Thermodynamic Characterization by Inverse Gas Chromatography. *Macromolecules* **1985**, *18*, 1454–1460.

[202] Tapriyal, D.; Wang, Y.; Enick, R.; Johnson, J.; Crosthwaite, J.; Thies, M.; Paik, I.; Hamilton, A. Poly(vinyl acetate), Poly((1-O-(vinyloxy) ethyl-2,3,4,6-tetra-O-acetyl-β-d-glucopyranoside) and Amorphous Poly(lactic acid) are the Most CO2-soluble Oxygenated Hydrocarbon-based Polymers. *J. Supercrit. Fluids* **2008**, *46*, 252–257.

[203] Zhang, C.; Zhang, W.; Gao, H.; Bai, Y.; Sun, Y.; Chen, Y. Synthesis and Gas Transport Properties of Poly(ionic liquid)-based Semi-interpenetrating Polymer Network Membranes for CO2/N2 Separation. *J. Memb. Sci.* **2017**, *528*, 72–81.

[204] Shen, Y. C.; Upadhya, P. C.; Linfield, E. H.; Davies, A. G. Temperature-dependent Low-frequency Vibrational Spectra of Purine and Adenine. *Appl. Phys. Lett.* **2003**, *82*, 2350–2352.

[205] Shen, Z.; McHugh, M.; Xu, J.; Belardi, J.; Kilic, S.; Mesiano, A.; Bane, S.; Karnikas, C.; Beckman, E.; Enick, R. CO2-solubility of Oligomers and Polymers that Contain the Carbonyl Group. *Polymer (Guildf).* **2003**, *44*, 1491–1498.

[206] Vakili, E.; Semsarzadeh, M. A.; Ghalei, B.; Khoshbin, M.; Nasiri, H. Characterization and Gas Permeation Properties of Synthesized Polyurethane-Polydimethylsiloxane / Polyamide 12-b-Polytetramethylene Glycol Blend Membranes. *Silicon* **2016**, *8*, 75–85.

[207] Brinzer, T. Ultrafast Dynamics of Carbon Dioxide in Imidazolium Ionic Liquids. Ph.D. thesis, University of Pittsburgh, 2018.

[208] Giammanco, C. H.; Kramer, P. L.; Wong, D. B.; Fayer, M. D. Water Dynamics in 1-Alkyl-3-methylimidazolium Tetrafluoroborate Ionic Liquids. *J. Phys. Chem. B* **2016**, *120*, 11523–11538.

[209] Giammanco, C. H.; Kramer, P. L.; Fayer, M. D. Dynamics of Dihydrogen Bonding in Aqueous Solutions of Sodium Borohydride. *J. Phys. Chem. B* **2015**, *119*, 3546–3559.

[210] Sanchis, A.; Prolongo, M. G.; Masegosa, R. M.; Rubio, R. G. Dynamic-Mechanical Study of the Dynamics of Polymer Blends near the Glass Transition. *Macromolecules* **1995**, *28*, 2693–2699.

[211] Kilic, S.; Michalik, S.; Wang, Y.; Johnson, J. K.; Enick, R. M.; Beckman, E. J. Effect of Grafted Lewis Base Groups on the Phase Behavior of Model Poly(dimethyl siloxanes) in CO 2. *Ind. Eng. Chem. Res.* **2003**, *42*, 6415–6424.

[212] Moreno, J. S.; Jeremias, S.; Moretti, A.; Panero, S.; Passerini, S.; Scrosati, B.; Appetecchi, G. B. Ionic Liquid Mixtures with Tunable Physicochemical Properties. *Electrochim. Acta* **2015**, *151*, 599–608.

[213] Canongia Lopes, J. N.; Cordeiro, T. C.; Esperança, J. M. S. S.; Guedes, H. J. R.; Huq, S.; Rebelo, L. P. N.; Seddon, K. R. Deviations from Ideality in Mixtures of Two Ionic Liquids Containing a Common Ion. *J. Phys. Chem. B* **2005**, *109*, 3519–3525.

[214] Fillion, J. J.; Brennecke, J. F. Viscosity of Ionic Liquid–Ionic Liquid Mixtures. *J. Chem. Eng. Data* **2017**, *62*, 1884–1901.

[215] Chatel, G.; Pereira, J. F. B.; Debbeti, V.; Wang, H.; Rogers, R. D. Mixing Ionic Liquids – "Simple Mixtures" or "Double Salts"? *Green Chem.* **2014**, 2051–2083.

[216] Niedermeyer, H.; Hallett, J. P.; Villar-Garcia, I. J.; Hunt, P. A.; Welton, T. Mixtures of Ionic Liquids. *Chem. Soc. Rev.* **2012**, *41*, 7780.

[217] Flory, P. J. Thermodynamics of High Polymer Solutions. *J. Chem. Phys.* **1942**, *10*, 51–61.

[218] Huggins, M. L. Theory of Solutions of High Polymers. *J. Am. Chem. Soc.* **1942**, *64*, 1712–1719.

[219] Rodríguez, H.; Rogers, R. D. Liquid Mixtures of Ionic Liquids and Polymers as Solvent Systems. *Fluid Phase Equilib.* **2010**, *294*, 7–14.

[220] Higgins, J. S.; Lipson, J. E. G.; White, R. P. A Simple Approach to Polymer Mixture Miscibility. *Philos. Trans. R. Soc. A Math. Phys. Eng. Sci.* **2010**, *368*, 1009–1025.

[221] Barlow, J. W.; Paul, D. R. Polymer Blends and Alloys? A Review of Selected Considerations. *Polym. Eng. Sci.* **1981**, *21*, 985–996.

[222] Araque, J. C.; Hettige, J. J.; Margulis, C. J. Ionic Liquids—Conventional Solvent Mixtures, Structurally Different but Dynamically Similar. *J. Chem. Phys.* **2015**, *143*, 134505.

[223] Machefer, S.; Schnitzlein, K. Ideal Mixing Rules for the Viscosity of Complex Polymer-Solvent Mixtures: Assessment of Segment-Fraction Approximations. *Ind. Eng. Chem. Res.* **2006**, *45*, 7293–7300.

[224] Schutt, T. C.; Hegde, G. A.; Bharadwaj, V. S.; Johns, A. J.; Maupin, C. M. Impact of Water-Dilution on the Solvation Properties of the Ionic Liquid 1-Methyltriethoxy-3-ethylimidazolium Acetate for Model Biomass Molecules. *J. Phys. Chem. B* **2017**, *121*, 843–853.

[225] Hegde, G. A.; Bharadwaj, V. S.; Kinsinger, C. L.; Schutt, T. C.; Pisierra, N. R.; Maupin, C. M. Impact of Water Dilution and Cation Tail Length on Ionic Liquid Characteristics: Interplay Between Polar and Non-polar Interactions. *J. Chem. Phys.* **2016**, *145*, 064504.

[226] Kaneko, K.; Saihara, K.; Masuda, Y.; Yoshimura, Y.; Shimizu, A. Dynamic Properties of Water Molecules in Ionic Liquid/Water Mixture with Various Alkyl Chain Length. *J. Mol. Liq.* **2018**, *264*, 337–342.

[227] Fajardo, O. Y.; Bresme, F.; Kornyshev, A. A.; Urbakh, M. Water in Ionic Liquid Lubricants: Friend and Foe. *ACS Nano* **2017**, *11*, 6825–6831.

[228] Sippel, P.; Dietrich, V.; Reuter, D.; Aumüller, M.; Lunkenheimer, P.; Loidl, A.; Krohns, S. Impact of Water on the Charge Transport of a Glass-forming Ionic Liquid. *J. Mol. Liq.* **2016**, *223*, 635–642.

[229] Low, B. T.; Zhao, L.; Merkel, T. C.; Weber, M.; Stolten, D. A Parametric Study of the Impact of Membrane Materials and Process Operating Conditions on Carbon Capture from Humidified Flue Gas. *J. Memb. Sci.* **2013**, *431*, 139–155.

[230] Noferini, D.; Faraone, A.; Rossi, M.; Mamontov, E.; Fratini, E.; Baglioni, P. Disentangling Polymer Network and Hydration Water Dynamics in Polyhydroxyethyl Methacrylate Physical and Chemical Hydrogels. *J. Phys. Chem. C* **2019**, *123*, 19183–19194.

[231] Pissis, P.; Kyritsis, A. Hydration Studies in Polymer Hydrogels. *J. Polym. Sci. Part B Polym. Phys.* **2013**, *51*, 159–175.